Charles University
Faculty of Mathematics and Physics

Doctoral Thesis

Spin and Lattice Excitations in Multiferroics

Stella Skiadopoulou

Department of Dielectrics
Institute of Physics
Czech Academy of Sciences

Supervisor: RNDr. Stanislav Kamba, CSc.

Study Programme: 4F3
Physics of Condensed Matter and Materials Research

Prague 2017

Acknowledgements

A doctoral thesis is not just about fascinating scientific novelties. This period of a doctoral student's life corresponds to a phase transition. One might debate on whether it is of first- or second-order, but this requires the inclusion of extra parameters, depending on the system (a.k.a. student) in question. In most cases, the system is multifunctional; therefore there exist more than one order parameters. To name a few: experience on scientific research, knowledge in new fields, new capabilities, writing, oral presentation and communication skills, and … multifunctionality itself. As one can see, it would be impossible to make the crossover from one phase to the other without any external help.

Before anything else, I am highly indebted to my supervisor Stanislav Kamba for the continuous support, guidance, patience, immense knowledge (not only scientific), and constant inspiration. His optimism, sense of humour and understanding supported me at stressful and difficult moments. Moreover, he did not only teach me physics, but how to lead a full life.

My thanks and appreciation also go to Veronica Goian who guided me through my first steps in infrared spectroscopy, but also through the beginning of my stay in Prague.

A very special gratitude goes to Fedir Borodavka for his precious guidance during the Raman spectroscopy experiments. I learned a lot from his patient and persistent attitude of conducting experiments.

I would like to express my sincere thanks to Christelle Kadlec and Filip Kadlec for their valuable support during the terahertz spectroscopy experiments, as well as the stimulating discussions.

I would also like to thank Maxim Savinov for the dielectric measuremtns, Jan Prokleška for his help with the magnetic measurements, Jan Drahokoupil and Maruška Trousilová for the X-ray diffraction (XRD) measurements, and Karel Jurek for the energy dispersive spectroscopy (EDS) measurements.

In particular, I would like to thank Professor Martha Greenblatt and her group for the significant collaboration on the Pb_2MnTeO_6 and Ni-based Tellurides work. Especially, my thanks go to Maria Retuerto, Zheng Deng, and Xiaojan Tan, for the synthesis of the samples.

My sincere thanks go to Xiaofei Bai, Ingrid C. Infante, and Brahim Dkhil for the $BiFeO_3$ ceramics, and Carolina Adamo and Darrell Schlom for the $BiFeO_3$ thin film.

Exceptionally, my great appreciation and warm thanks go to my colleagues from the Department of Dielectrics, namely Martin Kempa, Elena Buixaderas, Kristína Šášiková, Marek Pasciak, Jan Pokorny, Jakub Vit, Vladimir Pushkarev, Jirka Hlinka, Jan Petzelt, Peter Kužel,

Viktor Bovtun, Dmitry Nuzhnyy, Peter Ondrejkovic, Pavel Márton, Ivan Gregora, Vilgelmina Stepkova, Iegor Rafalovskyi, not only for the insightful discussions and comments, but also because they really made me feel like being a part of a family.

Another important contribution to my scientific, as well as personal life during my doctoral years, was made by my participation to the Initial Training Network NOTEDEV (Novel Terahertz Devices), supported by European Union funding under the 7th Framework Programme.

The current thesis also received financial support by the Czech Science Foundation (Project 15-08389S) and MŠMT KONTAKT II project LH15122.

And last but not least, I would like to thank my parents, Nikos and Marina, my sister Dimitra, and my friends, Cemal, Anna, Aga, Elena, Tinka, Fotini, Vova, Martin and Marek, for the devoted support, encouragement and funtimes during these past four years.

Declaration and confession

I declare that I carried out this doctoral thesis independently, and only with the cited sources, literature and other professional sources.

I understand that my work relates to the rights and obligations under the Act No. 121/2000 Coll., the Copyright Act, as amended, in particular the fact that Charles University in Prague has the right to conclude a license agreement on the use of this work as a school work pursuant to Section 60 paragraph of the Copyright Act.

In Prague, on July, 2017 Stella Skiadopoulou

Abstrakt v českém jazyce

Název doktorské práce: *Spinové a mřižkové excitace v multiferoikách*

Autor: *Stella Skiadopoulou*

Ústav: Oddělaní dielektrik, Fyzikální ústav AV ČR v.v.i, Na Slovance 2, 182 21, Praha 8

Školitel: *RNDr. Stanislav Kamba, CSc.*

Školící pracoviště: Oddělaní dielektrik, Fyzikální ústav AV ČR v.v.i, Na Slovance 2, 182 21, Praha 8

Konzultanti: *Veronica Goian, Christelle Kadlec, Filip Kadlec*

Abstrakt

Vědecký význam dynamické magnetoelektrické vazby kombinovaný s jejími pozoruhodnými potenciálními technologickými aplikacemi podnítil naše studium spinových a mřížkových excitací v řadě dobře známých i kompletně nových multiferoických materiálech.

Byly studovány magnetoelektrické excitace ve slavném pokojovém multiferoiku $BiFeO_3$. Kromě jiných se nalezly dvě nové infračerveně aktivní spinové excitace. Polární fonony byly studovány v širokém teplotním oboru jak v $BiFeO_3$ keramikách, tak vůbec poprvé i v tenké epitaxní vrstvě narostlé na substrátu $TbScO_3$.

Poprvé byl připraven a popsán dvojitý perovskit Pb_2MnTeO_6, který byl zařazen do vzácné rodiny antipolárních antiferomagnetů.

Kolosální spinově-indukovaný magnetoelektrický jev v Ni_3TeO_6 nás stimuloval k objevu elektromagnonů v tomto materiálu i k přípravě a studiu nových materiálů, kde Ni je částečně nahrazen pomocí Mn a Co. Všechny $Ni_{3-x}B_xTeO_6$ (B=Mn, Co) vzorky vykazují necentrosymetrickou *R*3 prostorovou grupu, kolineární antiferomagnetickou strukturu a spinově-indukovanou elektrickou polarizaci pod T_N. Dopování pomocí Mn zvyšuje Néelovu teplotu, zatímco Co dopování snižuje kritické magnetické pole pro spin-flop přechod, při kterém se zvyšuje magnetoelektrická vazba. Spinové excitace byly objevené ve všech sloučeninách. Kromě magnonů, Ni_3TeO_6 a $NiCo_2TeO_6$ vykazují i elektromagnony.

Abstract in English

Title: *Spin and Lattice Excitations in Multiferroics*

Author: *Stella Skiadopoulou*

Institute: Department of Dielectrics, Institute of Physics of the Czech Academy of Sciences, Na Slovance 2, 182 21, Prague 8

Advisor of the doctoral work: *RDNr. Stanislav Kamba, CSc.*

Training Institute: Department of Dielectrics, Institute of Physics of the Czech Academy of Sciences, Na Slovance 2, 182 21, Prague 8

Consultants: *Veronica Goian, Christelle Kadlec, Filip Kadlec*

Abstract

The scientific significance of dynamical magnetoelectric coupling, combined with the eminent implication of its technological applications, prompted our investigation of spin and lattice excitations of a series of widely known, as well as entirely novel, multiferroic materials.

The magnetoelectric excitations of the celebrated room temperature multiferroic $BiFeO_3$ were investigated. Among the previously reported, two new infrared active spin excitations were discovered. Polar phonons in $BiFeO_3$ ceramics, as well as in a thin film epitaxially grown on $TbScO_3$ substrate, were investigated in a broad temperature range.

The novel double perovskite Pb_2MnTeO_6 was prepared and described for the first time. Its crystal and magnetic structure classify it in the rare family of antipolar antiferromagnets.

The spin-induced colossal magnetoelectric effect in Ni_3TeO_6 stimulated us to discover electromagnons in this material and to prepare and study Mn and Co doped samples. All $Ni_{3-x}B_xTeO_6$ (B=Mn, Co) compounds present the non-centrosymmetric *R*3 space group symmetry, collinear antiferromagnetic spin structure, and spin-induced electric polarization below T_N. Mn-doping results in increase of the Néel temperature, whereas Co-doping in decrease of the magnetic field value of the spin-flop transition, at which the magnetoelectric coupling enhances. Spin excitations were observed in all compounds. In addition to the pure magnons, Ni_3TeO_6 and $NiCo_2TeO_6$ also display electromagnons.

Contents

Preface

The relatively new field of multiferroic materials, with its revival in 2000s, is of great value for the advances of various distinct fields of condensed matter physics, which astonishingly entangle and interplay under the broad roof of the multiferroic family.

Throughout the history of multiferroics, the static magnetoelectric coupling holds the reins of the multiferroic scientific front. However, there is a great interest in what happens away from the static regime in multiferroic systems; hence the exploration of the dynamical magnetoelectric effect was considerably triggered in recent years. Both cases share the same microscopic mechanisms, but in the latter case the order parameters of magnetization and polarization are not static, but oscillatory. Very often, in this dynamical regime, novel elementary excitations called *electromagnons* emerge, as "carriers" of this dynamical magnetoelectric coupling.

In that fashion, already widely known multiferroic materials, as well as entirely novel compounds, were studied and will be presented in the current thesis, in the frame of spin and lattice excitations, investigated by the combination of infrared, time-domain terahertz and Raman spectroscopies.

The layout of the current thesis consists of four chapters:

- Chapter 1: Introduction to the physical concepts of multiferroics, ferroelectrics and the dynamical magnetoelectric coupling
- Chapter 2: Description of the experimental methods used for the current study
- Chpater 3: Experimental results of three groups of multiferroic materials: $BiFeO_3$, Pb_2MnTeO_6, and the corundum-related family of $Ni_{3-x}B_xTeO_6$ (B=Mn, Co)
- Chapter 4: Conclusions

Chapter 1

Introduction

1 Introduction

The main physical concepts discussed in the current thesis will be presented in Chapter 1. A brief historical evolution of the scientific fields in question, in combination with the current trends, will be portrayed, supported by selected bibliographic review.

The first part of the chapter is devoted to the broad family of multiferroic materials. An attempt to describe the quantum-level microscopic mechanisms responsible for the magnetoelectric multiferroic behavior is of great importance. Subsequently, the classification of diverse multiferroic cases of materials will be stated. The celebrated dynamical magnetoelectric effect, which is the main interest of the current work, engages substantial part of this section.

In 1.2, the principles of ferroelectrics are presented, offering a glance at the polar counterpart of magnetoelectric multiferroicity, whether intrinsic or magnetically-induced.

Finally, a brief theoretical background of spin and lattice excitations in solids will be laid in section 1.3, in order to prepare the ground for the upcoming experimental observations.

The image below corresponds to a schematic representation of a snapshot of the spin precession in an antiferromagnetically ordered magnetic system. Such spin dynamics are responsible for the formation of magnons, which if coupled to the lattice dynamics, correspond to electromagnons (image created by the author).

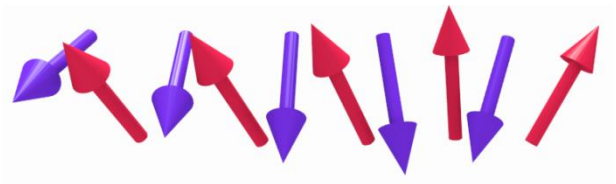

1.1 **Multiferroics**

The relatively new field of multiferroic materials, with its revival in 2000s, is of great value for the advances of various distinct fields of condensed matter physics, which astonishingly entangle and interplay under the broad roof of the multiferroic family.[1–6]

In the current section, a brief history of multiferroics will be presented, followed by some basic physics concepts, classification and proposed multiferroicity mechanisms to date.

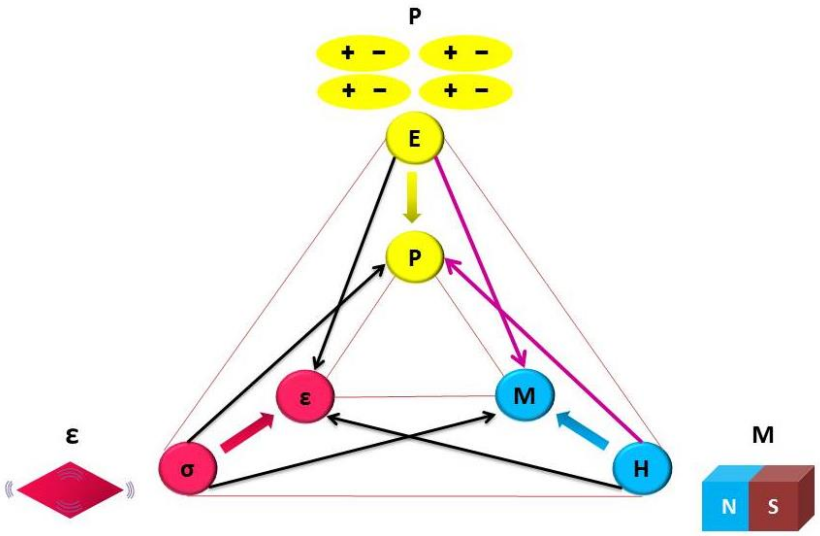

Figure 1.1 Schematic illustration of the possible interactions between the primary ferroic properties in multiferroic materials. The interplay between ferroelectricity and magnetism is highlighted with purple arrows for the particular case of magnetoelectric multiferroics. (image adapted from Ref. 7)

1.1.1 **Multiferroics through history**

The early years of multiferroics were mostly linked to the *magnetoelectric (ME) effect*: the interplay between magnetic and electric dipole moments. However, the magnetoelectric family of materials is much broader than what nowadays we came to know and understand as multiferroics. But let us see at first how it all started.

Surprisingly enough, for more than a century since the first report of magnetoelectric effect by Röntgen in 1888,[8] both magnetoelectricity and multiferroicity were neglected by the scientific community. Only a few isolated reports of magnetoelectrics or multiferroics appeared during the years, until the so-called "Revival of the magnetoelectric effect" in 2000s.[1,9,10]

The first reported study related to the magnetoelectric effect was, as mentioned above, by Röntgen in 1888, who observed magnetization emergence in a moving dielectric at the presence of external electrical field.[8] A few years later, in 1894, Pierre Curie predicted the possible existence of magnetoelectric effect in crystals, by the use of symmetry considerations.[11] The

reverse magnetoelectric effect, or else the polarization emergence in a moving dielectric at the presence of external magnetic field, was published in 1905 by Wilson.[12] However, only in 1926 the term "magnetoelectric effect" was stated for the first time by Debye.[13] The essential turn though occurred with the introduction of the broken space- and time-reversal symmetry by Dzyaloshinskii in 1959, as a prerequisite for the manifestation of the magnetoelectric effect.[14] In the latter publication, he predicted the occurrence of the magnetoelectric effect in antiferromagnets (AFM), namely Cr_2O_3, for which a year later was experimentally demonstrated by Astrov.[15]

Before we continue with the facts that led to what nowadays is understood as multiferroicity, it would be helpful to understand what was meant by the term "ferroic" property or material. The prefix "ferro-", meaning "iron" in latin, was initially used in "ferromagnets", materials that present spontaneous magnetic moment, as a courtesy to iron.[16] By spontaneous, it is meant that the magnetization appears in the material intrinsically, at the absence of an external magnetic field. Switching of the magnetic moments can occur at the presence of an external field. As an analogy to the spontaneous magnetization in ferromagnets, the term "ferroelectrics" was used for the first time by Schrödinger in 1912, for materials that present spontaneous polarization (ferroelectrics will be presented in more detail in Section 1.2).[17] During the 1960s, Aizu - the first to use the term "ferroic" - in a series of publications, presented all possible ferroelectric,[18,19] ferroelastic[20] and ferromagnetic[21] species, based on crystal symmetry analysis, as well as the possible coexistence of those three different ferroic properties.[21] Newnham *et al*.[22,23] further on, classified ferroics, considering as *primary ferroic properties*: ferromagnetism, ferroelectricity and ferroelasticity. Finally, the first experimental observation of electric field-induced magnetization rotation by 90° was achieved by Ascher *et al*. in 1966, who studied the boracite $Ni_3B_7O_{17}I$.[24]

Unfortunately, in spite of all the significant advances during 1960s and 1970s, the possibility of combined ferroic properties was left aside till 1990s. The main reason was that the family of perovskites, one of the main crystal structures studied among ferroic materials, only seldom share simultaneously magnetic and ferroelectric (FE) properties.[6] The reappraisal of the matter was done by Schmid in 1994, who introduced the term "multiferroics", as "those having two or more primary ferroic properties in the same phase"[25] (Figure 1.1), followed by Spaldin (as Hill at that time)[9] in 2000 and Khomskii[10] in 2001, both pointing out the reasons for the existence of so few single-phase magnetoelectric multiferroics (see Section 1.1.3.1).

During the coming years, significant contributions in the microscopic quantum level, as well as experimental breakthrough in various techniques, led to numerous discoveries of multiferroic

materials. In 2007, Cheong and Mostovoy reintroduced the classification of ferroelectrics in proper and improper,[26] and their role in the wider family of multiferroics. Finally, Khomskii in 2009 established the classification of multiferroics in Type I and II, depending on the origin and/or the microscopic mechanisms of the magnetoelectric coupling.[27]

Currently, the field of multiferroics has attracted more and more researchers, from both fundamental theoretical and experimental physics, as well as the radiant world of applications. New exotic physics concepts have been introduced, such as monopoles, vortices, skyrmions and electromagnons, the latter being one of the main subjects of this thesis.

1.1.2 **Magnetoelectric coupling in single-phase multiferroics**

Although there is great progress in the field of composite multiferroics, by engineering heterostructures of distinct ferroic materials, presenting substantially strong magnetoelectric coupling,[28,29] in the current thesis the main focus will be *single phase magnetoelectric multiferroics*.

In this section, the magnetoelectric coupling in single-phase multiferroics will be discussed, from the point of view of both phenomenological and quantum-level approaches. The first describes the comprehension of the coupling by means of the *Landau phenomenological theory* and the concept of the *order parameter*. The second can be as a first approach divided into two different microscopic mechanisms: the *spin-orbit* and the *spin-lattice coupling*.

1.1.2.1 Landau phenomenological approach

The primary ferroic properties can be described in terms of symmetry analysis, as mentioned above. The break of symmetry related to each of them can be represented by the so called order parameter, whose value goes from zero to non-zero at the occurrence of the phase transition.[30] For example, ferroelectricity is characterized by space-inversion symmetry breaking and the corresponding order parameter is polarization *P*, whereas ferromagnetism breaks the time-reversal symmetry and magnetization *M* is the corresponding order parameter.

Based on Landau phenomenological approach on phase transitions,[1,30] the coupling of the ferrorelectric and magnetic contributions in magnetoelectric multiferroics can be expressed by the expansion of the free energy:

$$F(\boldsymbol{E},\boldsymbol{H}) = F_o - P_i^S E_i - M_i^S H_i - \frac{1}{2}\varepsilon_o \varepsilon_{ij} E_i E_j - \frac{1}{2}\mu_o \mu_{ij} H_i H_j - \\ -\frac{1}{2}\beta_{ijk} E_i H_j H_k - \frac{1}{2}\gamma_{ijk} H_i E_j E_k - \ldots \qquad 1.1$$

where F_o is the ground state free energy, P^S and M^S the spontaneous polarization and magnetization respectively, E and H the electric and magnetic field respectively, $\varepsilon_0\varepsilon_{ij}$ and $\mu_0\mu_{ij}$ the dielectric permittivity and magnetic permeability, respectively, and β_{ijk} and γ_{ijk} third-order tensor coefficients describing quadratic ME coupling.[1] Derivation of the above free energy over the electric field E and magnetic field H, results in the expressions for polarization P and magnetization M, respectively:

$$\boldsymbol{P}_i(\boldsymbol{E},\boldsymbol{H}) = -\frac{\partial F}{\partial E_i} = \boldsymbol{P}_i^S + \varepsilon_0\varepsilon_{ij}\boldsymbol{E}_j + \alpha_{ij}\boldsymbol{H}_j + \frac{1}{2}\beta_{ijk}\boldsymbol{H}_j\boldsymbol{H}_k + \gamma_{ijk}\boldsymbol{H}_i\boldsymbol{E}_j - \ldots \quad 1.2$$

$$\boldsymbol{M}_i(\boldsymbol{E},\boldsymbol{H}) = -\frac{\partial F}{\partial H_i} = \boldsymbol{M}_i^S + \mu_0\mu_{ij}\boldsymbol{H}_j + \alpha_{ij}\boldsymbol{E}_j + \beta_{ijk}\boldsymbol{H}_j\boldsymbol{E}_\iota + \frac{1}{2}\gamma_{ijk}\boldsymbol{H}_i\boldsymbol{E}_j + \ldots \quad 1.3$$

where α_{ij} is the linear magnetoelectric coefficient, which corresponds to magnetic field-induced polarization or electric field-induced magnetization, as shown in equation 1.4:

$$\alpha_{ij} = \frac{\partial \boldsymbol{P}_i}{\partial \boldsymbol{H}_j} = \frac{\partial \boldsymbol{M}_i}{\partial \boldsymbol{E}_j} \quad 1.4$$

In addition, the upper bound on the magnetoelectric susceptibility $a_{ij}^2 \leq \varepsilon_0\mu_0\varepsilon_{ij}\mu_{ij}$,[31] restricts large ME coupling in multiferroics, where large permittivity and high permeability simultaneously occur.

Here, it is important to highlight that even though higher order magnetoelectric coupling coefficients exist, as seen above, as well as the dynamic magnetoelectric coupling (discussed in Section 1.1.4), in the vast majority of multiferroics literature when referred to the linear magnetoelectric coupling, the term "linear" is omitted. Furthermore, one should not identify the linear magnetoelectric effect with multiferroicity. Not all multiferroic materials exhibit linear magnetoelectric coupling, and not all materials exhibiting linear magnetoelectric coupling are multiferroics. For example, higher order magnetoelectric coupling may occur in materials, where there is no simultaneous breaking of space-inversion and time-reversal symmetries, such as in rear earth molybdates $R_2(MoO_4)_3$, which present magnetoelectric effect in the paramagnetic phase[32] or in multiferroic $YMnO_3$, where in the AFM phase the time-reversal symmetry is not broken and piezomagnetic coupling plays the role.[33]

1.1.2.2 Quantum-level microscopic mechanisms

A significant remark on the symmetry aspect in multiferroics is that one single magnetic moment breaks time-reversal symmetry, but not necessarily space-inversion,[4,5] which is also related to the fact that there are very few magnetic FEs (discussed in Section 1.1.3.1). However,

the spatial distribution of multiple magnetic moments can break the space-inversion symmetry, leading to the emergence of polarization.

The understanding of the underlying microscopic mechanisms that lead to magnetoelectric coupling is essential for the engineering of novel single-phase magnetoelectric multiferroics, since the ones already existing in nature are very limited. Complex interactions related to magnetic, ionic and electronic contributions may occur in the majority of the multiferroic materials, however one can distinguish two main types of coupling mechanisms: *spin-orbit* and *spin-lattice*.

The main difference between the two mechanisms is that in the former, the magnetically-induced polarization is related to the *direction* of the magnetic moments, thus the magnetic easy axis or plane, whereas in the latter, the polarization emerges as a result of the *crystal symmetry*. In addition, usually *spiral magnetic order* corresponds to spin-orbital coupling, whereas *collinear magnetic order* to *spin-lattice* coupling (see Section 1.1.3.2). Naturally, combination of the two operations may occur, which might hinder the efforts of clear understanding of the origin of magnetoelectric coupling in particular materials.

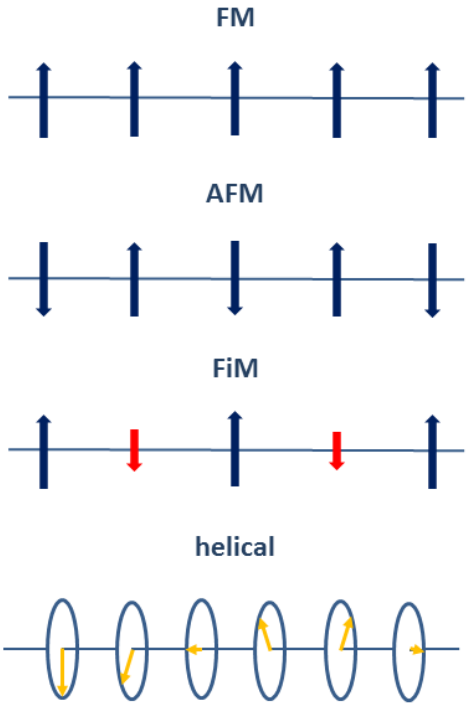

Figure 1.2 The basic magnetic orders: FM, AFM, FiM and helical.

Before we proceed with the detailed explanation of the microscopic coupling mechanisms, a brief reminder on spin ordering is necessary. Magnetic ordering in the crystal lattice arises from exchange interactions between partially filled *d* or *f* shells of *transition metal* or *rare-earth* ions. For a collinear spin alignment, the *Heisenberg exchange interaction* is of main importance, whereas in spiral spin order, the *magnetic frustration* related to spin-orbit coupling accounts for these fascinating spin formations.[4,5,27] A few basic magnetic structures are: ferromagnetic (FM), antiferromagnetic (AFM), ferrimagnetic (FiM) and helical (Figure 1.2).

Spin-orbit coupling

One of the two mechanisms that allow magnetoelectric coupling is the spin-orbit interaction. There are two main examples worth mentioning within the spin-orbit coupling mechanism: *Dzyaloshinskii-Moriya interaction* and *spin-dependent metal-ligand hybridization*.

At the end of 1950s, during the studies on the AFM Cr_2O_3, the historically first material to exhibit magnetoelectric coupling, Dzyaloshinskii suggested that antisymmetric exchange interaction can induce weak FM moment in antiferromagnets.[34] One year later, Moriya showed that this is merely a result of spin-orbit interaction.[35] Due to the great significance of their findings for the wide family of magnetic systems, this interaction was called *Dzyaloshinskii-Moriya (DM) interaction*.

Let us consider two magnetic ions separated by a non-magnetic one, say oxygen (Figure 1.3). The three atoms form straight bonds with 180° angle between them. Due to a relativistic correction to the superexchange interaction between the magnetic ions, oxygen moves away from its position, bending the bonds with its neighboring atoms. The Hamiltonian of such interaction can be formulated as:[36,37]

$$\boldsymbol{H}_{DM} = \boldsymbol{D}_{ij} \cdot (\boldsymbol{S}_i \times \boldsymbol{S}_j) \quad 1.5$$

where $\boldsymbol{D}_{ij}$ is the coefficient of the DM interaction, determining the amplitude of the oxygen displacement and perpendicular to the atoms plane, and $\boldsymbol{S}_i$, $\boldsymbol{S}_j$ the spins of the magnetic ions at sites *i* and *j*. Due to the displacement of the intermediate oxygen, a local polarization is induced, having the following expression relative to the spins:

$$\boldsymbol{P}_{DM} = \boldsymbol{e}_{ij} \times (\boldsymbol{S}_i \times \boldsymbol{S}_j) \quad 1.6$$

where $\boldsymbol{e}_{ij}$ is the unit vector that points from site *i* to *j*.

Another example of spin-orbit coupling based magnetoelectric coupling in single-phase materials is that of the *spin-dependent metal-ligand hybridization*, else known as *p-d* hybridization, due to the hybridization between metal's *d* and anion's *p* orbitals.[38] This second order spin-orbit coupling mechanism is related to a single magnetic moment and its interaction with the surrounding anions, say oxygens. The induced polarization is a result of all the bonds between the magnetic ion and its neighboring anions (Figure 1.3) and it can be expressed as:

$$\boldsymbol{P}_{p-d} = \sum_i (\boldsymbol{e}_i \cdot \boldsymbol{S}_i)^2 \boldsymbol{e}_i \quad 1.7$$

where the summation is over all different bonds and $\boldsymbol{e}_i$ the bond direction.

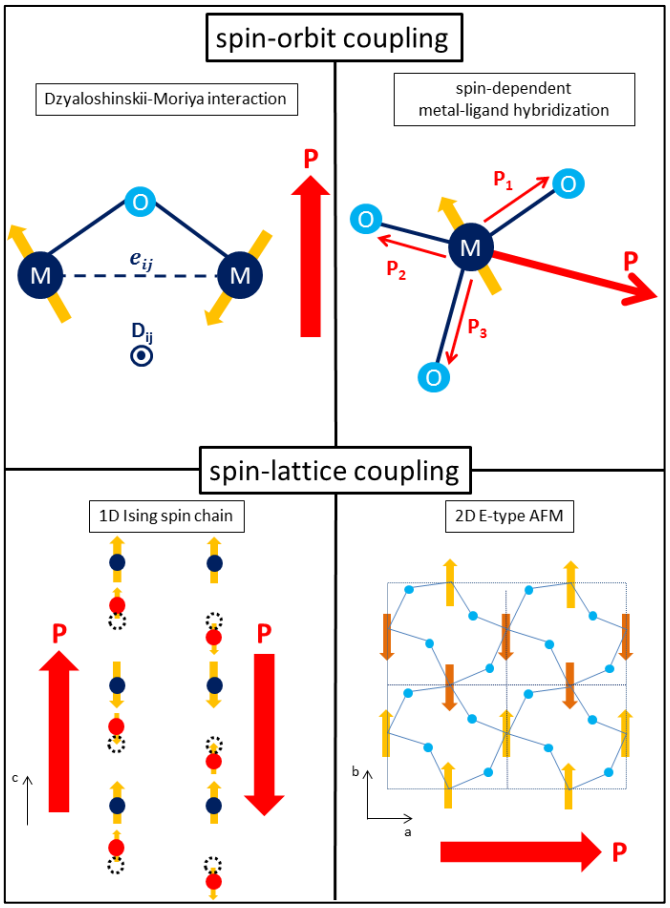

Figure 1.3 Schematic summary of the microscopic magnetoelectric coupling mechanisms (schemes adapted from Ref. 5, 41, 270)

A great advantage of the spin-orbit coupling based magnetoelectric effect is that the spins are susceptible to external magnetic fields, thus the materials possessing it can easily present magnetically driven polarization, which can be strongly influenced by external magnetic field.

Spin-lattice coupling

The weak spin-orbit coupling in the compounds with 3*d* transition metals, and the substantially low critical temperatures and polarization magnitudes related to the spin-orbit coupling led to the need for an alternative mechanism which would still take advantage of the magnetically-induced break of inversion symmetry. Since most materials with spin-orbit originated magnetoelectric coupling correspond to non-collinear magnetic structures (spiral, cycloidal, helical),[39] Sergienko *et al*. suggested a new mechanism of creation of polarization in the collinear E-type AFM $HoMnO_3$.[40] Instead of the spin-orbit coupling antisymmetric superexchange interaction, a symmetric exchange striction (with a Hamiltonian $H \propto \sum_{ij} J_{ij} (\boldsymbol{S}_i \boldsymbol{S}_j)$, where $\boldsymbol{S}_i$, $\boldsymbol{S}_j$ are the spins of the magnetic ions at sites *i* and *j*, and J_{ij} is the exchange interaction coefficients between the two spins) related to spin-lattice interaction was proposed. Hereby, two examples of such spin-lattice coupling will be mentioned: *one-dimensional Ising spin chain* and *two-dimensional E-type AFM*.

The idea of a symmetric exchange striction mechanism responsible for magnetically-driven polarization in the case of *one-dimensional Ising spin chain* was formulated first by Cheong and Mostovoy in 2007.[26] However, the first experimental demonstration of such a system was done by Choi *et al*. one year later,[41] for Ca_3CoMnO_6, which presents an up-up-down-down (↑↑↓↓) quasi-collinear spin order along *c*-axis. The magnetic moments originate from both Co^{2+} and Mn^{4+} ions, whose positions alternate along the chain, breaking the inversion symmetry of magnetic sites and inducing polarization along the same axis (Figure 1.3). Due to the symmetric

superexchange interaction, parallel spins (↑↑) result in contraction, whereas antiparallel (↑↓) in repulsion. The heterovalency of the magnetic ions is essential for the emergence of polarization, since the latter is proportional to the divergence of the exchange interaction ***J*** between the magnetic sites, which in turn is inextricably linked to the lattice symmetry.

As mentioned above, the general idea for the induction of polarization by collinear spin order was introduced with the orthorhombic perovskite E-type antiferromagnet $HoMnO_3$.[40] The magnetic cations of Mn^{3+} form antiferromagnetically alternating zigzag chains that lie in the *ab*-plane, with the spins pointing along *b*-axis. The polarization is induced along *a*-axis by the combination of both FM and AFM exchange strictions, which cause oxygen displacements and buckling of the oxygen octahedral (Figure 1.3).[40,42] An extra contribution to the total polarization was reported by Lee *et al*.,[43] which originates from the Ho-Mn symmetric exchange striction and gives rise to a *c*-axis polarization component. Note that the main difference between the one-dimensional spin chain and the E-type antiferromagnets concerning spin-lattice coupling is that the former requires heterovalent magnetic ions, whereas the latter isovalent.

1.1.3 **Classification of multiferroics**

Due to Kohmskii's prominent legacy in the field of multiferroics, we can, as a first approach, divide them in two classes: *type-I* and *type-II* multiferroics (Figure 1.4).[27] The main difference between them is that the two distinct ferroic orders occur at different critical temperatures in type-I, whereas in type-II occur simultaneously, in other words, the one induces the other. Below, the principal subclasses among the two families will be presented, together with a few examples of multiferroic materials.

1.1.3.1 Type-I Multiferroics

In this class of multiferroics, we often encounter enhanced FE properties. The critical temperature T_C at which occurs the FE phase transition is higher than the FM or AFM one, T_C or T_N respectively. Type-I multiferroics were among the first studied, since their FE properties were well known. Their main advantage is that in many cases they present multiferroic properties above room temperature (RT). However, the magnetoelectric coupling between ferroelectricity and magnetism is mostly weak. Hereby, four main subclasses will be described, based on distinct origins of ferroelectricity: *perovskites*, *lone-pair*, *charge ordering* and *geometric* ferroelectricity.

Multiferroic perovskites

Among the perovskite structures (ABO_3), one can come across a plethora of FE and magnetic phases, however not combined (more on perovskites in section 1.2.2). The empty *d* shells of the transition metal ions sitting in the B sites of the FE perovskites are usually necessary for inducing a non-centrosymmetric structure (thus FE polarization) by forming covalent bonds with the neighboring oxygens. On the other hand, the partially filled *d* shells of the transition metal ions are fundamental for the emergence of magnetic moment. This is the notorious "d^0 vs d^n problem",[44] where essentially both requirements cannot meet in the same material. One solution is the mixed perovskites, where d^0 and d^n metal ions belong to distinct oxygen octahedral cages (Figure 1.4), however presenting very weak magnetoelectric coupling. However, some cases do not follow the d^0 rule, such as $Sr_{1-x}Ba_xMnO_3$ does not follow the d^0 rule, here both ferroelectricity and magnetism is caused by the same Mn^{4+} cation.[45]

Lone-pair ferroelectricity

The considered "model" multiferroic $BiFeO_3$ with perovskite structure belongs in this multiferroic subclass. Bi^{3+} cation possesses $6s^2$ electrons that do not form chemical bonds. The hybridization between its 6*s* and 6*p* states results in distortion of the spherical symmetry of the shell, thus inducing high electric polarizability (Figure 1.4).[46] An AFM spiral order is caused by the magnetic moments of the Fe cations.

Charge ordering ferroelectricity

This subcase of type-I multiferroics is mostly observed for heterovalent transition metal compounds, where the cations' sites and bonds order forming an intermediate FE state (Figure 1.4).[47] Examples of materials presenting such behavior are $Pr_{1/2}Ca_{1/2}MnO_3$,[47] $TbMn_2O_5$,[48] and $LuFe_2O_4$.[49]

Geometric ferroelectricity

As expected by the title of this subclass, the FE polarization is generated by ionic geometry transformations, such as in the case of $YMnO_3$, where the triangular layered MnO_5 blocks tilt in a way that produce huge displacements among O^{2-} anions and Y^{3+} cations (Figure 1.4).[50]

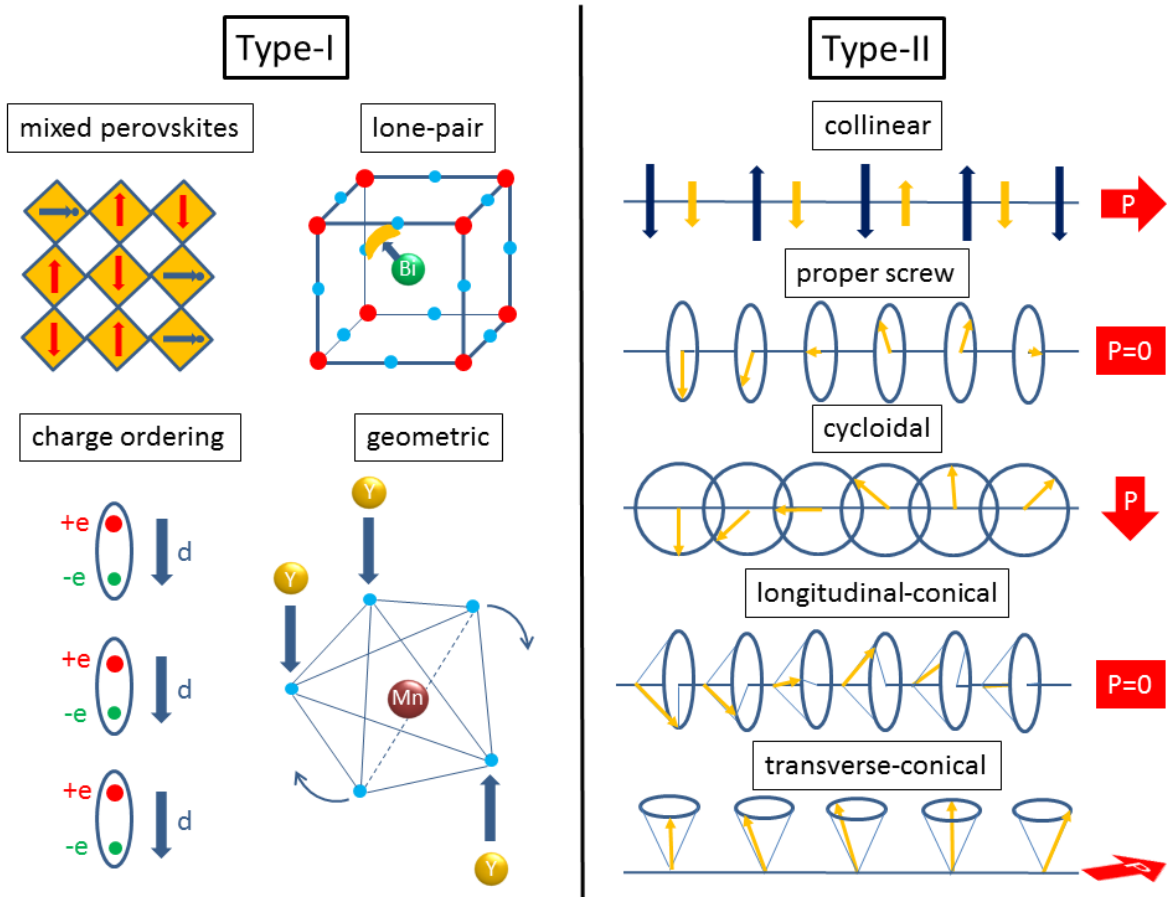

Figure 1.4 Classification of multiferroics (schemes adapted from Ref. 27, 39)

1.1.3.2 Type-II Multiferroics

The most thrilling attribute of type-II multiferroics is the fact that the magnetic order induces the FE polarization, often resulting in stronger magnetoelectric coupling than for the case of type-I multiferroics. Naturally, the critical temperature of the FE phase transition lies below the one of the magnetic phase transition, or the two coincide. Due to this confining interaction between the magnetic moments and the polarization, the latter becomes susceptible at magnitude, rotation and flipping changes, at the presence of external magnetic fields. However, the values of spin-induced FE polarization are approximately two or three orders lower than those observed in type-I multiferroics. As a reminder, another drawback of this class is the typically low critical temperatures that usually are required to achieve the magnetic ordering.

Since the spin structure is undoubtedly fundamental for type-II multiferroics, the main two subclasses are related to two basic spin orders: *spiral* and *collinear magnetic structures*. Indeed, the *spin-orbit* and *spin-lattice* coupling mechanisms (section 1.1.2.2) correspond roughly to the *spiral* and *collinear* spin orders respectively.

Multiferroics with spiral magnetic structures

The tendency of the magnetic moments to order in spirals could be described as a parallelism with the spin-flop transition in magnetic systems.[27] In such case, the minimization of energy occurs when the spins lie perpendicular to the magnetic field. Thus, canting of the spins is energetically favored in some systems, resulting in spiral structures. There exist various spin spiral geometries, however the main ones are: proper screw, cycloidal, longitudinal conical and transverse-conical (Figure 1.4).[4,39] As mentioned above, the magnetoelectric coupling in spiral magnetic structures is related to the spin-orbit coupling. Since in spin-orbit coupling mechanism the polarization direction is determined by the magnetic easy axis or plane, each spin configuration gives rise to different directions of the polarization vector, as can be seen in Figure 1.4.

A few examples of compounds with spiral spin order are: RMnO$_3$ (R=Tb, Dy, Eu$_{1-x}$Y$_x$) [51,52] and the famous BiFeO$_3$[53,54] presenting cycloidal spin order, CoCr$_2$O$_4$ transverse-conical,[55,56] and the Y-type hexaferrite Ba$_2$Mg$_2$Fe$_{12}$O$_{22}$ forming longitudinal-conical spin structure with P=0 which in external magnetic field transforms to transverse-conical, where P≠0.[57,58] Note that BiFeO$_3$ belongs to type-I multiferroics, but spiral spin structure enhances its static polarization in this material by 3% below T_N.[59]

Multiferroics with collinear magnetic structures

Like mentioned above, the symmetric exchange interaction instead of the antisymmetric one drives collinear magnetic systems to a FE state (see section 1.1.2.2). Here, spin-orbit coupling doesn't necessarily play a role in the magnetoelectric coupling. Heisenberg exchange striction in combination with the break of inversion symmetry by the spin order induces polarization, thus crystal symmetry dominates the coupling in the collinear spin structures.

Apart from the examples mentioned in section 1.1.2.2, such as HoMnO$_3$ and Ca$_3$CoMnO$_6$, a series of collinear antiferromagnets has drawn the attention, like the orthorhombic Ising antiferromagnet DyFeO$_3$,[60] the rare-earth double-perovskites R$_2$CoMnO$_6$ and R$_2$NiMnO$_6$,[61,62] and the hexagonal Ni$_3$TeO$_6$ with a colossal magnetoelectric effect,[63] which will be discussed in more detail in the current thesis (see section 3.3).

1.1.4 **Dynamical Magnetoelectric Coupling**

The linear static magnetoelectric coupling was described in section 1.1.2.1. Now it is time to see what happens away from the static regime in multiferroic systems. Naturally, the same microscopic mechanisms mentioned for the linear magnetoelectric coupling are responsible for the dynamical magnetoelectric coupling, but in this case the order parameters of magnetization and polarization are not static, but *oscillatory*.

In the current Section, a brief introduction to the concept of *dynamical magnetoelectric coupling* will be presented, followed by the description of its close relative, the *directional dichroism*, and finally, the novel elementary excitations of *electromagnons*, as "carriers" of the dynamical magnetoelectric coupling.

The optical (dynamical) magnetoelectric effect

Let us inspect the dynamical magnetoelectric coupling through the classical electromagnetism and the linear response theory. Since we refer to a dynamical behavior, it is convenient to follow the *frequency domain (ω)*. [64–70] However, it is preferable to start from the static case.

At the absence of magnetoelectric coupling, the classical electromagnetism relations of polarization and magnetization to the respective medium fields are: $\boldsymbol{P} = \chi^{\mathrm{e}}\boldsymbol{E}$ and $\boldsymbol{M} = \chi^{\mathrm{m}}\boldsymbol{H}$ (in cgs system), where χ^{e} and χ^{m} are the dielectric and magnetic susceptibilities, respectively. The magnetization and polarization currents are given by: $\boldsymbol{J}_{\mathrm{m}} = \boldsymbol{\nabla_r} \times \boldsymbol{M}$ and $\boldsymbol{J}_{\mathrm{e}} = \partial_t \boldsymbol{P}$, where $\boldsymbol{r}$ and t correspond to the space- and time-related derivatives. However, in the case of simultaneous break of time-reversal and space-inversion symmetries, the two terms are coupled, yielding:[71]

$$\boldsymbol{P} \sim \boldsymbol{M} \times (\boldsymbol{\nabla_r} \times \boldsymbol{M}) \overset{r \leftrightarrow t}{\longleftrightarrow} \boldsymbol{M} \sim \boldsymbol{P} \times \partial_t \boldsymbol{P} \qquad 1.8$$

Here, the interlocked components of $\boldsymbol{P}$ and $\boldsymbol{M}$ appear in terms of symmetry considerations. $\boldsymbol{P}$ is related to a spatial divergence of the magnetic moments $(\boldsymbol{\nabla_r} \times \boldsymbol{M})$, and $\boldsymbol{M}$ to a time-dependent polarization $(\partial_t \boldsymbol{P})$.

Analogously as described for the linear magnetoelectric coupling in equations 1.2 and 1.3, extra contributions appear at the polarization and magnetization relations above, which can be expressed as:

$$\boldsymbol{P}_i^{\omega} = \chi_{ii}^{\mathrm{e}}(\omega)\boldsymbol{E}_i^{\omega} + \alpha_{ij}^{\omega}\boldsymbol{H}_j^{\omega} \qquad 1.9$$

$$\boldsymbol{M}_j^{\omega} = \chi_{jj}^{\mathrm{m}}(\omega)\boldsymbol{H}_j^{\omega} + \alpha_{ji}^{\omega}\boldsymbol{E}_i^{\omega} \qquad 1.10$$

where i,j correspond to spatial coordinates, and α_{ij}^{ω} is the dynamical magnetoelectric coefficient. The difference between the *linear* and the *dynamical* case is that the terms $\boldsymbol{P}_i^{\omega}$ and $\boldsymbol{M}_j^{\omega}$ correspond to the *oscillating polarization* and *magnetization*, which are induced by the *oscillating electric* and *magnetic fields* $\boldsymbol{E}_i^{\omega}$ and $\boldsymbol{H}_j^{\omega}$, respectively. Interestingly, the latter can be identified as the electric and magnetic components of the electromagnetic radiation. Thus, the dynamical magnetoelectric coupling is, in fact, an *optical magnetoelectric effect*. [64–70]

It is of high importance to stress the significance and elegance of expression 1.8, since it depicts the very essence of the magnetoelectric coupling.[71] However, up to this point, the spin-induced polarization, in materials that do not possess inherently broken space-inversion symmetry, accounts for the manifestation of the magnetoelectric effect in the vast majority of magnetoelectric multiferroic materials, namely the type-II multiferroics. There is no significant experimental evidence showing the reciprocal effect, where the magnetic order is induced by a time-dependent polarization in non-magnetic systems, apart from the case of possible ferroelectrically-induced paramagnetism in triglycine sulfate (TGS) [72,73] Here, one should not confuse the weak ferromagnetism induced by FE order in say antiferromagnets (zero macroscopic magnetization),[74,75] with the otherwise paramagnetic or diamagnetic systems presenting ferroelectric-induced magnetization.[72,73] The possibility of the occurrence of a phonon-Zeeman effect, scilicet the Zeeman splitting of degenerate phonon modes at the presence of an external magnetic field, was formulated recently by Juraschek *et al*..[71] They suggest that ionic loops of circular motions of the ions can generate macroscopic magnetic moment via optically-driven phonons. Like intrinsic polarization is not required for the spin-induced FEs, intrinsic magnetism should not be needed for the polar-driven magnetization.

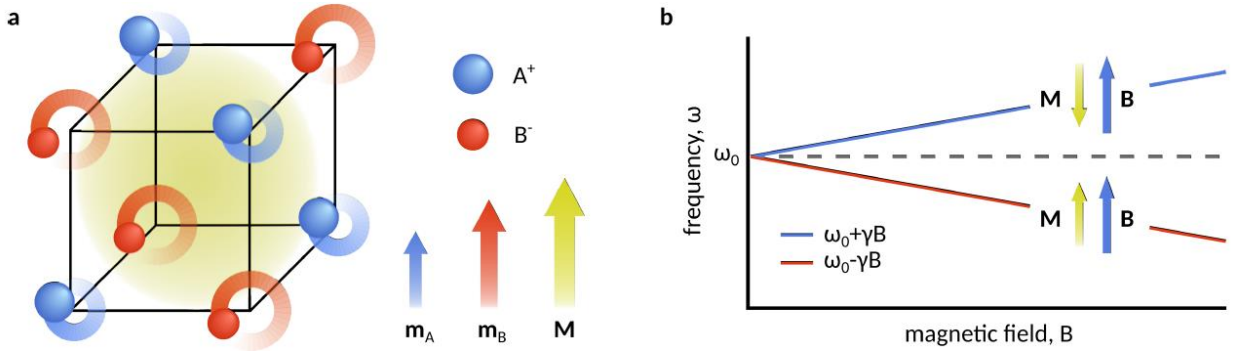

Figure 1.5 (a) The theoretically predicted reciprocal effect of the time-dependent polarization-induced magnetization, by the vibration of charges in an otherwise non-magnetic crystal lattice. (b) The Zeeman phonon splitting at the presence of an external magnetic field $\boldsymbol{B}$.[71]

Directional Dichroism

A concomitant effect alongside the optical magnetoelectric coupling is the phenomenon of *directional dichroism*, defined as the materials' different optical response to counterpropagating light.[67,68] At first, it was theoretically proposed by Brown *et al*. in 1963,[76] mentioned as *gyrotropic* or *nonreciprocal birefringence*, suggesting the possible observation of AFM domains. A few years later, Hornreich & Shtrikman related the phenomenon to the magnetoelectric effect.[64] Alas, only in the 1990s and 2000s there were a few experimental attempts for detecting it, mostly corresponding to rather weak effects and above near infrared range of the electromagnetic spectrum.[65,77–79] Nonetheless, the *terahertz* revolution of the 2000s promoted the first demonstration of the directional nonreciprocity of light transmission in multiferroics in the *terahertz* range in 2011 by Kezsmarki *et al*. (Figure 1.6).[67]

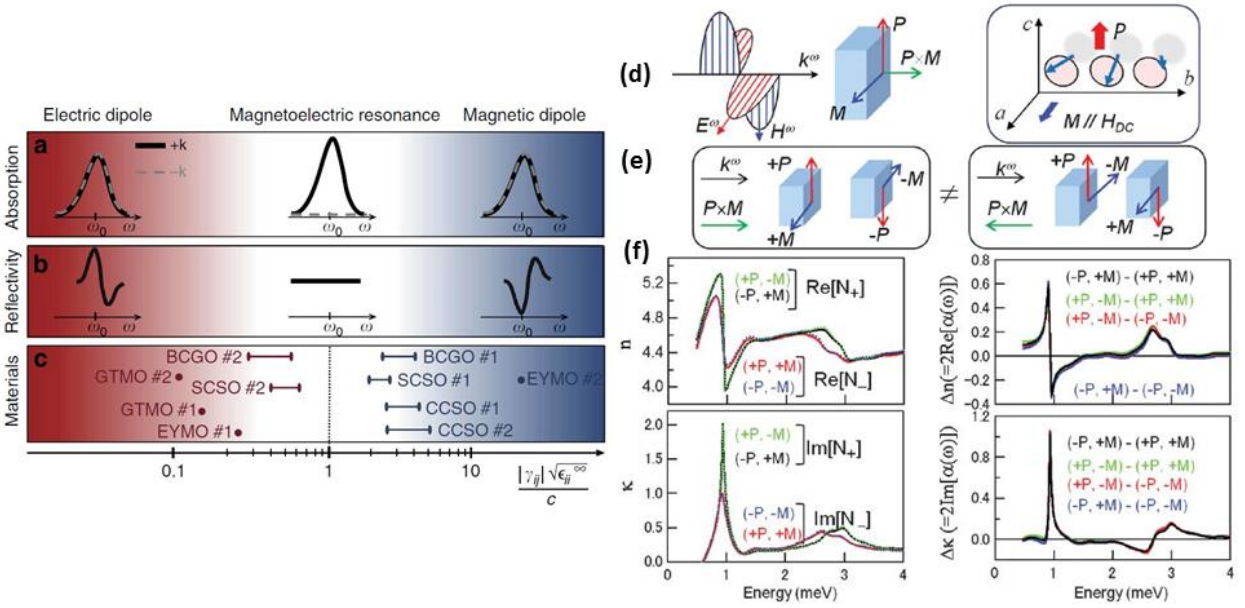

Figure 1.6 The effect of directional dichroism. (a) Absorption and (b) reflectivity modes, as seen in an electric dipole, magnetoelectric resonance and magnetic dipole, for counter-propagating waves. (c) A selection of materials and their behavior to counter-propagating waves. (d) The oscillating electric $\boldsymbol{E}^{\omega}$ and magnetic fields $\boldsymbol{H}^{\omega}$ of the propagating light and the induced cross-coupled magnetization $\boldsymbol{M}$ and polarization $\boldsymbol{P}$. On the right side, the *b*-*c* cycloidal structure induces static polarization $\boldsymbol{P}$ along *c*-axis. (e) The different configurations of the cross-coupled $\boldsymbol{P}$ and $\boldsymbol{M}$ for counter-propagating waves. (f) Absorptions in the complex refractive index for the different configurations shown in (e) for $Gd_{0.5}Tb_{0.5}MnO_3$, and the respective changes Δn and Δk. (images taken from R. 69, 80)

The significance of the latter work is that this oscillating behavior of polarization and magnetization is manifested in the hybrid elementary excitations known as *electromagnons*, which very often lie in the terahertz or far infrared region of the spectrum. Very soon, further evidence of the existence of directional dichroism in multiferroics was reported,[68,69,81] and the inextricable correlation of the *directional dichroism* to the *optical (dynamical) magnetoelectric*

effect was established. Note though that there is no necessary two-way relation between the two, in other words, a material presenting directional dichroism is not by definition multiferroic.

Continuing with the phenomenological description of the optical magnetoelectric effect from equations (9) and (10), one can arrive to the following expression for the index of refraction:[69]

$$N_{i,j}^{\pm} \approx \sqrt{\varepsilon_{ii}(\omega)\mu_{jj}(\omega)} \pm \frac{1}{2}\left[\chi_{ji}^{\mathrm{me}}(\omega) + \chi_{ij}^{\mathrm{em}}(\omega)\right] \qquad 1.11$$

The $\pm$ sign in the second part of the equation is the explicit manifestation of directional dichroism, corresponding to the $\pm\boldsymbol{k}$ wavevectors of the light propagation, and relating it to the magnetoelectric susceptibilities. The right-hand rule stands for the polarization vectors of the electromagnetic wave: $\boldsymbol{E}^{\omega}$, $\boldsymbol{H}^{\omega}$, the directions of the electric and magnetic components, respectively.

Electromagnons

One of the main interests of the current thesis is the dashing world of *electromagnons*. As the very word indicates, the electromagnons are *electro*-active *magnons*,[82] namely collective spin and lattice excitations that couple the dielectric and magnetic properties. In that fashion, like seen above in the refractive index expression 1.11, they contribute to both the dielectric and magnetic susceptibilities.

The first report about the possibility of such coupling was done at the end of 1960s by Bar'yakhtar & Chupis,[83,84] referring to them as "seignette-magnons". Smolenskii & Chupis in 1982 published a review on ferroelectromagnets, reintroducing the potential of such excitations, naming them "ferroelectromagnons".[85] But only in 2006, the first experimental evidence of electromagnons was demonstrated by Pimenov *et al*. in $R\mathrm{MnO_3}$ via terahertz transmittance experiments.[82] Soon it was followed by the far-infrared studies of $\mathrm{Eu_{0.75}Y_{0.25}MnO_3}$, revealing spectral weight transfer from the low-frequency polar phonons to the terahertz-range magnons.[86] Such behavior was theoretically predicted by Katsura *et al*.[87] for the spin-orbit interaction induced polarization in helical magnets, attributing it to the coupling between the lattice and spin excitations, thus the electromagnons.

Since the electromagnons originate from the collective spin and lattice excitations, all the possible quantum-level microscopic mechanisms responsible for the multiferroic coupling mentioned in section 1.1.2.2 are undoubtedly related to their generation. To remind the reader, there are two main possible coupling mechanisms: *spin-orbit* and *spin-lattice*. Within the spin-orbit coupling case, the *spin-current* (DM interaction) and the *p-d hybridization* (metal-ligand) can drive the system to a polar phase. Spin-current coupling mostly originates from non-collinear

spin structures and it is a consequence of the *antisymmetric superexchange interaction*. On the other hand, *spin-lattice* interaction appears principally in systems with collinear spin order, where the *symmetric exchange striction* is the parent of the polarization induction. However, in many cases a combination of the above contributions may occur.

The electromagnon frequencies often lie in the terahertz range. In Figure 1.7 one can see the possible activation of electromagnons at the long-wavelength spectroscopy. The example chosen is the case of sinusoidal phase in $RMnO_3$, presenting cyclon (black solid) and extra-cyclon (red dashed) branches in the magnon dispersion curves. The three main quantum-level microscopic mechanisms discussed above are illustrated, with the respective contributions in the wavevector-domain. Note that electromagnons can have wavevector out of Brillouin zone center ($q \neq 0$), if the magnetic structure is modulated (helical), while magnon (AFM resonance) activated in terahertz (THz) or infrared (IR) spectra of unmodulated antiferromagnets has $q=0$.

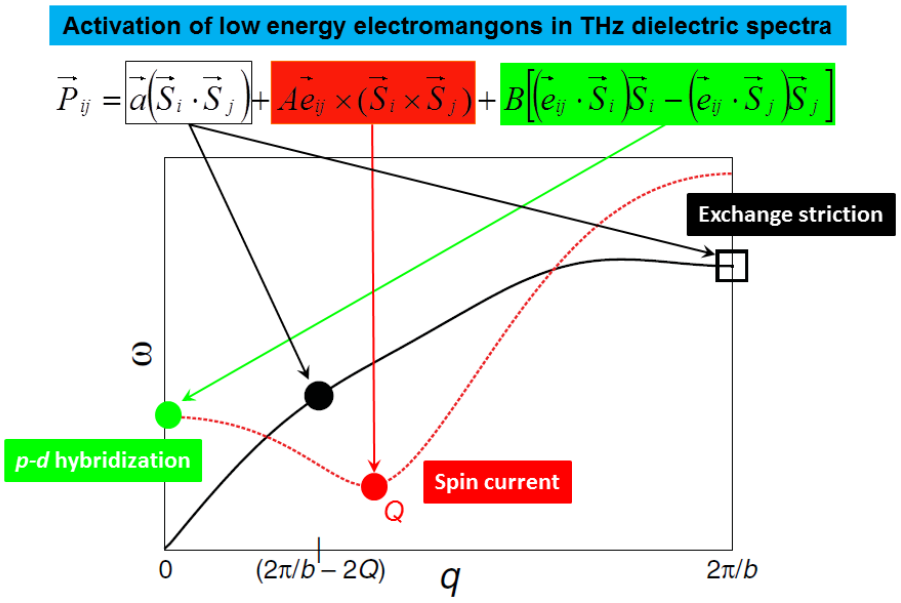

Figure 1.7 Possible activation of electromagnons in the terahertz range of the electromagnetic spectrum. The typical dispersion curves for magnons in the sinusoidal phase of $RMnO_3$ are shown: cyclon (black solid) and extra-cyclon (red dashed). The three main microscopic mechanisms responsible for the electromagnon activation are demonstrated. (image adapted from Ref. 88)

1.2 **Ferroelectrics**

1.2.1 **Principles of ferroelectrics**

FEs correspond to insulating systems, which present two or more stable or metastable states of nonzero electric polarization in the absence of electric field, known as spontaneous polarization.[89–92] The polarization in a bulk or film is organized in domains and, by reversing the applied electric field, switching of the domains' orientation takes place. FEs belong to 10 polar point groups, a subcategory of the 20 non-centrosymmetric piezoelectric point groups.[89]

The FE phenomenon was firstly observed by Valasek in 1920.[93] Initially, the FE research was limited to the study of hydrogen-bonded materials, such as Rochelle salt (Potassium Sodium Tartrate ($NaKC_4H_6O_6.4H_2O$)) and monopotassium phosphate (KH_2PO_4). In 1941, barium titanate's ($BaTiO_3$) FE properties were discovered independently in USA, Japan and Soviet Union and the route for understanding ferroelectricity was simplified.

In a similar way as in the ferromagnets ,[94] the spontaneous polarization disappears above a critical temperature T_C, the crystal goes through a *ferroelectric* to *paraelectric* phase transition, and the static permittivity follows the Curie-Weiss law:[95]

$$\varepsilon(0) \propto \frac{1}{T-T_0}\begin{cases} T_0 < T_C \; for \; 1^{st} \; order \; phase \; transition \\ T_0 = T_C \; for \; 2^{nd} \; order \; phase \; transition \end{cases} \qquad 1.12$$

An important characteristic of FEs is the hysteretic behavior of polarization with the application of an electric field.[96,97] In Figure 1.8, an almost ideal case of hysteresis loop is presented. As the electric field is increased, polarization increases until a certain value, which corresponds to the saturation polarization P_S. By removal of the bias voltage, a large part of the polarized regions maintain their distorted positions and, subsequently, at zero field a remnant polarization P_R is reached. The same behavior is followed for the case of negative bias. The two points where the hysteresis loop meets the voltage axis correspond to the forward and reverse coercive voltages, V^+ and V^- respectively. High values of the coercive field account for easily polarizable materials, which retain their polarization. Finally, the area of the loop provides the work necessary for polarization switching.[96]

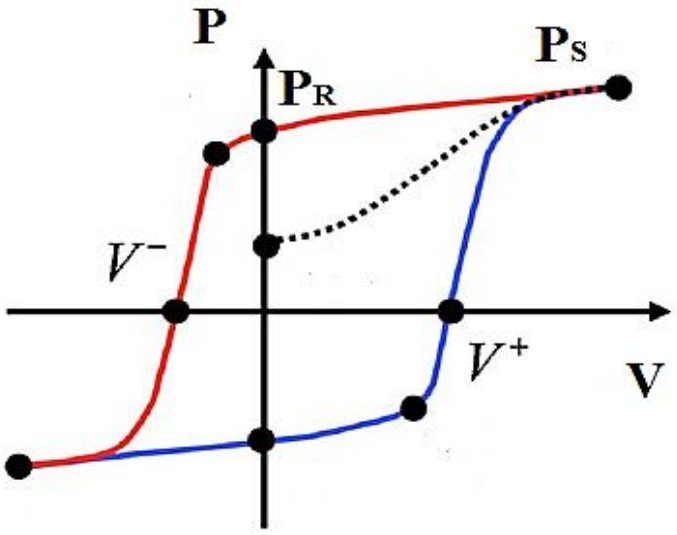

Figure 1.8 Schematic representation of a well-saturated electromechanical hysteresis loop. The two axes represent the applied voltage *V* and the resulting polarization *P*. P_S and P_R correspond to the saturation and remnant polarization, respectively, whereas V^+ and V^- to the forward and reverse coercive voltage, respectively.[96]

1.2.2 **Classification of ferroelectrics**

There are various groups of materials that present FE properties. To name a few: perovskites ($BaTiO_3$, $PbTiO_3$, $BiFeO_3$, $SrTiO_3$), ilmenites ($LiNbO_3$), layered oxide FEs (Aurivillius phases consisting of layered bismuth oxides, Ruddlesden-Popper phases), other FE oxide families (tungsten bronzes, boracites), hydrogen-bonded FEs (KH_2PO_4, Rochelle salt), magnetic FE oxides (hexagonal manganites, such as $YMnO_3$), electronic FEs ($BaBiO_3$, $LuFeO_4$, $YFeO_4$) and FE polymers (PVDF, liquid crystals).[89]

However, the most widely studied structure of FEs is the perovskite (see type-I multiferroics in section 1.1.3.1). Their structure is ABO_3, having cation A at the corners of the unit cell, B at the center and O at the midpoint of each face, creating an oxygen octahedra net, with B at the center of each one of them (Figure 1.9). Based on two main behaviors observed mostly in FE perovskites, the whole family can be divided into two classes: the *displacive* and the *order-disorder ferroelectrics*.

Let us consider a cubic perovskite structure, as an example for the *displacive* FE class. At the paraelectric phase, the structure is centrosymmetric, presenting zero net-polarization. Below T_C, the vertical displacement of central cation B breaks the symmetry of the cubic structure and, by changing the distribution of charge in the unit cell, induces polarization (Figure 1.9**)**.[98] The double-well potential (bottom of Figure 1.9), presents the two stable states (lower energy states) of the spontaneous polarization, which in the paraelectric state becomes a single-well. The displacive FE phase transition is often driven by the so-called *soft mode*, which is related to the instability of the low-frequency phonon, thus its tendency to reach very low frequencies ($\omega \to 0$) close to the phase transition.[95] Therefore, the soft mode frequency follows the Cochran law:

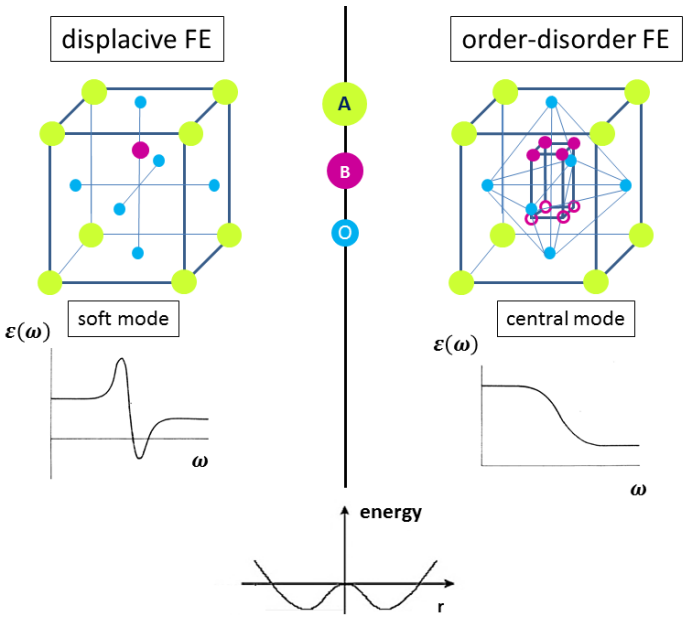

Figure 1.9 The two main classes of FEs: displacive and order-disorder, shown for the perovskite structure. The respective soft and central mode contributions to the permittivity are shown, together with the double-well potential. (image created by the author)

$$\omega_{sm}^2 \propto T - T_C \qquad 1.13$$

In the class of *order-disorder* FEs, the cation B hops among two or more equivalent positions, and the double-well potential remains double-well at both the FE and paraelectric phase. Here, the soft mode mechanism is not responsible for the phase transition, but instead a relaxation mode with frequency lower than that of the lowest polar vibrational mode, and it yields:

$$\omega_R \propto T - T_C \qquad 1.14$$

Both above mentioned types of FE phase transitions are proper FE, i.e. the order parameter is polarization and the phase transition is induced by a soft phonon or relaxation with wavevector from Brillouin-zone center. Nevertheless, pseudoproper and improper FEs also exist, where the order parameter is represented by another quantity, such as strain, the AFM order parameter, the eigenvector of a phonon with wavevector off the Brillouin Zone center, charge, or orbital ordering.[99]

1.3 Lattice and spin excitations in solids

The macroscopic properties of multiferroics can be explained by accessing the atomic- and/or electronic-level behavior of distinct materials. *Lattice vibrations*, or else *phonons*, are related to the *dielectric* properties of solids. In addition, they can give us information about the crystal symmetry, for example identifying polar phases, which are of high interest for the field of multiferroics. *Spin excitations*, or else *magnons*, reflect the *magnetic* properties of the materials, the counter-companion of polarization in the magnetoelectric multiferroics. And finally, the combination of investigation of lattice and spin excitations can reveal the possible coupling between them, thus the novel excitations of *electromagnons*.

As it will be explained in Chapter 2, the access of the microscopic mechanisms is possible via a combination of different spectroscopic techniques, which give us information on the macroscopic response functions. The bridge between the microscopic and the macroscopic behaviors is the theory of physical concepts of lattice and spin excitations. In the current section, the latter concepts will be introduced and related to the macroscopic response functions, such as the complex dielectric function ε^* and the magnetic permeability μ^*.

1.3.1 Lattice vibrations

The main goal in this section is to derive the dispersion relation for phonons in a simplified one-dimensional diatomic crystal, and further on, via a phenomenological approach, to relate the atomic vibrations to the macroscopic dielectric function.

1.3.1.1 One-dimensional diatomic lattice

As a first approximation, we can consider the classical one-dimensional harmonic oscillator, for a diatomic chain of oppositely charged atoms, with masses m and M, and charges e* and –e*, respectively (Figure 1.10). Only nearest neighbor interactions are taken into consideration. Since the current thesis is dedicated to a spectroscopic approach, the long-wavelength limit ($q \rightarrow 0$) holds. In such approximation, all sites with equivalent

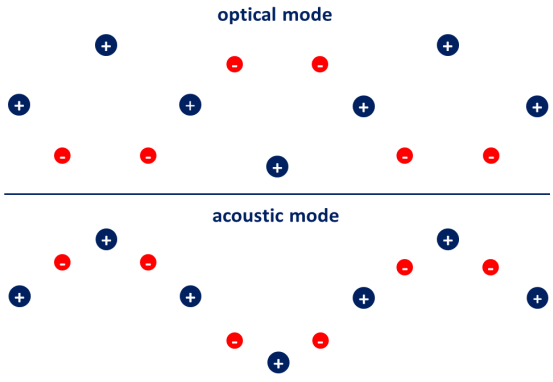

Figure 1.10 The one-dimensional diatomic chain of charged atoms and the two possible vibrational modes: optical and acoustic. (image created by the author)

mass are displaced by the same amount, thus we will attribute displacement u_1 to atoms of mass m and u_2 to atoms with mass M. Due to the dipole interactions, an additional force proportional to the electric field e^*E must be taken into account. Hence, from the equations of motion we get:[100,101]

$$m\frac{d^2u_1}{dt^2} = 2C(u_2 - u_1) + e^*E$$

$$M\frac{d^2u_2}{dt^2} = 2C(u_1 - u_2) - e^*E \qquad 1.15$$

where C is the spring constant. We can consider plane wave solutions for the above system in the form $u_{1,2} \propto e^{i(ka-\omega t)}$, where a is the lattice constant, and arrive to the dispersion relation:

$$\omega^2 = 2C\left(\frac{1}{m}+\frac{1}{M}\right) \pm C\left[\left(\frac{1}{m}+\frac{1}{M}\right)^2 - \frac{4sin^2ka}{mM}\right]^{1/2} \qquad 1.16$$

For the long-wavelength limit ($k \rightarrow 0$), the above dispersion relation reduces to the two following roots:

$$\omega_{OP}^2 = 2C\left(\frac{1}{m}+\frac{1}{M}\right) \qquad 1.17$$

$$\omega_{AC}^2 = \frac{2C}{m+M}k^2a^2 \qquad 1.18$$

corresponding to the optical and acoustic branches respectively. In Figure 1.11, the Brillouin Zone dispersion relation for phonons of the one-dimensional diatomic chain is presented, in comparison with the ones of FM and AFM magnons, which will be discussed later.

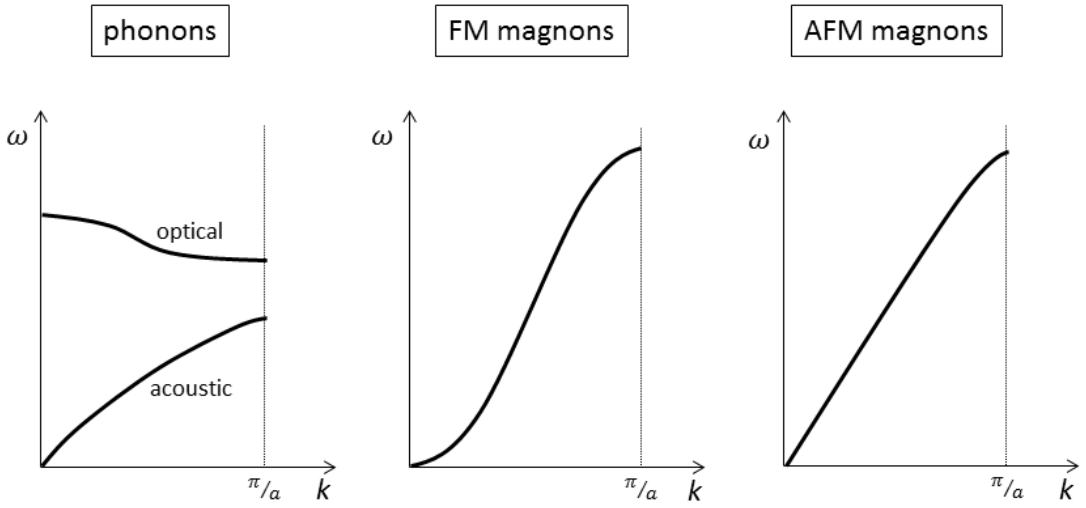

Figure 1.11 Qualitative comparison of the dispersion relations of phonons, FM magnons and AFM magnons, in one-dimensional approach, and within the Brillouin Zone. (image created by the author)

1.3.1.2 Dispersive dielectric function

Polar optical phonons contribute to the dielectric properties of the crystal, and they appear as reflection or absorption bands in the measured experimental spectra. In order to extract this information from the spectra, one needs to relate the microscopic model to the macroscopic electromagnetic theory. In order to achieve that, we return to the equations of motion 1.15, and by plugging in the plane wave solutions, we get the following relations:[101,102]

$$-(\omega^2-\omega_0^2)u_1=\frac{e^*}{m}E$$

$$-(\omega^2-\omega_0^2)u_2=-\frac{e^*}{M}E \qquad 1.19$$

where ω_0^2 is the squared resonant frequency in the absence of Coulomb interactions ($e^*=0$), and it is related to the reduced mass of the ion pair:

$$\omega_0^2=2C\left(\frac{1}{m}+\frac{1}{M}\right) \qquad 1.20$$

At this point we can introduce the polarization, as a summation over all ionic pairs with number N and relative displacement $u=u_1-u_2$:

$$P=\frac{Ne^*u}{\varepsilon_\infty} \qquad 1.21$$

where ε_∞ corresponds to the electronic contribution to the dielectric constant. Equation 1.21 through equations 1.19 becomes:

$$P=\frac{1}{\varepsilon_\infty}\frac{Ne^{*2}}{\omega_0^2-\omega^2}\left(\frac{1}{m}+\frac{1}{M}\right)E \qquad 1.22$$

Let us see now how the transverse and longitudinal optical modes (TO and LO respectively) appear in the description of polar lattice vibrations. The resonant frequency ω_0 mentioned above corresponds to the transverse optical frequency ω_{TO}. The longitudinal optical modes propagate only in the case when the dielectric constant vanishes ($\varepsilon(\omega_{LO})=0$).

But before we continue with the derivation of the expression for the dielectric function, a reminder of the classical Maxwell equations in matter (for zero charge density) is required (in cgs system):[103]

$$\boldsymbol{\nabla} \times \boldsymbol{H} - \frac{1}{c}\frac{\partial \boldsymbol{D}}{\partial t} = \frac{4\pi}{c}\boldsymbol{j}$$

$$\boldsymbol{\nabla} \times \boldsymbol{E} + \frac{1}{c}\frac{\partial \boldsymbol{B}}{\partial t} = 0 \qquad 1.23$$

$$\boldsymbol{\nabla} \cdot \boldsymbol{D} = 0$$

$$\boldsymbol{\nabla} \cdot \boldsymbol{B} = 0$$

where c is the speed of light, $\boldsymbol{H}$ the magnetizing field, $\boldsymbol{D}$ the electric displacement field, $\boldsymbol{j}$ the current density, $\boldsymbol{E}$ the electric field and $\boldsymbol{B}$ the magnetic field. The following constitutive equations are considered:

$$\boldsymbol{D} = \varepsilon \boldsymbol{E} = \boldsymbol{E} + 4\pi \boldsymbol{P}$$

$$\boldsymbol{P} = \chi^{\mathrm{e}} \boldsymbol{E} \qquad 1.24$$

$$\boldsymbol{B} = \mu \boldsymbol{H} = \boldsymbol{H} + 4\pi \boldsymbol{M}$$

$$\boldsymbol{M} = \chi^{\mathrm{m}} \boldsymbol{H}$$

The solutions of the Maxwell equations 1.23 for the propagation of electromagnetic waves in matter, and specifically for the electrical component can be approximated by a plane wave of the form:

$$\boldsymbol{E} = \boldsymbol{E}_0 e^{i(\boldsymbol{kr} - \omega t)} \qquad 1.25$$

where $\boldsymbol{k}$ is the propagation vector and ω the frequency of light. The magnetic component $\boldsymbol{H}$ presents a similar solution, but the detailed derivation will be omitted for the current thesis. For the dispersion relation connecting the polarization P and the electric component E (the vector notation is dropped for simplicity reasons) for the TO mode gives:

$$4\pi\omega^2 P = (c^2 k^2 - \omega^2) E \qquad 1.26$$

For $k = 0$, solving the system of equations 1.22 and 1.26 offers the relation between TO and LO modes:

$$\omega_{LO}^2 = \omega_{TO}^2 + 4\pi \frac{Ne^{*2}}{\varepsilon_\infty}\left(\frac{1}{m} + \frac{1}{M}\right) \qquad 1.27$$

Here we can introduce the dielectric function as:

$$\varepsilon(\omega) = \frac{D(\omega)}{E(\omega)} = 1 + \frac{4\pi P_e(\omega)}{E(\omega)} + \frac{4\pi P_i(\omega)}{E(\omega)} \qquad 1.28$$

where P_e the electronic and P_i the ionic contribution to polarization. Now we can clearly see the definition of the electronic contribution to the dielectric function:

$$\varepsilon_\infty = 1 + \frac{4\pi P_e(\omega)}{E(\omega)} \qquad 1.29$$

Thus, equation 1.28 becomes:

$$\varepsilon(\omega) = \varepsilon_\infty + \frac{4\pi}{\omega_{TO}^2-\omega^2}\frac{Ne^{*2}}{\varepsilon_\infty}\left(\frac{1}{m}+\frac{1}{M}\right) = \varepsilon_\infty + \frac{f}{\omega_{TO}^2-\omega^2} \quad 1.30$$

where f is the so-called oscillator strength of the mode:

$$f = \frac{4\pi Ne^{*2}}{\varepsilon_\infty}\left(\frac{1}{m}+\frac{1}{M}\right) = \Delta\varepsilon \cdot \omega_{TO}^2 \quad 1.31$$

The static dielectric constant is given by:

$$\varepsilon(0) = \varepsilon_\infty + \frac{f}{\omega_{TO}^2} \quad 1.32$$

Equation 1.30 presents a pole for the TO mode, meaning that TO modes can be absorbed. From equations 1.27 and 1.30 we get:

$$\frac{\varepsilon(\omega)}{\varepsilon_\infty} = \frac{\omega_{LO}^2-\omega^2}{\omega_{TO}^2-\omega^2} \quad 1.33$$

The above relation presents the TO-LO splitting for polar modes, and forbids the propagation of waves for frequencies between ω_{TO}^2 and ω_{LO}^2, where $\varepsilon(\omega)$ becomes negative.
If we consider the condition for the propagation of the LO modes $\varepsilon(\omega_{LO}) = 0$, we arrive to the famous Lyddane-Sachs-Teller (LST) relation:[104]

$$\frac{\varepsilon(0)}{\varepsilon_\infty} = \frac{\omega_{LO}^2}{\omega_{TO}^2} \quad 1.34$$

If we introduce a damping contribution of the form $\gamma\frac{du_{1,2}}{dt}$ in the equations of motion 1.15, and sum over all possible *j* independent oscillators, we arrive to the generalized dielectric function:[105]

$$\varepsilon(\omega) = \varepsilon_\infty + \sum_j \frac{f_j}{\omega_{j,TO}^2-\omega^2+i\gamma_{j,TO}\omega} \quad 1.35$$

And the generalized LST relation:

$$\frac{\varepsilon(0)}{\varepsilon_\infty} = \prod_j \frac{\omega_{j,LO}^2}{\omega_{j,TO}^2} \quad 1.36$$

1.3.2 **Spin excitations**

In an analogous way as that of the atomic vibrations in the crystal lattice, spin fluctuations in magnetic structures contribute to the macroscopic magnetic response functions. For the current discussion, it is sufficient to consider the semi-classical approach for the description of spin waves in solids.

The two basic magnetic orders will be discussed: *FM* and *AFM*. The following Heisenberg exchange interaction will be considered, with spin-Hamiltonian:

$$H = -2\sum_{ij} \mathrm{J}_{ij} \left(\mathbf{S}_i \mathbf{S}_j\right) \quad \left\{ \begin{array}{l} J > 0 \;\; ferromagnetic \\ J < 0 \;\; antiferromagnetic \end{array} \right\} \qquad 1.37$$

where $\boldsymbol{S}_\mathrm{i}$, $\boldsymbol{S}_\mathrm{j}$ are the spins of the magnetic ions at sites i and j, and J_ij is the exchange interaction coefficients between the two spins.

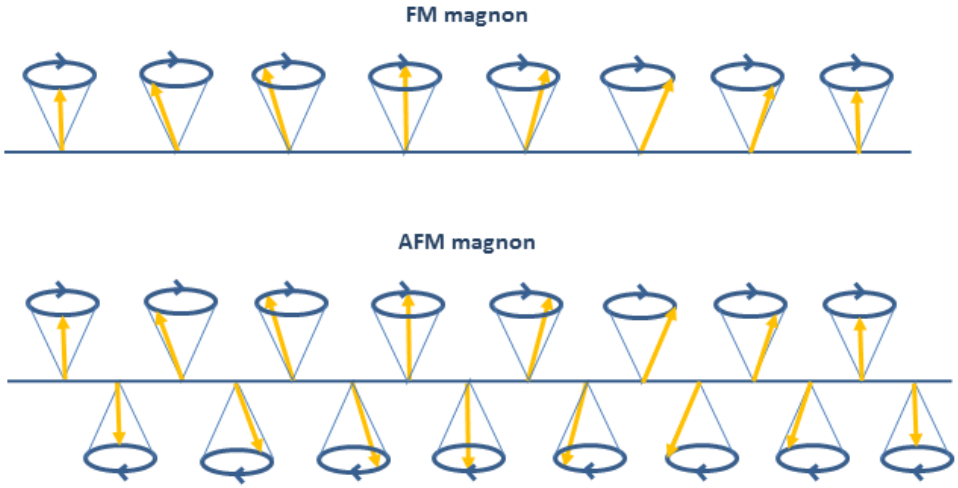

Figure 1.12 Illustration of FM and AFM magnons. The distance between the spins is equal to the lattice constant a, however for demonstration purposes in the AFM magnon it seems shorter than the FM case. (image created by the author)

Ferromagnetic magnons

For a one-dimensional FM alignment of spins $\boldsymbol{S}_j$ (Figure 1.12), within the Heisenberg exchange model of equation 1.37, the following equation of motion holds:[102]

$$\frac{d}{dt}\langle \boldsymbol{S}_j \rangle = -\frac{i}{\hbar}\langle \boldsymbol{S}_j, H \rangle \qquad 1.38$$

which for a ferromagnet from 1.37 and assuming only nearest-neighbour interaction yields:

$$\frac{d}{dt}\langle \boldsymbol{S}_j \rangle = \frac{2J}{\hbar}\langle \boldsymbol{S}_j \times (\boldsymbol{S}_{j+1} + \boldsymbol{S}_{j-1}) \rangle \qquad 1.39$$

Decomposition to the x, y, z components, considering spins along z-axis, and with small deviations to the other coordinates, such as $S^x, S^y \ll S^z,\ S^z = S$, yields:

$$\frac{d}{dt}S_j^x \approx \frac{2JS}{\hbar}(-S_{j-1}^y - S_{j+1}^y + 2S_j^y)$$

$$\frac{d}{dt}S_j^y \approx \frac{2JS}{\hbar}(S_{j-1}^x + S_{j+1}^x - 2S_j^x) \quad 1.40$$

$$\frac{d}{dt}S_j^z \approx 0$$

We assume solutions of the plane wave form: $S_j^x = Ae^{i(jka-\omega t)}$, $S_j^y = Be^{i(jka-\omega t)}$, where a is the lattice constant, with each spin corresponding to neighboring ions, and we arrive to the dispersion relation for the magnons in ferromagnets:

$$\hbar\omega_{FM} = 4JS(1 - coska) \quad 1.41$$

which for the long-wavelength limit reduces to:

$$\hbar\omega_{FM} = 2JSk^2a^2 \quad 1.42$$

From the above, we also get the circular precession expression for the spin amplitudes: $B = -iA$. A qualitative representation of the FM magnon dispersion relation within the Brillouin Zone is shown in Figure 1.11, in comparison with the respective phonon and AFM magnon cases.

Antiferromagnetic magnons

A similar treatment can be followed for the AFM spin waves (Figure 1.12). In order to describe the antiferromagnetically ordered spins, we will consider two sublattices, *A* and *B*, with $S_A^z = S$ and $S_B^z = -S$, respectively. Equations 1.40 become analogously for *A* and *B* sublattices:[102]

$$\frac{d}{dt}S_{A,j}^x \approx \frac{2JS}{\hbar}(-S_{A,j-1}^y - S_{A,j+1}^y - 2S_{A,j}^y)$$

$$\frac{d}{dt}S_{A,j}^y \approx -\frac{2JS}{\hbar}(-S_{A,j-1}^x - S_{A,j+1}^x - 2S_{A,j}^x) \quad 1.43$$

$$\frac{d}{dt}S_{B,j}^x \approx \frac{2JS}{\hbar}(S_{B,j-1}^y + S_{B,j+1}^y + 2S_{B,j}^y)$$

$$\frac{d}{dt}S_{B,j}^y \approx -\frac{2JS}{\hbar}(S_{B,j-1}^x + S_{B,j+1}^x + 2S_{B,j}^x)$$

After some algebra, we arrive to the dispersion relation for the AFM magnons:

$$\hbar^2\omega_{AFM}^2 = 4J^2S^2(1 - cos^2ka) \quad 1.44$$

which for the long-wavelength limit reduces to:

$$\hbar\omega_{AFM} \approx 2JSka \quad 1.45$$

A qualitative representation of the antiferromagnetic magnons dispersion relation within the Brillouin Zone is shown in Figure 1.11, in comparison with the respective phonon and FM

magnons cases. It should be mentioned here that crystal anisotropy opens a gap at the dispersion relation of magnons, enabling detection at long-wavelength.[106] Moreover, in the cases where the magnetic unit cell is larger than the structural unit cell, additional acoustic-like magnon branches appear, which correspond to the THz frequency range at the long-wavelength limit.

Dispersive magnetic permeability

In a similar way as the dispersive dielectric function was derived in section 1.3.1.2, based on Loudon's classical oscillator model,[105] one can arrive to the dispersive expression for the magnetic permeability:[107]

$$\mu(\omega) = 1 - \sum_j \frac{F_j}{\omega^2 - \omega_{j,m}^2 + i\Gamma_{j,m}\omega} \quad 1.46$$

where F_j is the oscillator strength, $\omega_{j,m}$ the resonant frequency of the magnetic oscillators and $\Gamma_{j,m}$ the respective damping.

The combination of the two dispersive expressions of the dielectric function 1.35 and magnetic permeability 1.46 enter in the expression of the complex index of refraction:

$$n^*(\omega) = \sqrt{\varepsilon^*(\omega)\mu^*(\omega)} \quad 1.47$$

The above relation is of high importance for extracting the phonon and magnon parameters from the experimental spectra of infrared and time-domain terahertz spectroscopies, as we will see later in Chapter 2. Lastly, the dispersive magnetoelectric coefficient enters the complex refractive index, as seen from equation 1.11, essential for the case of electromagnon investigation.

1.3.3 **Selection rules**

The use of vibrational selection rules is employed, in order to determine whether a vibrational transition from one eigenstate to another is allowed or not. Infrared (IR) and Raman spectroscopies correspond to different vibrational selection rules.

From equation 1.28, one can see the contribution of the ionic and electronic polarizability in the complex dielectric function. The ionic displacements induce dipole interactions and they are responsible for the absorption or emission of photons with frequencies in the infrared and terahertz regions. The electronic polarizability, or else deformation of the electron cloud of the atom, contributes as well to the total polarization, and it can induce emission (Stokes) or absorption (anti-Stokes) of a phonon, by the inelastic scattering process in the case of Raman spectroscopy.

Therefore, IR and Raman vibrational modes are related to the dipole moment (vector) and polarizability (tensor of 2nd rank) changes, respectively. The symmetry of the crystal is essential for determining the constraints of the light-matter interactions, and therefore the possible transitions. IR-active modes have the same symmetry with the 1st order terms (x, y, z), whereas Raman-active modes with the 2nd order $(x^2, y^2, z^2, xy, yz, xz)$.

The discussed selection rules are extremely important for the detection of soft modes (section 1.2.2), which are simultaneously infrared and Raman active. In a similar way, the same selection rules can be applied for the detection of electromagnons, since those correspond to polar spin-waves.

Chapter 2

Experimental techniques

2 Experimental techniques

One of the easiest, straightforward and cost-effective ways to access the fundamental physical concepts that underlie in the various cases of multiferroic materials is the combination of various spectroscopic techniques.

Three spectroscopic techniques were used throughout the conduction of the experiments of the current thesis, in order to detect the spin and lattice excitations in multiferroics: *Fourier-transform infrared*, *Raman* and *time-domain terahertz spectroscopies*. The range of the electromagnetic spectrum covered by the combination of the above techniques is approximately from 3 to 3000 cm^{-1}, or else 0.09 to 90 THz, or 0.375 to 375 meV, or 3 mm to 1 μm. In Figure 2.1, the region of infrared and terahertz radiation is shown within the entire range of the electromagnetic spectrum. The principles of each technique, along with the fitting model considerations used to treat the spectra of the materials in question, will be presented in the current chapter.

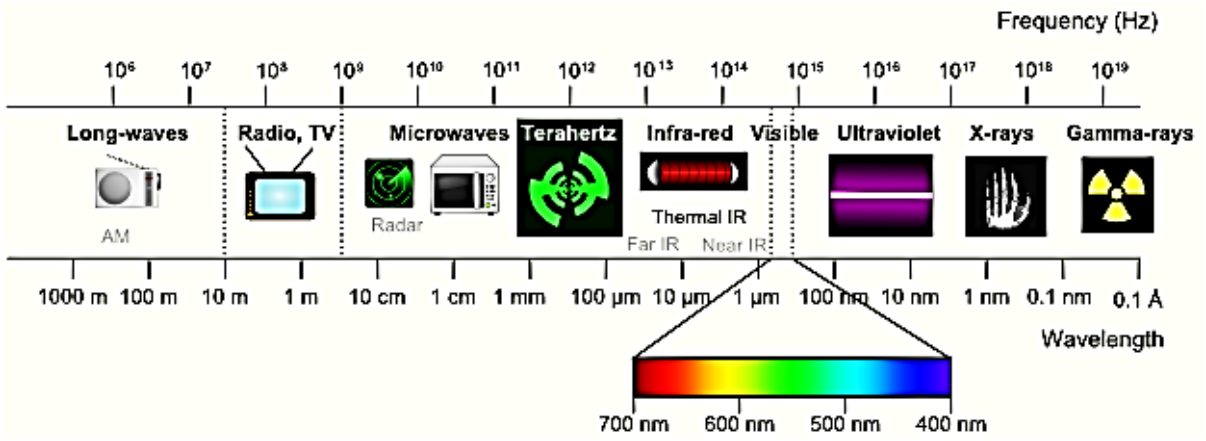

Figure 2.1 Scheme of the electromagnetic spectrum range, from long-wave radio to gamma-rays. Infrared and terahertz ranges lie in the millimeter and submillimeter wavelength region, bridging electronic and optical spectroscopies.[108]

2.1 Fourier-transform infrared spectroscopy

Although the visible range (~400 – 700 nm) was already explored by Newton in the 17th century, with his famous letter on the refraction of light through a prism,[109] IR radiation took almost another 100 years to be observed. In 1800, Herschel measured the heat effect of dispersed light on a mercury thermometer, beyond the red wavelengths of the visible range, noted as "radiant heat".[110] At the end of 19th century, Rubens and his collaborators with a series of experiments managed to extend the range of IR radiation, reaching the scale of ~10 μm.[111–114]

Nichols' detection of strong reflection bands in crystalline quartz at ~9 μm, reaching almost 100% of reflectivity, revolutionized the far-IR spectrometry.[113] The detected radiation was later called by Rubens "reststrahlen" (translation from German: residual rays), and it corresponds to the lattice vibrations in the crystal lattice.[115] Among other contributions of Rubens' group in IR spectroscopy was the use of the mercury arc lamp within quartz as an IR source,[116] which is still widely used, and the almost 100% reflective surfaces of pure metals,[117] a property which is used as sampling reference.

Despite the outstanding efforts of long-wavelength spectroscopy in late 19th century, the lack of suitable detectors delayed advances almost by half a century. However, a few prototype IR spectrometers were built during the 1930s, reaching wavelengths of ~200 μm.[118] Among the innumerous and ironically fortunate inventions achieved during World War II was the thermocouple detector, which was employed in an IR spectrophotometer by Wright & Hersher in 1947.[119,120] But still, another 20 years had to pass for the revolutionary era of IR spectroscopy to come, since most systems were based on prism or grating monochromators. The interferometer technique, introduced by Michelson in 1891,[121] and accompanied by the Fourier-transform conversion of an interferogram to a spectrum, pointed out by Rayleigh in the same year,[122] was widely known for many years. But it was only in 1949 that Fellgett calculated for the first time a Fourier-transform IR (FTIR) spectrum (later known as multiplex or Fellgett advantage),[115] collected by star observation. In 1950s Jacquinot noted the importance of the use of large apertures in interferometers (known as Jacquinot or throughput advantage)[115,123,124] and the wide use of FTIR spectrometers was initiated. Finally, the contribution of the fast FT algorithm by Cooley & Tukey,[125] and the advances in computer technology in the years to come, commercialized FTIR spectrometers, resulting in a widespread use in various fields.

2.1.1 **Basic principles of FTIR spectroscopy**

Lattice vibrations in solids mostly lie in the IR range of the electromagnetic spectrum. One of the most convenient methods to measure the IR phonons is the use of Fourier-transform interferometer, which simultaneously detects a broadband signal and transforms it to a frequency-dependent spectrum.

Such treatment is possible by the use of Michelson interferometer, which is based on the principle of creating interference patterns by changing the optical path of the beam. Initially, the beam is separated into two parts by a beamsplitter, and one of them is reflected by a moving mirror. The intensity of the signal of the interference of the two beams is related to the optical

path difference, and it is defined as *interferogram*. After the detection, the interferograms undergo Fourier-transformation, and the spectrum is produced in the particular spectral range of choice.

By the use of a combination of light sources, beamsplitters and detectors, one can chose to study the far-IR (FIR), mid-IR (MIR) or near-IR (NIR) range. Most of phonons in the materials studied for the current thesis appear in the FIR range, however the MIR range is essential for the information on the high-frequency electronic contributions.

2.1.2 **Fitting models**

The spectra obtained from the various spectroscopic techniques contain the physical properties of the materials under investigation. A spectrum is most often presented as the frequency dependence of reflection, transmission or absorption of light that is directed to the sample. The latter quantities are in turn related to the response functions of the material, such as the complex dielectric function ε^* and the magnetic permeability μ^*.

In order to arrive to the desired expressions, let us go back to introducing the plane wave solutions to the Maxwell equations 1.23 and derive the following dispersion relation:

$$k^* = \frac{\omega}{c}\sqrt{\varepsilon^*\mu^*} \quad 2.1$$

where $k^*, \varepsilon^*, \mu^*$ stand for the complex functions of wavevector, dielectric function and magnetic permeability, yielding:

$$\varepsilon^* = \varepsilon' - i\varepsilon'' \quad 2.2$$

$$\mu^* = \mu' - i\mu'' \quad 2.3$$

where the imaginary parts correspond to losses, thus the convention of the negative sign. The complex refractive index is:

$$n^* = \sqrt{\varepsilon^*\mu^*} = n - ik \quad 2.4$$

From equations 2.2 and 2.4, one arrives to the following relation between the dielectric function and the refractive index:

$$\varepsilon^* = (n - ik)^2 \Rightarrow \begin{Bmatrix} \varepsilon' = n^2 - k^2 \\ \varepsilon'' = 2nk \end{Bmatrix} \quad 2.5$$

If we consider the near normal incidence geometry and neglect multiple reflections from the backside of the sample surface for the bulk case, then the incident wave E_i is partly transmitted E_t and partly reflected E_r, and the continuity equation at the surface yields:

$$E_i = E_t + E_r \quad (2.6)$$

Introducing the above to the Maxwell's equations 1.23, we end up with the incident and reflected components:

$$E_i = \frac{1}{2}E_0(n^* + 1)$$

$$E_r = \frac{1}{2}E_0(n^* - 1) \quad (2.7)$$

Now we can define the reflectivity as the ratio of the amplitudes between the incident and the reflected waves:

$$R = \left|\frac{n^*-1}{n^*+1}\right|^2 = \frac{(n-1)^2+k^2}{(n+1)^2+k^2} \quad (2.8)$$

or else:

$$R = \left|\frac{\sqrt{\varepsilon^*}-\sqrt{\mu^*}}{\sqrt{\varepsilon^*}+\sqrt{\mu^*}}\right|^2 \quad (2.9)$$

Finally, we have an expression that relates the observed quantity of the reflected radiation derived from the experimental spectra to the physical properties of the material, either described by the complex index of refraction or the complex dielectric function and magnetic permeability. Based on the idea above, that the light can be reflected (R), transmitted (T) or absorbed (A), the following equation holds:

$$1 = R + T + A \quad (2.10)$$

The three main models that were used for the evaluation of the spectra of the current work are presented below.

2.1.2.1 Classical damped harmonic oscillator model

In the case of symmetrical and narrow IR reflection bands, or else when the TO-LO splitting is small, a sum of damped harmonic oscillators can be considered:[105]

$$\varepsilon(\omega) = \varepsilon_\infty + \sum_i \frac{f_i}{\omega_{i,TO}^2 - \omega^2 + i\gamma_{i,TO}\omega}, f_i = \Delta\varepsilon_i \cdot \omega_{i,TO}^2 \quad (2.11)$$

where $\omega_{i,TO}$ of i-th transverse optic (TO) phonons, and $\gamma_{i,TO}$ are the corresponding damping constants.

2.1.2.2 4-parameter generalized oscillator model

On the other hand, when the bands are too asymmetrical and broad, or else the TO-LO splitting too high, one can retreat to the generalized LST relation, where a factorized expression of zeros and poles are used:[126]

$$\varepsilon(\omega) = \varepsilon_\infty + \prod_i \frac{\omega_{i,LO}^2 - \omega^2 + i\gamma_{i,LO}\omega}{\omega_{i,TO}^2 - \omega^2 + i\gamma_{i,TO}\omega} \qquad 2.12$$

where $\omega_{i,TO}$ and $\omega_{i,LO}$ are the frequencies of i-th transverse optic (TO) and longitudinal optic (LO) phonons, and $\gamma_{i,TO}$ and $\gamma_{i,LO}$ are the corresponding damping constants.

2.1.3 **Current setup**

The near-normal incidence IR reflectivity spectra are measured by a Fourier-transform IR spectrometer Bruker IFS 113v in the frequency range of 20—3000 cm^{-1} (0.6 – 90 THz) at room temperature (RT) (Figure 2.2). For the low-temperature measurements, the spectral range is reduced by the transparence of cryostat windows to 20—650 cm^{-1}. A pyroelectric deuterated triglycine sulfate detector is used for the room-temperature measurements, whereas a He-cooled (operating temperature 1.6 K) Si bolometer is used for the low-temperature measurements down to approximately 7 K. A commercial high-temperature cell (SPECAC P/N 5850) is used for the high-temperature experiments. The thermal radiation from the hot sample entering the interferometer is taken into account in our spectra evaluation.

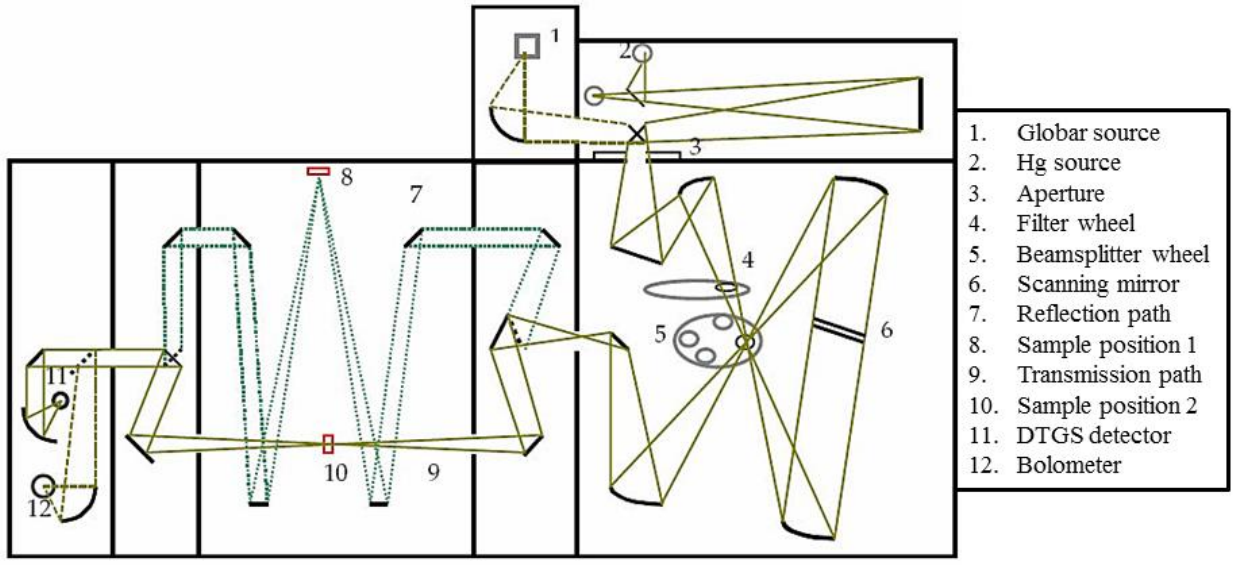

Figure 2.2 Schematic representation of the FTIR experimental setup used in the current thesis.

2.2 **Raman spectroscopy**

Raman effect, or else inelastic scattering of electromagnetic radiation by matter, was theoretically predicted for the first time in 1923 by Smekal.[127] The same year, Compton detected the X-ray inelastic scattering by particles,[128] and in 1928, Raman and Krishnan proved experimentally the "optical analog of the Compton effect", now known as "Raman" effect.[129] The same year, similar observation was done by Landsberg and Mandelstam,[130] although not that widely known.

As for all spectroscopies, the technological advances of the 1960s upgraded the experimental systems, and launched the successful fields of Raman, IR and THz spectroscopies - the main interest of the current thesis. For Raman spectroscopy though, the invention of laser by Maiman in 1960[131] was of great importance, since the use of monochromatic radiation was necessary. Another significant invention that contributed to the advances of Raman spectroscopy was the invention of charged coupled semiconductor devices (CCD) by Boyle and Smith,[132] which up to now is the most common detector.

2.2.1 **Basic principles of Raman Spectroscopy**

Monochromatic radiation is sent to the material under investigation. As mentioned earlier, the most common sources are lasers. Subsequently, two processes occur: *elastic* (Rayleigh) and *inelastic scattering*.[133,134] In the first case, the incident and the scattered photon have the same frequency (the laser beam frequency). In the latter, the incident photon loses part of its energy due to the interaction with the crystal lattice, which results in a shift between the incident and scattered frequency.

The frequency shift experienced by the photons is called *Raman shift*, and it corresponds to the frequency of collective excitations (quasi-particles) of the lattice (phonons), spin structure (magnons, electromagnons), electron density (plasmons), to name a few. In the current thesis, we will concentrate in the spin and lattice excitations.

The Rayleigh scattering results in an intense line in the Raman spectra, at zero Raman shift frequency, whereas the inelastic scattering produces weaker peaks with non-zero Raman shift frequency. There are two inelastic scattering processes: creation (Stokes) and annihilation (anti-Stokes) of a phonon, resulting in emission of a higher and lower energy photon (compared to the incident one), respectively (Figure 2.3). Therefore, Stokes lines are designated with positive values of the Raman shift frequencies, whereas anti-Stokes with negative.

As discussed in paragraph 1.3.3, the crystal symmetry is important for the selection rules of the vibrational modes, thus the geometrical configuration of the experimental setup (orientation of polarizer and analyzer) can yield different vibrational spectra. Thorough investigation of all possible polarization configurations provides the whole set of Raman-active modes for a particular crystal symmetry. Due to the difference in selection rules between Raman and IR spectroscopies, a combination of the two techniques is preferable for better understanding of the underlying physical behavior of materials.

In Figure 2.3, the different absorption/emission processes for infrared-terahertz and Raman spectroscopies are presented, along with the energy and momentum conservation laws, where $\omega, \boldsymbol{k}$ and $\Omega, \mathbf{q}$ are the photon and phonon frequencies and wavevectors, respectively. The $\pm$ symbol corresponds to the Stokes and anti-Stokes scattering processes, where annihilation and creation of a phonon, respectively, is realized by photon scattering.

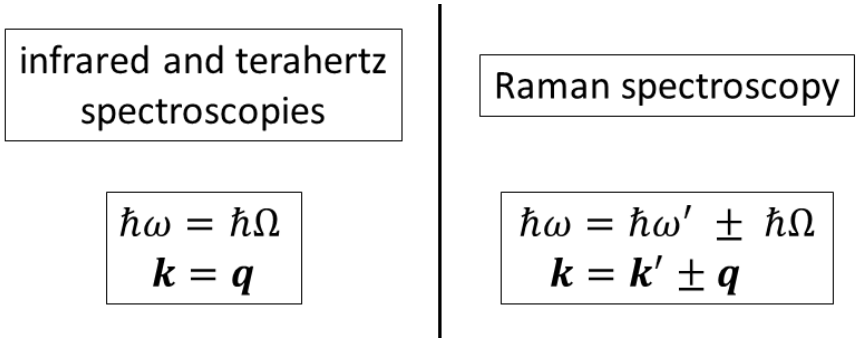

Figure 2.3 Absorption/emission (annihilation/creation) processes of photon (phonon) in infrared-terahertz/Raman spectroscopies, respectively.

2.2.2 **Current setup**

The setup shown in Figure 2.4 was used in the current thesis for the Raman studies of single crystals. A Renishaw RM 1000 Micro-Raman spectrometer with Bragg filters is used, equipped with an Oxford Instruments Microstat continuous-flow optical He cryostat. The experiments are performed in the backscattering geometry in the 5–1800 cm^{-1} range. An Ar^{+}-ion laser operating at 514.5 nm is employed. The spectra are carefully fitted with the sum of independent damped harmonic oscillators multiplied by the corresponding Stokes temperature factor.[135]

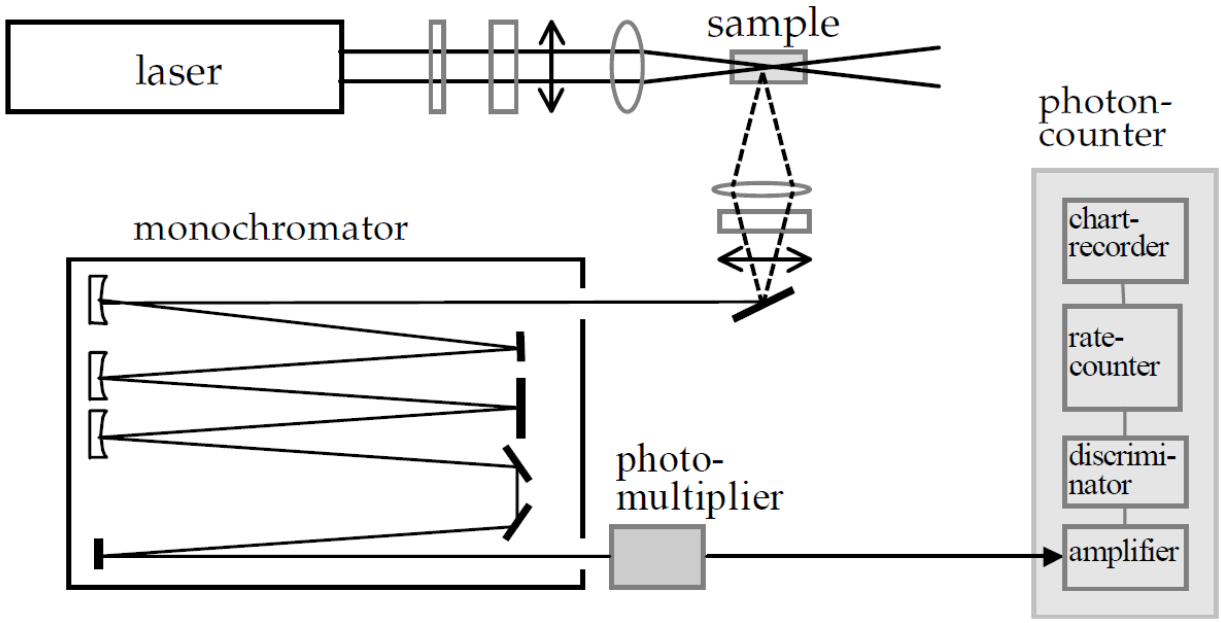

Figure 2.4 Schematic representation of the current Raman experimental setup.

2.3 **Time-domain terahertz spectroscopy**

Terahertz (THz) spectroscopy can be viewed as the "starlet" of spectroscopies. This quite new field, being approximately 30 years-old, has attracted vast scientific attention, due to the fundamental physical concepts related to the THz spectral range, and thereby, the innumerous applications in optoelectronics, medicine, biology, biochemistry, security technologies and art conservation. But let us see why it took so long for the scientific community to explore the so-called "THz gap".

As mentioned in section 2.1, quite a few efforts were made at the end of 19th century to approach the far-infrared range of the electromagnetic spectrum. Rubens & Snow published in 1893 experimental results on rock-salt (NaCl), sylvite (KCl) and fluorite (CaF_2) prisms, reaching wavelengths of approximately $8\mu m$ ($\sim 37\ THz$), by, as they called it, "production of prismatic heat-spectra".[111] A series of publications by Rubens and his collaborators for the years to come[112–114] triggered Max Planck to close the gap between the short- and long-wavelengths, and arrive to the final expression of the blackbody radiation law, historically significant for the foundation of quantum mechanics.[136,137] Until 1930s, the exploration of the long-wavelength spectrum was mainly done from high-to-low frequencies, thus the optical field of spectroscopies. Thereafter, great contribution was achieved by the field of microwave spectroscopy, thus the electronic counterpart, aiming at narrowing the THz gap from low-to-high frequencies. As an

example, Cleeton & Williams measured in 1934 absorption of wavelengths in the order of cm, by the use of magnetron.[138]

However, the elegance of physics hidden in the THz spectral region and the lack of technological means did not allow its exploration almost until the 1970s. The first time-domain THz spectrometer was used in 1968,[139] in the microwave region, and the first results were obtained by Yang *et al*. in 1971.[140]

2.3.1 **Principles of the time-domain THz method**

The THz time-domain spectroscopy (THz-TDS) makes use of optoelectronically generated electromagnetic transients (high-amplitude and short-duration wave). The THz transients are produced by femptosecond (fs) laser pulses. A typical THz-TDS setup is the one presented in Figure 2.5, where the train of laser pulses is sent to a beamsplitter to follow two paths: one moving mirror serving as delay line, and the other one, going through the THz emitter, and subsequently to the sample. Finally, the two beams interfere at the detector, and thereby the THz signal is treated by the lock-in amplifier. After collection of the THz pulses by the computer, the spectra are calculated by Fourier-transform, passing to the frequency-domain. The spectral resolution in THz-TDS is defined by the inverse of the optical delay time.

One of the most important features of THz-TDS is the access to the phase of the propagated electromagnetic wave, which relieves from the need of the use of Kramers-Kronig relations for the evaluation of the complex dielectric function. In addition, the combination of the elevated brightness of THz transients (compared to the thermal sources used in IR spectroscopy), with the highly sensitive gated detection of about ~ps time resolution, and the high signal-to-noise ratio, establishes THz-TDS as preferred technique in particular spectral ranges (however depending on the sample THz transparency).[141]

2.3.2 **Current setup**

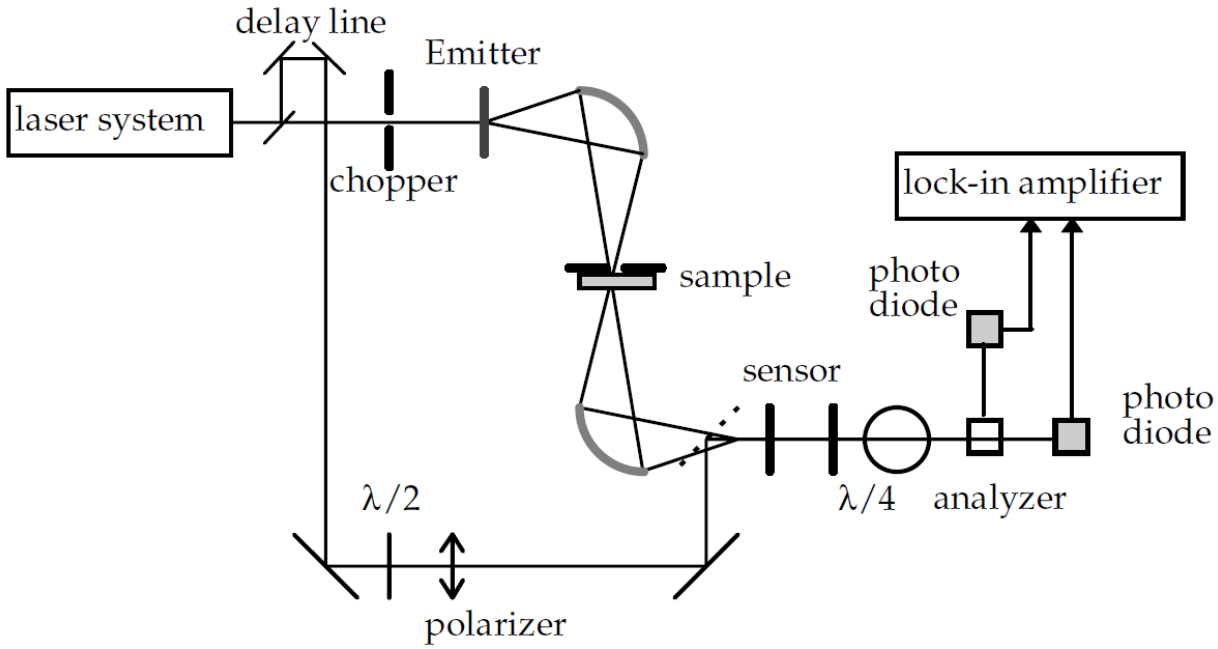

Figure 2.5 Experimental setup of the time-domain terahertz spectrometer used in the current thesis.

The THz-TDS measurements for the current thesis were performed in the transmission geometry with a custom-made time-domain THz spectrometer, from 3 to 70 cm^{-1} (0.09 – 2.0 THz). A femtosecond Ti:sapphire laser oscillator (Coherent, Mira) produces a train of femtosecond pulses, which generate linearly polarized broadband THz pulses radiated by a photoconducting switch TeraSED (Giga-Optics). A gated detection scheme based on electrooptic sampling with a 1 mm thick [110] ZnTe crystal as a sensor allows us to measure the time profile of the electric field of the transmitted THz pulse (Figure 2.5). An Oxford Instruments Optistat optical cryostat with mylar windows is used for the low-temperature THz measurements. With the use of a superconducting magnet, THz experiments in an external magnetic field ($H_{ext} \leq 7$ T) are also possible. An Oxford Instruments Spectromag cryostat in the Voigt configuration is then used for these measurements, where the electric component of the THz radiation $\boldsymbol{E}_{THz}$ is set parallel and perpendicular to $\boldsymbol{H}_{ext}$.

Chapter 3

Results

Chapter 3 Results

3 Results

The scientific significance of dynamical magnetoelectric coupling, combined with the eminent implication of its technological applications, prompted the investigation of spin and lattice excitations of a series of materials.

In the current chapter, the experimental findings of already widely known multiferroic materials, as well as entirely novel compounds, will be presented. Hereby, the structure of the coming chapter will be briefed.

The celebrated room temperature multiferroic $BiFeO_3$ launches the exploration of magnetoelectric excitations in the current work. Even though $BiFeO_3$ possesses a complex magnetic behaviour, and multiferroic properties originating in diverse mechanisms simultaneously, it is considered a model multiferroic, therefore it is chosen to initiate this chapter. The spin and lattice excitations of $BiFeO_6$ ceramics and thin film are discussed, as reported in Ref. 142.

In section 3.2, the novel double perovskite Pb_2MnTeO_6 is described for the first time, by a series of structural, magnetic, dielectric and spectroscopic characterization. Its crystal and magnetic structure classify it in the rare family of antipolar antiferromagnets. The observations on Pb_2MnTeO_6 were published in Ref. 143.

The last subchapter of the materials under investigation is dedicated to the family of Ni-based tellurides, of the corundum-related structure $Ni_{3-x}B_xTeO_6$ (B=Mn, Co). The spin-induced colossal magnetoelectric effect in Ni_3TeO_6 stimulated the probe of magnetoelectric excitations, revealing electromagnons. These results were published in Ref. 144. Exploiting the existence of dynamical magnetoelectric coupling in Ni_3TeO_6, novel compounds of Ni-substitution by Mn and Co were synthesized and studied for the first time. The enhanced magnetoelectric properties of the new compounds will be demonstrated in detail.

3.1 Spin and lattice excitations of a $BiFeO_3$ thin film and ceramics

A comprehensive study of polar and magnetic excitations in $BiFeO_3$ ceramics and a thin film epitaxially grown on an orthorhombic (110) $TbScO_3$ substrate will be presented in the current section, as published in Ref. 142.

IR reflectivity spectroscopy was performed at temperatures from 5 to 900 K for the ceramics and below room temperature for the thin film. All 13 polar phonons allowed by the factor-group analysis were observed in the ceramic samples. The thin-film spectra revealed 12 phonon modes only and an additional weak excitation, probably of spin origin. On heating towards the FE phase transition near 1100 K, some phonons soften, leading to an increase in the static permittivity.

In the ceramics, terahertz transmission spectra show five low-energy magnetic excitations including two which were not previously known to be IR active; at 5 K, their frequencies are 53 and 56 cm^{-1}. Heating induces softening of all magnetic modes. At a temperature of 5 K, applying an external magnetic field of up to 7 T irreversibly alters the intensities of some of these modes. The frequencies of the observed spin excitations provide support for the recently developed complex model of magnetic interactions in $BiFeO_3$.[145] The simultaneous IR and Raman activity of the spin excitations is consistent with their assignment to electromagnons.

A comparison of the spin-wave frequency temperature dependence in $BiFeO_3$, from the current and previous studies, is presented below as a preview to the coming section.

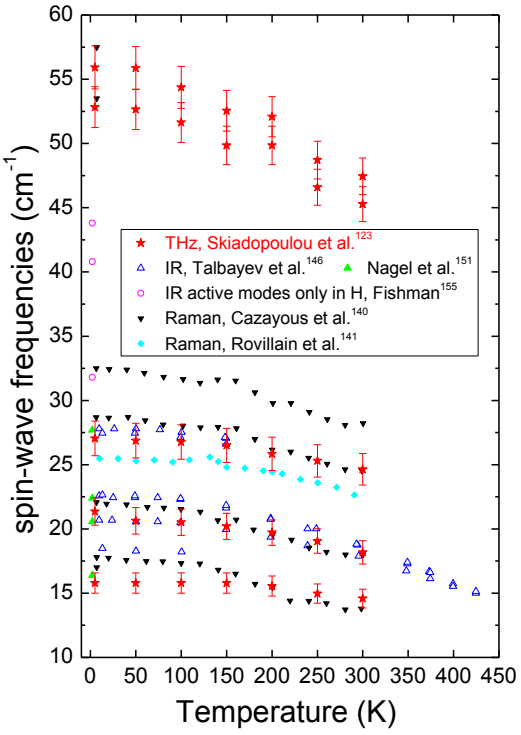

3.1.1 **Introduction**

Among novel materials, an intense effort is concentrated on the study of multiferroics.[1,70] A wide range of applications, such as information storage, sensing, actuation, and spintronics, await pioneering materials and strategies that would produce robust magnetoelectric coupling at room temperature (RT).[2,146] The ability to manipulate magnetization in a magnetoelectric multiferroic by electric fields can be extremely promising for such applications, due to the simplicity and cost efficiency of applying an electric field. As one of the few single-phase RT magnetoelectric multiferroics, bismuth ferrite $BiFeO_3$ is at the center of attention, as it presents a FE phase transition at approximately 1100 K and an antiferromagnetic (AFM) one at 643 K.[147]

The knowledge of lattice and spin excitations in $BiFeO_3$ is essential for understanding the underlying mechanisms that induce its multiferroic behavior. A series of Raman and IR spectroscopy studies have presented controversial results concerning the assignment of the magnon and phonon modes, as well as of the highly acclaimed electromagnons (i.e., electrically active magnons). Probing IR-active low-energy excitations is hindered by a lack of sufficiently large single crystals. Raman-active phonons of the rhombohedral *R*3*c* $BiFeO_3$ structure have been reported for single crystals,[148–150] polycrystalline ceramics,[151–153] and thin films,[154,155] however, there is a significant discrepancy between the claimed phonon frequencies and symmetry representations. A possible explanation for such inconsistences between the various experimental results is the presence of oblique phonon modes, which show a continuous variation of frequency along the phonon propagation vector with respect to the crystallographic axes of the probed specimen.[153] Up to now, the phonon IR spectroscopy studies have been focused on ceramics[156–158] and single crystals,[159,160] whereas, to our knowledge, no report of a thin-film IR investigation exists.

When it comes to magnon and electromagnon studies, Raman spectroscopy holds the record for the number of excitations observed, yielding up to 16 magnetic modes corresponding to the cycloidal spin structure (eight Φ_n cyclon and eight Ψ_n extra-cyclon modes) for single crystals,[161–164] but only one for polycrystalline thin films.[165,166] Furthermore, the influence of strain on the number of spin excitations and their frequencies were reported for epitaxial thin films grown on a series of substrates.[167] Time-domain terahertz (THz) spectroscopy,[168] inelastic neutron scattering measurements,[169–172] and absorbance spectroscopy in the THz range[173] (Figure 3.1(b)) have revealed modes similar to the Raman-active ones predicted by theoretical calculations.[145,173–176]

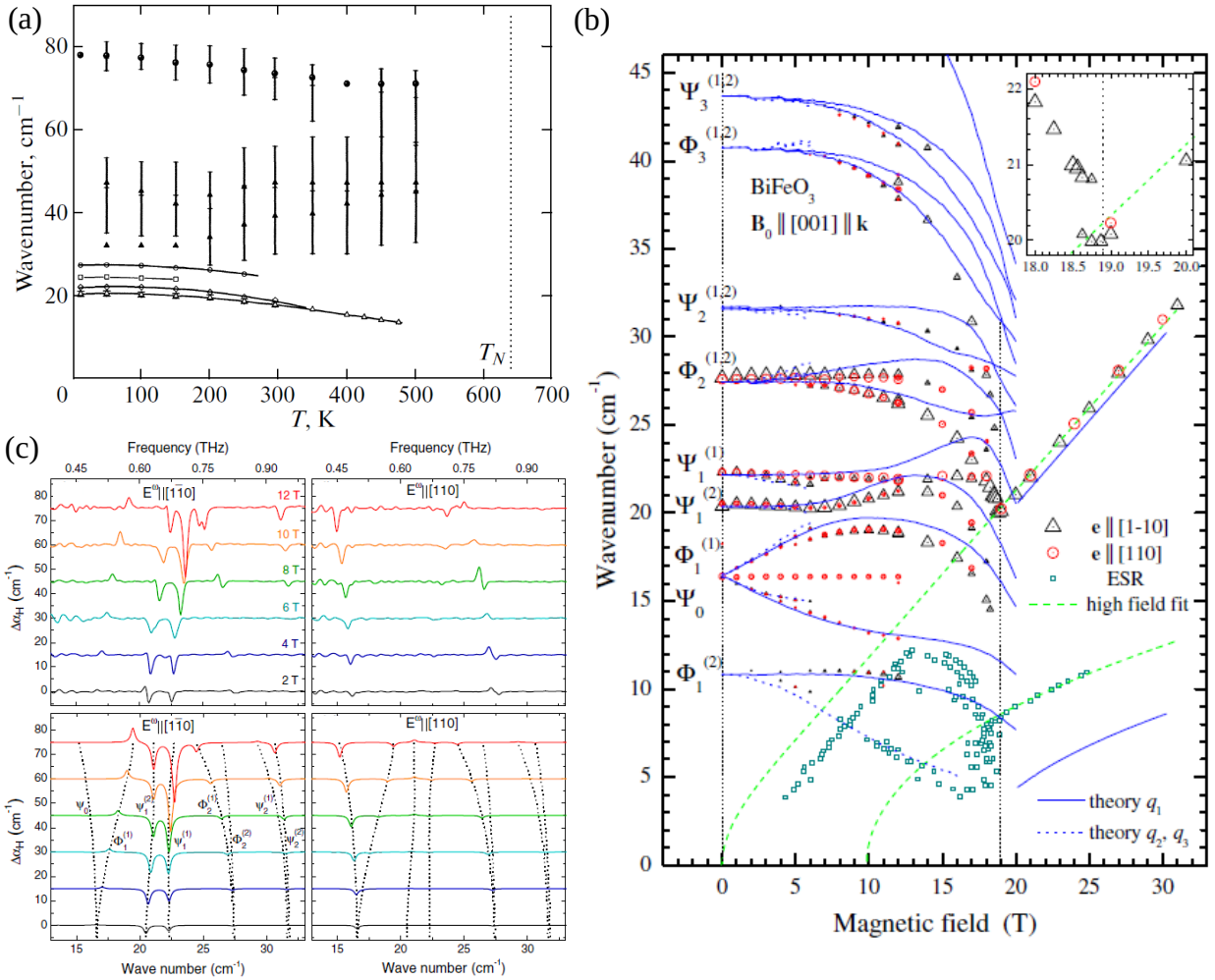

Figure 3.1 (a) Temperature dependence of magnon frequencies (open symbols) in $BiFeO_3$ ceramics below 40 cm^{-1}, as obtained by IR transmission spectra by Komandin *et al.*.[157] (b) Magnetic field dependence of spin wave modes in the terahertz absorption spectrum of $BiFeO_3$ at 4 K, reported by Nagel *et al.*.[173] The unwinding of the cycloidal spin structure occurring at 18:8 T is evident. Blue solid lines are calculated modes of cycloid $\boldsymbol{q_1}$, and dotted blue lines of $\boldsymbol{q_2}$ and $\boldsymbol{q_3}$. (c) Magnetic-field dependence of the non-reciprocal directional dichroism spectra of $BiFeO_3$ single crystal, measured at 2.5 K with the two orthogonal polarizations $E_{ext} \parallel [1\bar{1}0]$ (up left) and $E_{ext} \parallel [110]$ (up right) respectively, published by Kezsmarki *et al.*.[177] The calculated spectra are displayed right below respective polarizations, together with the assignment of each mode.

The best agreement between the experimental and theoretical spin-excitation frequencies (including their splitting in an external magnetic field) was obtained for a microscopic model that takes into account the nearest and next-nearest neighbor exchange interactions, two Dzyaloshinskii-Moriya interactions, and an easy-axis anisotropy.[145,173] The same model successfully described the low-energy inelastic neutron scattering spectra.[172] In contrast, Komandin *et al.*[157] showed IR transmission spectra with an excitation at approximately 47 cm^{-1} which had not been previously reported by experimental or theoretical studies (Figure 3.1(a)). The intensive discussion in the literature concerning the nature of the spin excitations raises the question: which excitations are pure magnons (i.e., contribute only to the magnetic permeability

μ^*) and which are electromagnons (i.e., influence at least partially the permittivity ε^*)? It is worth noting that according to a recent symmetry analysis,[81] $BiFeO_3$ allows directional dichroism and therefore spin waves can be simultaneously excited by the electric and magnetic components of electromagnetic radiation, which was experimentally observed by Kezsmarki *et al.*[177] (Figure 3.1(c)). For more details on $BiFeO_3$ spin dynamics, see the review of Park *et al.*.[178]

In the current work we report spin and lattice excitations in $BiFeO_3$ ceramics, as measured by the combination of IR reflectivity and time-domain THz transmission spectroscopy, in a temperature range from 10 to 900 K. All 13 IR-active phonon modes are observed, exhibiting softening on heating. Five low-frequency spin modes are detected from 5 K up to RT, the highest two appearing at 53 and 56 cm^{-1}. This corresponds to the frequency range where such excitations were theoretically predicted,[145,173,174] but not experimentally confirmed up to now. At 5 K, the low-energy spin dynamics in the THz range were also studied in a varying magnetic field of up to 7 T. Softening of the (electro)magnon frequencies upon increasing the magnetic field was observed. Additionally, a $BiFeO_3$ epitaxial thin film grown on an orthorhombic (110) $TbScO_3$ single crystal substrate was studied via IR reflectance spectroscopy.

3.1.2 **Experimental details**

$BiFeO_3$ ceramics were prepared by the solid-state route. A stoichiometric mixture of Fe_2O_3 and Bi_2O_3 powder oxides with a purity of 99.99% was ground and uniaxially cold-pressed under 20–30 MPa pressure into 8 mm diameter pellets. The pellets were then covered by sacrificial $BiFeO_3$ powder to avoid bismuth oxide loss from the pellet, and sintered in a tube furnace at 825° C for 8 h in air. To avoid any secondary phase formation, the samples were quenched to RT. Polished disks with a diameter of 4 mm and thicknesses of approximately 600 and 338 μm were used for the IR reflectivity and THz transmission measurements, respectively.

An epitaxial $BiFeO_3$ thin film with a thickness of 300 nm was grown by reactive molecular-beam epitaxy on a (110) single crystal substrate. The growth parameters were the same as for the samples reported in Ref. 179. A commercial high-temperature cell (SPECAC P/N 5850) was used for the high-temperature experiments. The thermal radiation from the hot sample entering the interferometer was taken into account in our spectra evaluation.

The experimental details of IR reflectivity and time-domain THz spectroscopies used for the study of spin and lattice excitations were according to Chapter 2.

3.1.3 **Results and discussion**

3.1.3.1 Phonons in the $BiFeO_3$ ceramics

The temperature dependence of the experimental IR reflectivity spectra of the $BiFeO_3$ ceramics is shown in Figure 3.2(a). The reflectivity band intensities are higher than those in the previously published spectra of ceramics[156–158] and single crystal,[160] but comparable to the single-crystal spectra published by Lobo *et al.*.[159] This confirms the very high quality and density of our ceramic samples, which is essential for an accurate determination of phonon and magnon parameters.

The IR reflectivity and THz transmission spectra were fit simultaneously using equation 2.12, the resulting phonon parameters are listed in Table 3.1. The real and imaginary parts of the complex dielectric spectra calculated from the fits are shown in Figure 3.2(b) and (c). As predicted by the factor group analysis for the rhombohedral *R*3*c* structure of $BiFeO_3$,[156] all 13 IR-active phonons ($4A_1 + 9E$ symmetries) are clearly seen from 10 K up to RT. In Table I the symmetries of all modes are assigned based on Raman spectra,[153] first-principles calculations,[180] and IR spectra of single crystals.[159] The damping of the modes strongly increases on heating; therefore, above 300 K, the IR reflection bands broaden and mutually overlap. Note the remarkable softening of the modes below 150 cm^{-1} upon heating (see Figure 3.2). Consequently, the static permittivity ε(0) determined by the sum of phonon contributions as $\varepsilon(0) = \varepsilon_\infty + \sum \Delta\varepsilon_j$ increases on heating in agreement with the Lyddane-Sachs-Teller relation[181] (see Figure 3.3). A qualitatively similar temperature dependence was published in previous studies of $BiFeO_3$ ceramics,[156,157] but the absolute value of permittivity was lower, probably due to a lower density/quality of the earlier studied ceramics.

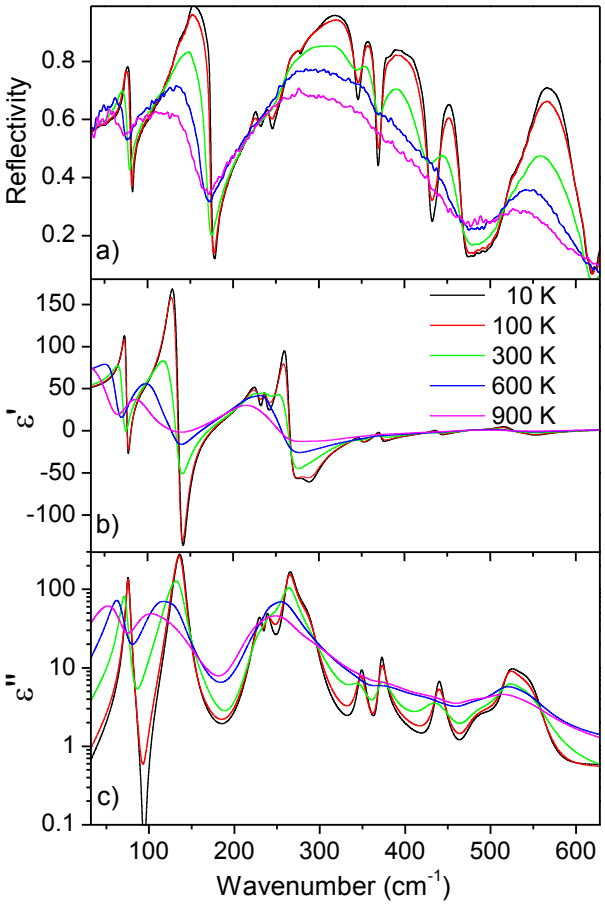

Figure 3.2 (a) IR reflectivity spectra of $BiFeO_3$ ceramics as selected temperatures. (b) Real and (c) imaginary part of permittivity, as obtained from the fits.

Table 3.1 A comparison of the parameters of the IR-active modes in the $BiFeO_3$ ceramics (at 10 and 900 K) and the thin film (at 10 K), obtained from IR spectra fitting. The symmetry assignment of each mode is also given.

	Ceramics								Thin Film					
	10 K				900 K				10 K $E_{ext} \parallel [1\bar{1}0]$			10 K $E_{ext} \parallel [001]$		
Symmetry	ω_{TO}	γ_{TO}	ω_{LO}	γ_{LO}	ω_{TO}	γ_{TO}	ω_{LO}	γ_{LO}	ω_{TO}	γ_{TO}	$\Delta\varepsilon$	ω_{TO}	γ_{TO}	$\Delta\varepsilon$
E	75.8	4.6	81.5	2.8	64.3	40.9	70.5	19.3	74.7	1.4	4.3	77.8	1.8	4.5
E	133.7	22.8	137.4	34.6	101.0	65.1	117.9	51.1	132.2	2.3	8.6	136.7	2.9	12.2
$\boldsymbol{A}_1$	137.8	13.6	175.8	4.0	124.3	57.6	165.8	32.9	145.2	2.4	7.4			
$\boldsymbol{A}_1$	231.2	14.0	233.9	5.6	226.2	59.6	233.5	31.4	225.9	2.9	0.6	227.4	2.2	0.7
E	236.7	7.6	243.6	13.3	234.0	31.7	240.8	69.3	241.0	4.3	0.9	242.4	4	0.2
E	264.0	13.0	283.0	38.0	258.2	60.4	278.0	48.5	266.2	2.3	5.4	266.8	4.4	0.4
E	288.5	26.2	345.8	9.2	278.4	61.6	340.7	40.4	293.9	4.6	3.6	279.5	5.5	10.6
E	349.0	10.0	368.1	5.0	342.5	42.5	363.6	41.0						
E	372.0	7.3	430.7	10.6	364.5	50.1	420.3	51.4				371.7	9.2	0.9
E	439.6	11.0	468.0	13.3	424.0	54.3	464.3	37.1				445.7	0.3	1.1
$\boldsymbol{A}_1$	476.2	41.2	503.7	49.1	469.8	41.0	502.8	106.2	472.2	7.1	0.01			
E	520.2	21.8	523.8	76.0	514.7	45.7	518.3	62.5	524.0	9.8	0.3	516.8	12.7	0.04
$\boldsymbol{A}_1$	549.5	36.9	606.2	27.1	542.1	78.8	595.3	102.3	550.6		0.07	551.8	2.3	1
Spin wave												603.6	9.9	0.01

In contrast, the permittivity calculated from the single-crystal spectra[159] is slightly higher, due to the absence of the A_1 modes whose dielectric strength $\Delta\varepsilon_j$ is lower than the *E*-symmetry modes.

We would like to stress that the temperature dependence of permittivity calculated from the phonon contributions has been previously published mostly below RT,[157,159] and only Ref. 156 reported ε(0,T) up to 900 K. Experimental low-frequency (i.e., below 1 MHz) dielectric data are also not available above RT due to the presence of significant leakage currents in $BiFeO_3$ at high temperatures. There is only one publication[158] presenting IR spectra of $BiFeO_3$ ceramics up to 1280 K, i.e., far above T_C, however, in this case, emissivity was measured instead of reflectivity above 600 K and ε(0,T) was not reported. In that work, Massa *et al.*[158] listed phonon parameters at selected temperatures, from which we recalculated ε(0,T); these values are presented for sake of

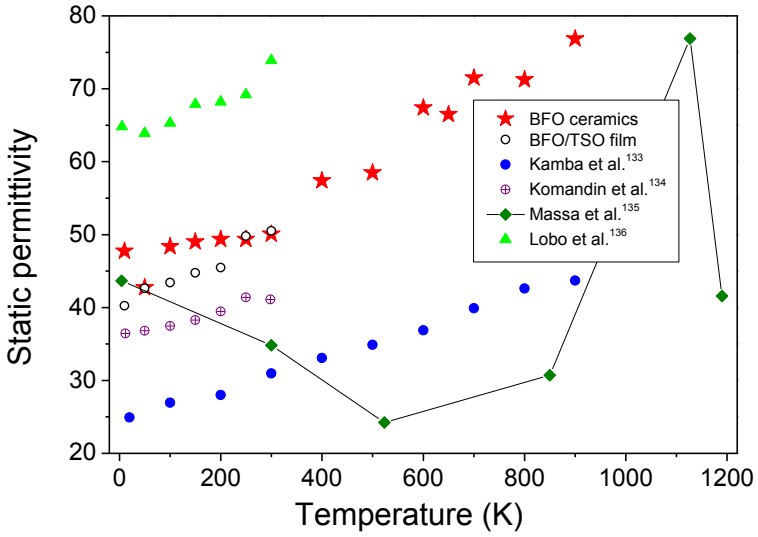

Figure 3.3 Temperature dependence of the static permittivity calculated from the sum of phonon contributions. The data for the ceramics and the film ($\boldsymbol{E}_{ext} \parallel [1\bar{1}0]$) from the current work are compared with previously published data obtained, on ceramics [156–159], and a single crystal.[159] The line connecting the data from Ref. 158 is a guide for the eyes. See the text for additional details.

comparison in Figure 3.3. One can see that, at T = 523 and 850 K, Massa *et al.*[158] obtained the lowest published values of ε(0). We also note the unusual increase in ε_∞ and ε(0,T) on cooling below RT; the latter appears to be in contradiction with the soft-mode frequency increase on cooling, reported in the same work. Finally, two additional phonon modes at T = 4 K, not predicted by the factor-group analysis, are reported in Ref. [158]. All these facts raise questions about whether these results describe the intrinsic properties of $BiFeO_3$. Nevertheless, it is worth noting the peak in Massa's data at the FE phase transition near 1120 K; this is the only experiment showing a dielectric anomaly at T_C in $BiFeO_3$. The peak is much lower than in other canonical FEs, apparently due to the first-order character of the phase transition from *R*3*c* symmetry to the high-temperature *Pnma* structure.[147,178]

3.1.3.2 Excitations in the $BiFeO_3$ thin film

The polarized IR reflectivity spectra of the bare (110) $TbScO_3$ substrate and reflectance spectra of the $BiFeO_3/TbScO_3$ thin film are shown in Figure 3.4. All $BiFeO_3$ mode frequencies obtained by fitting are listed in Table 3.1. We note that, on the one hand, the $BiFeO_3$ phonons below 150 cm^{-1} are better resolved in the $\boldsymbol{E}_{ext} \parallel [1\bar{1}0]$ polarization with respect to the substrate crystal axes, because the $TbScO_3$ phonons are weak in this case. On the other hand, the $BiFeO_3$ modes at 372 and 446 cm^{-1} are seen only in the $\boldsymbol{E}_{ext} \parallel [001]$ polarized spectra, due to a more favorable $TbScO_3$ spectrum in this region. Namely, the large TO-LO splitting of the $TbScO_3$ phonons within 370–480 cm^{-1} enhances the sensitivity of the IR reflectance to the thin-film phonons.[182]

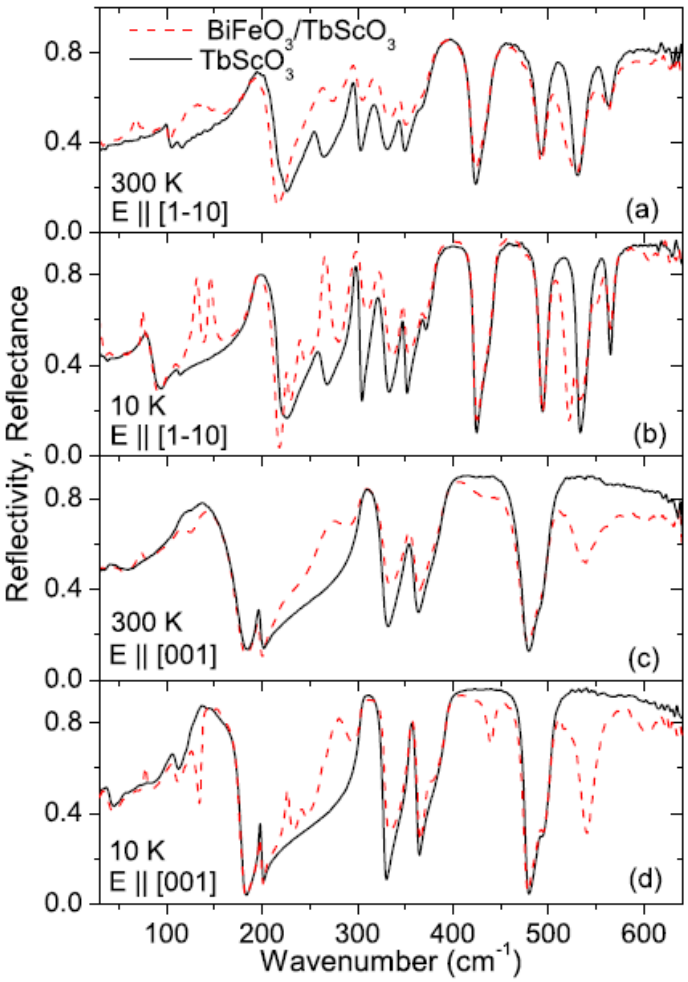

Figure 3.4 Room-temperature and 10 K IR reflectivity spectra of the $TbScO_3$ substrate and reflectance of the $BiFeO_3/TbScO_3$ thin film for polarizations (a) and (b) $\boldsymbol{E}_{ext} \parallel [1\bar{1}0]$ and (c) and (d) $\boldsymbol{E}_{ext} \parallel [001]$.

Therefore, due to the properties of $TbScO_3$, the two polarizations provide complementary information on the $BiFeO_3$ response. Note that some $TbScO_3$ phonons seen below 150 cm^{-1} (see Figure 3.4) exhibit anomalous temperature shifts and even splitting on cooling. This is probably caused by phonon interaction with the crystal field (and related electronic transitions).[183]

The in-plane lattice parameters of the (110) $TbScO_3$ substrate are slightly smaller than those of $BiFeO_3$, inducing only a small compressive strain (~0.24%) in the $(001)_{cub}$ epitaxial film. Here the orientation of the thin film is marked with respect to the pseudocubic crystal axis (which is denoted by the subscript "cub") of $BiFeO_3$. The ferroelastic and FE domain structure of $BiFeO_3/TbScO_3$ was investigated in Ref.179, 184, where two kinds of stripelike domains separated by $(010)_{cub}$ vertical boundaries were reported. The spontaneous polarization $\boldsymbol{P}$ in adjacent domains is rotated by 109° and its direction is tilted from the $[001]_{cub}$ direction.[184] In our IR spectra, only vibrations polarized in the film plane are active. Since the FE polarization $\boldsymbol{P}$ is tilted from the normal of the thin film plane, phonons of both E and A_1 symmetries can be excited. Nevertheless, we see only some of the modes due to our limited sensitivity to the thin film. In contrast to the ceramics samples, the phonon damping observed in the thin film is much lower (see Table 3.1). The values of the damping constants are comparable to those of single crystals,[159] which confirms the high quality of our epitaxial thin film. Similar to the case of $BiFeO_3$ ceramics, the phonon eigenfrequencies in the film decrease on heating, leading to an increase in the static permittivity $\varepsilon(0,T)$ (see Figure 3.3). The phonon frequencies of the $BiFeO_3$ ceramics and the film present no significant differences, which is clearly a consequence of the very small strain applied to the film by the substrate. The calculated $\varepsilon(0,T)$ is, however, smaller in the $BiFeO_3$ film than in the single crystal (see Figure 3.3), because, for the former sample, only strong phonons were revealed in the IR reflectance spectra.

In the low-temperature $\boldsymbol{E}_{ext} \parallel [001]$ spectra, a weak but sharp and clearly observable minimum in reflectance develops near 600 cm^{-1} [see Figure 3.4(d)]. We can exclude its phonon origin, because the factor-group analysis in rhombohedral structure does not allow an additional mode. A lower crystal symmetry is also excluded because our thin film has only 0.24% compressive strain; it is known that the films change the structure only with strain higher than 2%.[167] Also the multiphonon origin is not likely since multiphonon scattering usually decays on cooling; at RT, the peak intensity is markedly lower, close to our sensitivity limit [see Figure 3.4 (c)]. Interestingly, the position of the peak, approximately 604 cm^{-1}, corresponds to the maximum magnon energy observed at the Brillouin-zone boundary by inelastic neutron scattering in a $BiFeO_3$ single crystal.[169] Therefore, we assign this peak to scattering by the highest-energy part of the magnon branch. The magnon density of states can be activated in the

IR spectra due to the modulated cycloidal magnetic structure of $BiFeO_3$; the maxima in the density of states occur either at the maximal energy or at the Brillouin-zone boundary. Correspondingly, another peak in the density of states can be expected for the magnon branch at the K and M points. These magnons have an energy[172] of approximately 525 cm^{-1}, which falls into the range of the highest-energy phonon. We assume that this strong phonon screens the weak magnon signal, which is why we do not detect the corresponding absorption in the IR spectra. Finally, let us mention that in perovskites, the magnons from the Brillouin-zone boundary become frequently electrically active due to the exchange striction;[185] therefore, they can be called electromagnons.

3.1.3.3 Magnetic excitations in THz spectra of $BiFeO_3$ ceramics

Our efforts to measure THz spectra of the $BiFeO_3$ film failed, due to insufficient signal. This can be explained by the fact that the thin film only slightly absorbs the THz waves and the index of refraction n of $BiFeO_3$ is higher than that of the substrate only by ≈50%. We note that time-domain THz spectroscopy can be used only for studies of the thin films with n at least one order of magnitude higher than that of the substrate. As an example, such a technique was successfully used for investigation of the FE soft mode behavior near a strain-induced FE phase transition in $SrTiO_3$ thin films.[186]

In contrast, THz spectra of the $BiFeO_3$ ceramics were successfully measured at temperatures from 5 to 900 K. The spectra of the complex refractive index $N(\omega) = n(\omega) + ik(\omega)$, determined from experimental data for various temperatures, are presented in Figure 3.5. In magnetic systems, N depends on the complex permittivity ε^* and permeability μ^* via the relationship $N(\omega) = \mu^* \varepsilon^*$. Since we cannot resolve whether the observed modes contribute to μ^* (as magnons) or ε^* (as electromagnons or polar phonons), we only present $n(\omega), k(\omega)$ spectra in Figure 3.5(left).

In the THz spectra, one can see a gradual increase in n and k on heating. This is mainly caused by the softening of the TO_1 phonon and an increase in the phonon damping with heating. The weak maxima in the $k(\omega)$ spectra correspond to frequencies of magnetic excitations. Their temperature dependences are plotted in Figure 3.5(right) together with the modes observed in Raman[162,164] and IR[168,173] spectra. Note that the modes between 32 and 44 cm^{-1} become IR active only in external magnetic field.[145,173] Besides a good agreement between the frequencies of Raman and IR-active modes, one can see a gradual decrease in all mode frequencies with increasing temperature. Although the excitations should exist at least up to T_N, we fit our THz

spectra only up to 300 K, because, above RT, their damping is very high, precluding their exact fitting. We clearly distinguish five magnetic excitations. The three of them appearing up to 27 cm^{-1} correspond to the IR-active modes observed earlier by other authors.[157,168,173] In our spectra they exhibit an enhanced damping in comparison with single-crystal data, mainly due to the fact that we measured unpolarized spectra. At 5 K, two modes are seen with peak absorption frequencies of 53 and 56 cm^{-1}. These modes were not observed in IR spectra before, apparently because the samples used in previous studies were opaque above 40 cm^{-1}. These peak frequencies correspond well to the modes No. 7 and 8 reported in Raman spectra by Cazayous *et al.*.[162]Note that Komandin *et al.*[157] predicted a polar and heavily damped mode at an estimated frequency of 47 cm^{-1}, but their rough estimation was based on discrepancies between IR reflectivity and THz transmission spectra. Nagel *et al.*[173] discovered additional spin excitations near 40 and 43 cm^{-1}, but a magnetic field higher than 5 T was needed for the activation of these

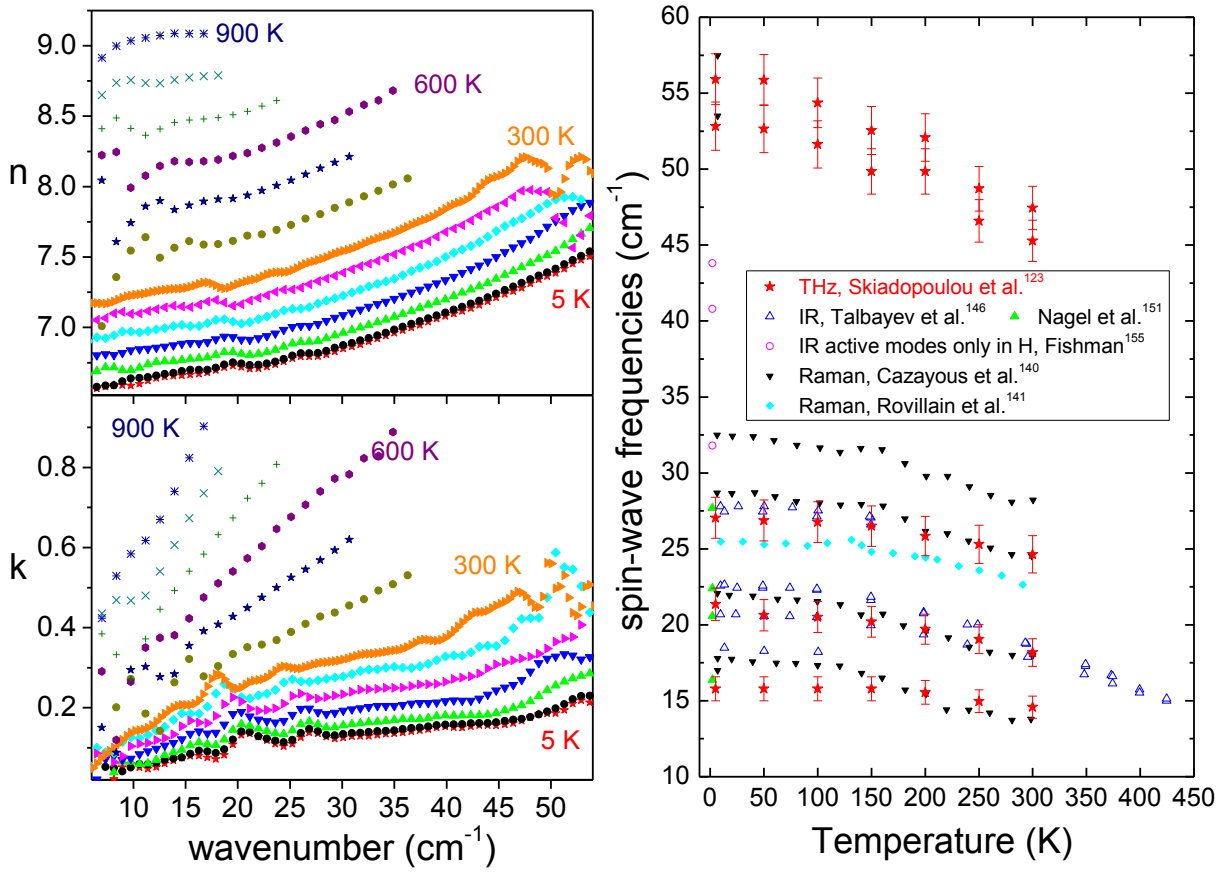

Figure 3.5 (left) Temperature dependencies of the (up) refractive index and (down) extinction coefficient spectra of BiFeO$_3$ ceramics, determined from the THz transmission. The spectra are shown for every 50 and 100 K below and above RT, respectively. (right) Temperature dependence of the spin excitation frequencies determined by fits of the absorption index spectra in the THz range compared with published frequencies obtained from Raman scattering [162,164] and far IR spectra.[173] The modes at ~32, 41, and 44 cm^{-1} were predicted by Fishman[175] and they become IR active only in magnetic field above 7 T.[173]

excitations in far-IR transmission spectra. Furthermore, Fishman predicted[145] a mode above 50 cm^{-1}, which should soften in an external magnetic field, and de Sousa *et al*. predicted[174] exactly the two modes which we observe.

We measured THz transmittance at 5 K under a magnetic field up to 7 T (see the $k(\omega)$ spectra in Figure 3.6). All modes exhibit small frequency shifts with increasing magnetic field. A similar behavior was reported by Nagel *et al*.,[173] but their frequency shifts were higher due to much higher values of the applied magnetic field (up to 31 T). We see also weak indications of the modes near 32, 35, 38, and 42 cm^{-1}, which correspond well (except the one at 35 cm^{-1}) to the magnetic-field induced modes of Ref. 173. In our measurements, while the sample was kept at a temperature of 5 K, applying the magnetic field of 7 T irreversibly changed the shape of the magnetic modes in the absorption index spectrum (see Figure 3.6), similarly to the observations in Ref.173. This behavior is probably a consequence of magnetic-field-induced changes in the geometry of magnetic domains and pinning the domain walls on defects. The pronounced modes near 53 and 56 cm^{-1} can be identified with the pair of modes predicted by Fishman near 45 cm^{-1} at H_{ext} = 15 T.[145] Thus, our observations confirm the complex effective Hamiltonian describing the magnetic interactions in $BiFeO_3$; it includes nearest and next-nearest neighbor exchange interactions, two Dzyaloshinskii-Moriya interactions, and an easy-axis anisotropy.[145] Very recently this model was also confirmed by low-energy inelastic neutron scattering spectra.[172]

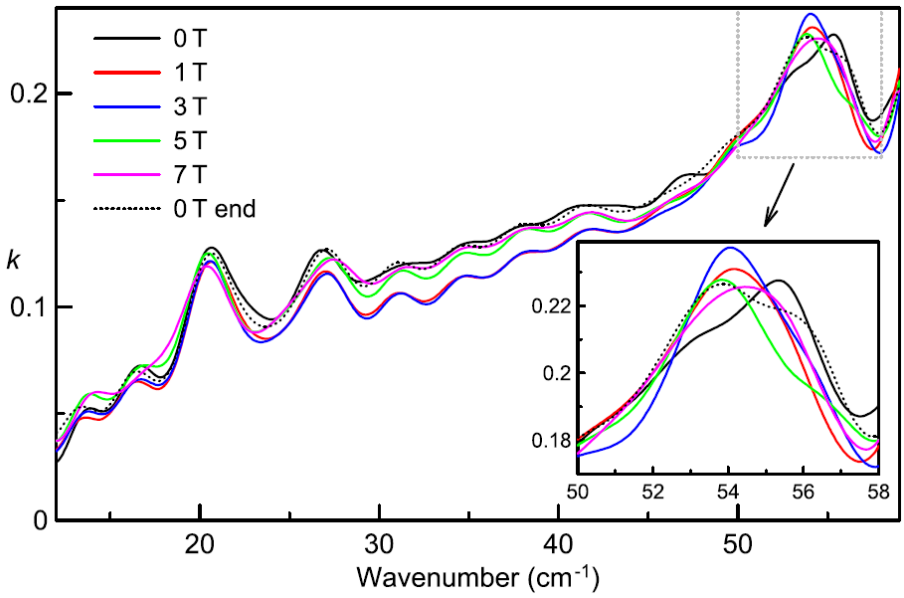

Figure 3.6 Magnetic field dependence of the experimental THz extinction coefficient in the $BiFeO_3$ ceramics measured at 5 K. The dotted line shows the zero-field spectrum after applying the magnetic field.

We were not able to fit unambiguously the THz spectra above 300 K using the modes seen at low temperatures, owing to their heavy damping at high temperatures. Nevertheless, a fit with one effective overdamped mode provided reasonable results. Surprisingly, this overdamped mode with a relaxation frequency around 15 cm^{-1} and $\Delta\varepsilon = 0.5 - 1.2$ ($\Delta\varepsilon$ rising with T) was necessary even above T_N, suggesting that there are still some paramagnons present in the paramagnetic phase. Alternatively, this mode might be due to a multiphonon or quasi-Debye absorption allowed in the non-centrosymmetric phase.[187]

Finally, we would like to stress that from unpolarized THz spectra, we could not distinguish whether our magnetic excitations are magnons or electromagnons. The symmetry analysis published by Szaller *et al.*,[81] however, allows electromagnons in the cycloidal *G*-type AFM phase of $BiFeO_3$. In analogy with selection rules for polar phonons which, in acentric lattices, are both IR and Raman active, we suggest that for spin excitations, their simultaneous IR and Raman activities indicate that they are electromagnons. The polar activity of spin excitations has been confirmed by Kezsmarki *et al.*,[177] who observed directional dichroism[81,188] of a $BiFeO_3$ single crystal in polarized far-IR spectra between 10 and 30 cm^{-1}.

3.1.4 **Conclusions**

An extensive study of IR vibrational spectra of $BiFeO_3$ ceramics and an epitaxial thin film is reported. The intensities of all phonons observed in the ceramics are higher than in the previous publications.[156–158] Thus, the static permittivity of our samples calculated from phonon contributions is close to the previously published single crystal data.[159] Some phonons slightly soften on heating, leading to an increase in the permittivity towards T_C. Nevertheless, the permittivity is much lower than in canonical FE perovskites, such as $BaTiO_3$ and $KNbO_3$, because the phonons in $BiFeO_3$ are much harder and the Born effective charges are much smaller. In addition, the phonons in a $BiFeO_3/TbScO_3$ epitaxial thin film were studied, showing parameters similar to those in $BiFeO_3$ single crystals. In the thin film, an additional weak excitation near 600 cm^{-1} was detected, which apparently corresponds to a peak in the magnon density of states possibly activated due to the incommensurately modulated magnetic structure of $BiFeO_3$. Time-domain THz spectra of $BiFeO_3$ ceramics reveal most of the spin excitations previously observed in single crystals.[168,173] Also, at 5 K, a pair of IR-active modes near 55 cm^{-1} were observed, which corresponds to spin excitations theoretically predicted by de Sousa *et al.*[174] and Fishman.[145] This observation confirms the particular form of the Hamiltonian suggested by Fishman for the explanation of the magnetic interactions in $BiFeO_3$.

3.2 Pb_2NbTeO_6 double perovskite: an antipolar antiferromagnet

Pb_2MnTeO_6, a new double perovskite, has been synthesized for the first time. Section 3.2 demonstrates the rare combination of an antipolar AFM structure, as reported in Ref. 143.

Its crystal structure has been determined by Synchrotron X-ray and Powder Neutron Diffraction. Pb_2MnTeO_6 is monoclinic (*I*2/*m*) at room temperature with a regular arrangement of all the cations in their polyhedra. However when the temperature is lowered to ~120 K it undergoes a phase transition from *I*2/*m* to *C*2/*c* structure. This transition is accompanied by a displacement of the Pb atoms from the center of their polyhedra due to the $6s^2$ lone pair electrons, together with a surprising off-centering of Mn^{2+} (d^5) magnetic cations. This strong first order phase transition is also evidenced by specific heat, dielectric, Raman, and IR spectroscopy measurements.

The magnetic characterizations indicate an AFM order below T_N ~ 20 K; analysis of Powder Neutron Diffraction data confirm the magnetic structure with propagation vector $\boldsymbol{k}$ = (0 1 0) and collinear AFM spins. The observed jump in dielectric permittivity near ~150 K implies possible antiferroelectric (AFE) behavior, however the absence of switching suggests that Pb_2MnTeO_6 can only be antipolar. First principle calculations confirmed that the crystal and magnetic structures determined are locally stable, and that AFE switching is unlikely to be observed in Pb_2MnTeO_6.

The strong first order structural phase transition occurring above 120 K is previewed below, as observed by heat capacity measurements. T_C exhibits strong temperature hysteresis.

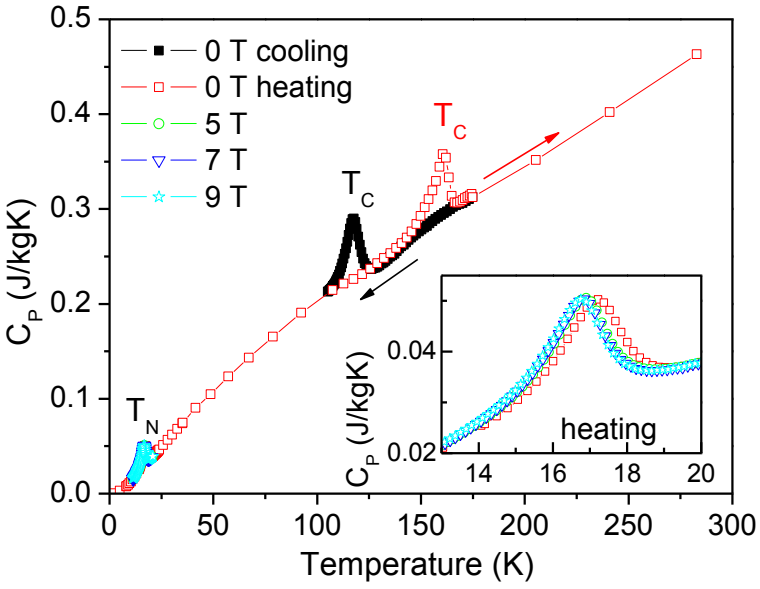

3.2.1 **Introduction**

In the past years, $A_2BB'O_6$ ordered double perovskites have been widely investigated due to the huge variety of interesting physical properties, including magnetoresistance, ferroelectricity, and piezoelectricity.[189–191] Also magnetoelectric behavior, where magnetism and ferroelectricity are coupled, is extensively searched for these phases, for practical applications in memories, sensors and communication.[192,193] These magnetoelectric materials have the intrinsic ability to couple the electric polarization to magnetization, and *vice versa*, with a new degree of freedom for the potential design of conventional devices. However, there are few compounds where electric dipole and spin orders coexist, and the ones reported present very low magnetoelectric response and/or low ordering temperatures. Therefore it is a grand challenge to find materials with high magnetoelectric coupling above room temperature (RT).

To design new magnetoelectric materials, the phases must contain magnetic cations and satisfy any of the requirements for ferroelectricity: i) contain lone pair cations to produce polarization; ii) form non-centrosymmetric structures with a cation able to move from the center of its position to create an electric dipole (usually a d^0 ion with second order Jahn–Teller (SOJT) effect); iii) present a collinear, cycloidal or transverse conical magnetic structure, which induces an electric dipole; iv) undergo a transition into a charge-ordered polar state.[194–200] In this work, we investigate a double perovskite with Pb^{2+} in the A site. Pb^{2+} has a $6s^2$ lone electron pair that can be polarized along a particular direction by its off-center displacement, which results in a highly asymmetric coordination environment. This displacement is caused by the high covalency of Pb(6*s*)−O(2*p*)* bonds due to the hybridization of the Pb 6*s* states with the antibonding oxygen states, which is generally considered to be the effect of a stereochemically active lone electron pair.[201,202] For example, in Pb_2MnWO_6 the displacement occurs along <100> and <010> cubic axes, resulting in an antipolar arrangement (i.e. similar to an AFE order, but in contrast to it, it cannot be transformed to an induced FE phase by application of an electric field).[203]

Pb-based double perovskites with magnetic cations in the B-sites are potentially good candidates for both magnetic and FE orderings. Pb_2FeNbO_6 and Pb_2FeTaO_6 have been extensively studied since both exhibit FE order close to RT with polarization ($\boldsymbol{P}_s$) || <111> and antiferromagnetic (AFM) order below a Néel Temperature (T_N) ~ 150 K.[204,205] These materials frequently exhibit superparamagnetic clusters even above RT, and due to the biquadratic magnetoelectric coupling ($\sim M^2P^2$) the magnetic susceptibility exhibits anomalies at the FE phase transition temperature.[206] This coupling can be very large and can even allow the switching of the FE domains by a magnetic field, as was recently demonstrated at RT in the solid solution

between $PbFe_{1-x}Ta_xO_3$ and $PbZr_{1-x}Ti_xO_3$.[207] With this aim, the synthesis of Pb_2MnTeO_6 was undertaken in this investigation and we demonstrate that it exhibits an antipolar ordering below 120 K and AFM ordering below 20 K.

3.2.2 **Experimental Details**

3.2.2.1 Sample Preparation and Determination of its Crystal and Magnetic Structures

Pb_2MnTeO_6 was prepared by a standard solid-state technique with reagent-grade starting materials PbO, $MnCO_3$ and TeO_2. A stoichiometric mixture of the starting solids was thoroughly ground and heated in an O_2 flow at 1073 K for 12 hours to obtain a pure sample. The product was initially characterized by Powder X-ray Diffraction (PXD) for phase identification and purity. PXD was performed in a Bruker-AXS D8 diffractometer (40 kV, 30 mA), controlled by a DIFFRACTplus software, in Bragg-Brentano reflection geometry with Cu Kα, λ = 1.5406 Å. For the structural refinements, Powder Neutron Diffraction (PND) data were collected at RT and 14 K at the POWGEN instrument in the Spallation Neutron Source in Oak Ridge National Laboratory.[208] Two patterns were collected to cover *d*–spacing between 0.4 and 8.5 Å. The PND data were refined by the Rietveld method, with the FullProf program.[209,210] Synchrotron Powder Diffraction (SPXD) measurements at 11 K and 50 K were made at beamlines X17A and X16C of the National Synchrotron Light Source, respectively. Those data were refined with Topas-Academic.[211] X-ray absorption near edge spectroscopy (XANES) was collected simultaneously in both the transmission and fluorescence mode for powder samples on beam line X-19A at the Brookhaven National Synchrotron Light Source. The results from SPXD and XANES will not be presented in the current thesis, but they are available in the Supporting Information (SI) of Ref. 143.

3.2.2.2 Magnetic, Dielectric and Heat Capacity Measurements

Magnetization measurements were carried out in a commercial Quantum Design superconducting quantum interference device (SQUID) magnetometer MPMS5. The magnetization was measured in zero field cooled (ZFC) and field cooled (FC) conditions under a 0.1 T magnetic field, for temperatures ranging from 5 to 300 K. Isothermal magnetization curves were obtained at 5 and 300 K under an applied magnetic field that varied from -5 to 5 T. Differential Scanning Calorimeter (DSC) experiments were performed on a Perkin Elmer DSC 7 with liquid nitrogen cooling (93–300 K). Pyris Software (Version 11.0.3, Perkin Elmer

Instruments, 2009) was used for control and evaluation. The temperature dependence of Heat Capacity (C_P) was measured with the Heat Capacity option of the Physical Property Measurement System (PPMS9, Quantum Design). The standard relaxation method was used for the measurements of low and high temperature parts. The data close to the structural transition were measured by application of large temperature pulse and independent evaluation of heating and cooling part, in order to capture the effect of hysteresis. Low-frequency (1 Hz–1 MHz) dielectric measurements were performed between 40 and 300 K with a Novocontrol Alpha-A high-performance frequency analyser. Cooling and heating rate was 5 K/min. The sample was placed in a He-flow Leybold cryostat; good thermal contact was secured by He gas in the sample chamber. We attempted to measure an AFE hysteresis loop close and below T_C at frequencies from 1 to 50 Hz with our custom-made setup. The results from DSC will not be presented in the current thesis, but they are available in the SI of Ref. 143.

3.2.2.3 THz, Infrared and Raman Studies

The experimental details of IR reflectivity, Raman and time-domain THz spectroscopies used for the study of spin and lattice excitations were according to Chapter 2.

3.2.2.4 Theoretical Calculations

Density functional theory (DFT) calculations were performed with the Vienna Ab-initio Simulation Package. PBEsol pseudopotentials with Pb 5*d*, 6*s*, and 6*p*; Mn 3*s*, 3*p*, 3*d*, and 4*s*; Te 5*s* and 5*p*; and oxygen 2*s* and 2*p* valence states were used. A 500 eV plane wave cutoff was used for all calculations. A *k*-point mesh with approximately 0.2 $Å^{-1}$ spacing between each point was used. Structural relaxations were considered converged once the force on each atom was less than 1 meV/Å. The Dudarev approach to DFT+*U* was used to approximate electronic correlation in the Mn *d*-orbitals. Reported results used U = 5 eV. Varying U between 3 and 7 eV did not significantly alter our results. The Isotropy Software Package was used to study symmetry related properties.

3.2.3 **Results and discussion**

3.2.3.1 Crystal Structure

PXD of Pb_2MnTeO_6 demonstrates the formation of a pure perovskite-based compound (Figure 3.7). The crystal structure refinements were performed from PND at RT and 14 K, and confirmed by SPXD. At RT Pb_2MnTeO_6 is refined with the monoclinic space group *I*2/*m* (No. 12). Figure 3.7(up) shows the excellent agreement between PND experimental and calculated data and the inset show how other space groups cannot explain the splitting of some of the reflections. Only $P2_1/n$ could explain the data similar to *I*2/*m*, but the reflections $h + k + l \neq 2n$ do not appear, which indicates *I*-centering of the unit cell. Moreover, the *R* factor for the *I*2/*m* model (R_{Bragg} = 3.83%) is significantly better than that of the $P2_1/n$ model (R_{Bragg} = 5.72%). There are only a few other reported double perovskites with the same symmetry including Pb_2CoTeO_6, Pb_2CoWO_6, Sr_2CoOsO_6 and Sr_2CoTeO_6.[212–215] The cell parameters of *I*2/*m* model are related to the ideal cubic perovskite aristotype ($a_0 \approx 4$ Å) as $a \approx b \approx \sqrt{2}a_0$, and $c \approx 2a_0$. It is defined with one single A-site for Pb atoms at 4*i*(*x*, 0, *z*), two crystallographically independent B positions for Mn at 2*a*(0, 0, 0) and Te at 2*c*(0, 0, ½) and two nonequivalent oxygen atoms (O1 at 4*i*(*x*, 0, *z*) and O2 at 8*j*(*x*, *y*, *z*)) (see tables 1 and 2 of Ref. 143 for the refined crystallographic parameters, atomic coordinates, thermal parameters and reliability factors at RT, interatomic distances and bond angles). At RT there is no significant movement of the Pb atom from the center of the polyhedron. The average

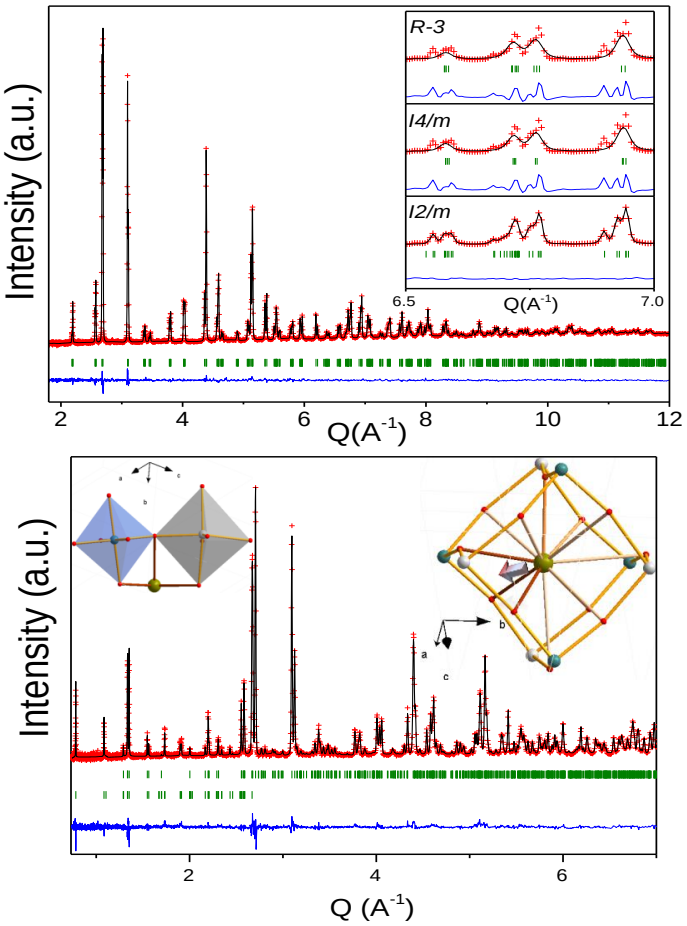

Figure 3.7 (up) Observed (crosses), calculated (full line) and difference (bottom) PND Rietveld profiles at RT. Upper inset shows the refinement for Pb_2MnTeO_6 in *R-3, I4/m and I2/m* space groups. (down) PND Rietveld profiles at 14 K. The two sets of reflection patterns correspond to crystallographic and magnetic structures. Inset left: TeO_6 (blue) and MnO_6 (grey), where it is shown the displacement of Mn inside the Oh. Inset right: Environment of Pb cations and its off-center.

<Pb-O> bond distance at RT is 2.874 Å, comparable to that expected from the ionic radii sums of 2.89 Å for $^{XII}Pb^{2+}$ (i.r.: 1.49 Å) and $^{VI}O^{2-}$ (i.r.: 1.40 Å);[216] and also similar to Pb-O distances in other double perovskites, e.g., 2.814 Å in Pb_2MnReO_6,[217] and 2.898 Å in Pb_2MnWO_6.[203] In addition, MnO_6 and TeO_6 are regular and do not demonstrate cationic displacements. The average <Mn-O> and <Te-O> bond distances at RT, 2.159 Å and 1.915 Å, respectively, are somewhat smaller than the calculated values for $^{VI}Mn^{2+}$ (i.r.$_{(High\ Spin)}$: 0.83 Å) and O^{2-} of 2.23 Å and $^{VI}Te^{6+}$ (i.r.: 0.56 Å) and O^{2-} of 1.96 Å, from Shannon ionic radii tables.[216] However, similar Pb-based double perovskites, Pb_2MnWO_6 and Pb_2MnReO_6, have similar Mn-O bond distances (2.124 Å and 2.106(5) Å, respectively), and Pb_2CoTeO_6 has a comparable Te-O distance (1.929(1) Å) as well.[212]

When the temperature is lowered, around 120 K the compound undergoes a structural phase transition, as demonstrated by $C_P(T)$, dielectric measurements, IR and Raman spectroscopies (see below). The PND data at 14 K (Figure 3.7) are explained with the monoclinic *C*2/*c* (No.15) space group, with a relation of the unit cell parameters to those of the ideal cubic perovskite as $a \approx c \approx \sqrt{6}a_0$, and $b \approx \sqrt{2}a_0$. This low-temperature phase is unusual for perovskites. It was described for similar Pb_2RSbO_6 double perovskites (R = rare earths),[218,219] which contain a completely ordered array of alternating BO_6 and $B'O_6$ octahedra sharing corners, tilted in antiphase along the three pseudocubic axes (with an $a^-b^-b^-$ tilting scheme). Also the transition sequence from *C*2/*c* to *I*2/*m* space groups has been never reported before, since for Pb_2RSbO_6 the sequence is $C2/c \rightarrow P2_1/n \rightarrow R3 \rightarrow Fm3m$, different from the one observed in Pb_2MnTeO_6. In *C*2/*c* structure, Pb atoms are placed at the Wyckoff 8*f*(*x*, *y*, *z*) A sites; Mn and Te atoms at the 4*e*(0, *y*, ¼) and 4*d*(¼, ¼, ½) B and B' sites, respectively; and oxygen atoms are located at three crystallographically nonequivalent positions at 8*f*(*x*, *y*, *z*). The Bragg *R*-factors obtained at 14 K for the refinement of the two PND frames are 5.82% and 6.32%. The refinement of the occupancy of Pb and O atoms indicates full occupancies; no oxygen vacancies at any position and no antisite disorder between Mn and Te, at RT and 14 K (see Ref. 143 for the tables with the refined parameters). This structure is confirmed by SPXD data collected at 11 K (see SI of Ref. 143), showing that the magnetic diffraction peaks discussed below do not have any nuclear contribution from a lower lattice symmetry. SPXD also reveal the same structure at 50 K, proving that the only structural transition is the one in the range 120 K to 160 K; *i.e.*, the 20 K transition is purely magnetic (structural parameters from the X-ray refinements are given in the SI of Ref. 143). The following analysis is based on the neutron data, which are much more accurate.

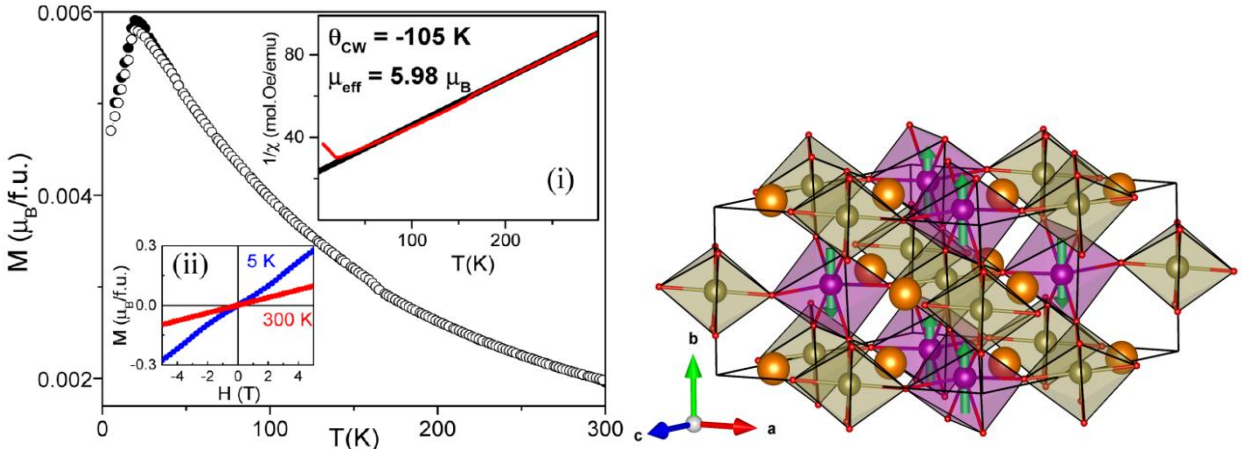

Figure 3.8 (left) Susceptibility vs temperature of Pb2MnTeO6 ceramics measured at 0.1 T. (insets) (i) Inverse of the susceptibility fitted to the Curie−Weiss Law. (ii) Hysteresis loops at 5 and 300 K. (right) Magnetic structure with the spins over the Mn atoms (purple atoms). Te atoms are brown, Pb atoms are orange, and oxygen are red.

At low temperature the structure changes, significantly increasing the distortion. Pb atoms are now situated in distorted polyhedra, in which we can consider 8-fold coordination if we discard the Pb-O distances longer than 3.1 Å. Pb atoms present off-center displacement, due to the $6s^2$ lone pair. There are three Pb-O shorter distances creating a PbO_3E environment (E being the lone pair), as was described in Pb_2TmSbO_6.[219] The right inset of Figure 3.7(down) shows the environment of Pb atoms and the arrow marks the direction of their displacement, which is almost along the *b* direction. This antiparallel displacement of Pb from the centroids of their polyhedra motivated the study of possible AFE character in this compound. The Pb off-centering also implies the displacement of Mn cations inside their octahedra (0.044 Å) closer to one octahedron edge formed by the O3 atoms and moving away from the Pb-O shorter distances (see left inset of Figure 3.7(down)); while Te cations are not displaced. This off-center displacement is highly unusual for the magnetic and Jahn-Teller-inactive Mn^{2+} (d^5) cation, mimicking the behavior which usually occurs for d^0 cations. The phenomenological Brown's Bond-Valence Model (BVS)[220,22134] helps to estimate the valences of the cations, by an empirical relationship between the observed bond-lengths and the valence of a bond. The values obtained at RT, Mn (2.22(1)+) and Te (6.04(3)+), are close to the expected values of 2+ and 6+; although the slightly higher valence observed for Mn could suggest a minor compressive stress on these bonds. We corroborate the oxidation states of Mn^{2+} and Te^{6+} by X-ray absorption spectroscopy (SI of Ref. 143).

3.2.3.2 Magnetic Measurements

The magnetization *vs.* temperature curves recorded in ZFC and FC modes (Figure 3.8(left)) show that Pb_2MnTeO_6 undergoes an AFM transition at T_N ~ 17 K, as observed by a drop in the

magnetization. ZFC and FC curves show no divergence in the entire 5-300 K temperature region. The high temperature data were fitted to a Curie-Weiss law, $\chi = C/(T-\theta_{CW})$ (inset (i) of Figure 3.8(left)). The fitting allowed us to extract the effective magnetic moment, $\mu_{eff} = 5.98\ \mu_B$, which agrees well with $\mu_{Mn2+} = 5.92\ \mu_B$. The Curie-Weiss constant, $\theta_{CW} = -105$ K, indicates strong AFM correlations in the system. Note that the fit was done for the temperature range above the structural transition (T > 160 K). In inset (ii) of Figure 3.8(left), the isothermal magnetization curves are shown. They indicate a linear paramagnetic behavior at 300 K and an AFM behavior at 5 K showing a lack of saturation even at the highest measured field (as expected for an AFM material); however a slight curvature is observed in the M vs H data at 5 K, indicating small competition of magnetic interactions at low temperature.

3.2.3.3 Magnetic Structure

The magnetic structure determination was carried out from PND at 14 K. New reflections of magnetic origin appear in the PND diagram (SI of Ref. 143), which can be indexed with the $\boldsymbol{k}$ = (0 1 0) propagation vector. The magnetic symmetry analysis has been performed with the ISODISTORT software.[222] The collinear AFM solution was found with a magnetic space group P_C2/n, subsequently transformed into the set of constraints to be used in the Fullprof program.[211] In this case, the crystallographic and magnetic unit cells coincide, but the crystallographic unit cell is *C*-centered, whereas the magnetic unit cell is primitive. So, the translation symmetry is actually different for the crystallographic and magnetic structures, lifting out the *C*-centering translation to correspond to the (0 1 0) propagation vector. After the full refinement of the profile, including the magnitude of the magnetic moments, the best discrepancy factor of R = 9.78 % was obtained. The magnetic moment on the Mn atom has a value of 3.64(9) μ_B and is aligned along the *b* axis of the *C*2/*c* unit cell (<110> axis of conventional perovskite subcell). A view of the magnetic structure is displayed in Figure 3.8(right). The magnetic moments on Mn atoms are ferromagnetically arranged into chains running along the *b* axis. Each chain is surrounded by four nearest neighbor chains with the opposite direction of spins, resulting in the AFM structure. The long distance superexchange magnetic interactions via Mn–O–Te–O–Mn paths, account for the relatively low T_N. Other examples of AFM double perovskites with similar T_N and containing one magnetic cation at B site and one non-magnetic ion at B′ are Sr_2CrSbO_6 (T_N = 12 K),[223] Sr_2FeWO_6 (T_N = 37 K)[224] and Pb_2CoTeO_6 (T_N = 16 K).[212]

3.2.3.4 Heat Capacity

Figure 3.9 shows the temperature dependence of C_P. The peaks seen near 117 K (cooling) and 160 K (heating) indicate a structural phase transition that exhibits a large thermal hysteresis, characteristic of a first-order phase transition. Similar values of critical temperature (T_C) were obtained with DSC (SI of Ref. 143). The measurements were reproducible and the change of enthalpy was 0.45 ± 0.01 J/g at T_C. The peak near 17.2 K manifests the AFM ordering, which shifts down by 0.4 K in external magnetic field of 9 T (Inset of Figure 3.9).

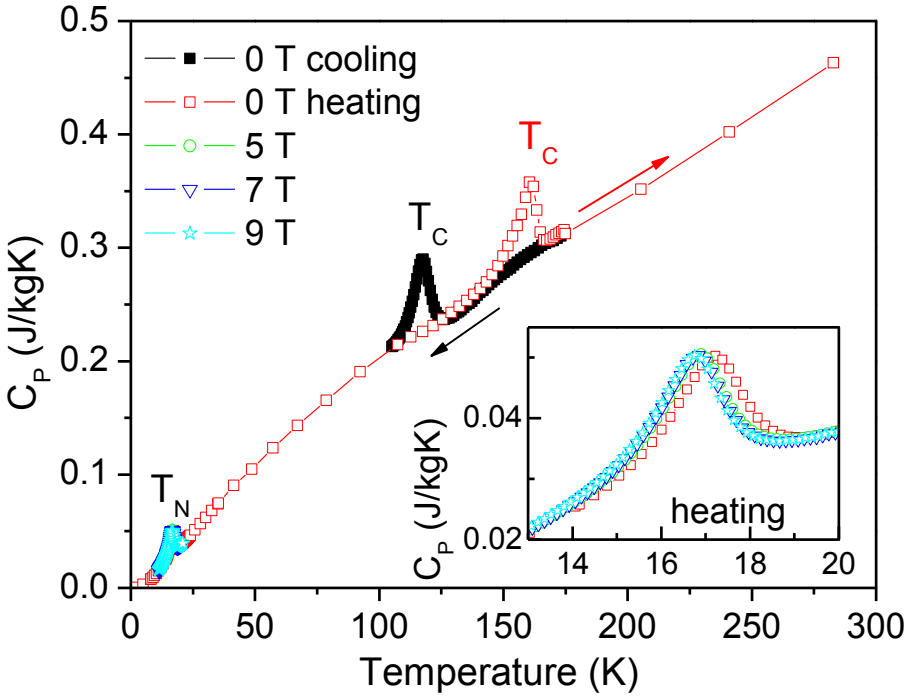

Figure 3.9 Temperature and magnetic field dependence of heat capacity. Large thermal hysteresis of T_C is seen. T_N exhibits 0.4 K shift down with an applied magnetic field.

3.2.3.5 Dielectric and ac Conductivity Measurements

Dielectric data (Figure 3.10) are strongly influenced by leakage conductivity of the sample. Note that the conductivity σ' drastically increases with both frequency and temperature (Figure 3.10(c)); at 50 K the σ' is 6 orders of magnitude higher at 900 kHz than at 1 Hz. This is caused by a non-homogeneous conductivity in the ceramic sample; the grains exhibit large conductivity (seen at high frequencies), while the grain boundaries are less conducting and therefore they radically reduce the low-frequency σ'. The resistive grain boundaries are responsible for the creation of internal barrier layer capacitors with ultra low thickness. They enhance the electric capacity of the sample and cause a "giant" effective permittivity at low frequencies, which reaches in our case values about 10,000 at temperatures above 200 K (see SI of Ref. 143). This

mechanism of creation of "giant" or "colossal" dielectric permittivity is well known in many dielectrics and multiferroics with non-negligible conductivity.[225] The conductivity is also responsible for the high dielectric loss (Figure 3.10(b)). Nevertheless, the influence of conductivity on ε' decreases with increasing frequency, therefore ε' in Pb_2MnTeO_6 seen at 900 kHz has intrinsic values, at least, up to 200 K. In Figure 3.10(a), one can see remarkable step-down of $\varepsilon'(T)$ near 120 K (on cooling), typical for AFE[226] or improper-ferroelectric[227] phase transitions. According to our structural refinement, the low-temperature $C2/c$ crystal structure is centrosymmetric, thus the FE order is excluded. Similar change of $\varepsilon'(T)$ is seen on heating, but the anomaly occurs ~40 K higher, which is evidence for a first-order character of the phase transition. The temperatures of dielectric anomalies correspond well to the temperatures of the phase transitions seen in $C_P(T)$ (Figure 3.9). The centrosymmetric character of the both phases was also confirmed by Second Harmonic Generation (SHG) that showed only very weak SHG response (close to the noise limit) even with an unusually long collection time.

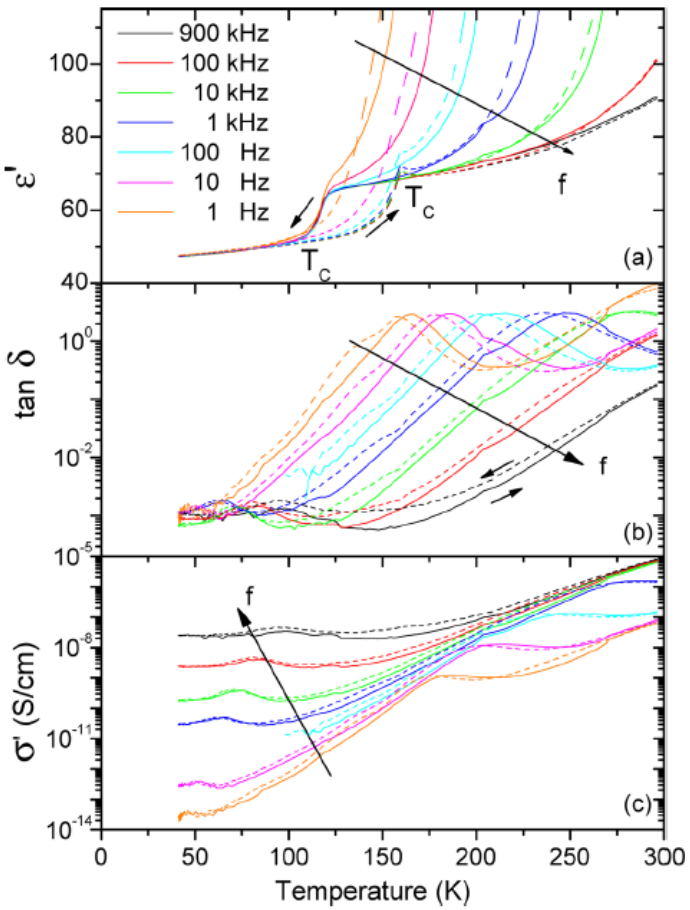

Figure 3.10 Temperature dependence of (a) dielectric permittivity ε′, (b) dielectric loss tan δ, and (c) conductivity σ′ measured at various frequencies on cooling (solid lines) and heating (dashed lines). Large thermal hysteresis of drop-down in ε′ is typical for first-order phase transition.

Since the unit cell doubles below T_C in Pb_2MnTeO_6 like in AFEs and the step down of ε' observed at T_C is reminiscent of a dielectric anomaly at AFE phase transition, we tried to measure AFE hysteresis loops. Only linear increase of polarization with electric field typical for paraelectrics was observed (Figure 3.11), but we cannot exclude that AFE hysteresis loop appears at higher electric fields than our 28 kV/cm, however, we could not apply higher field due to a finite conductivity of the sample.

Similar step down of permittivity as in our case has been observed in other double perovskites including Pb_2CoTeO_6[212] and Pb_2MnWO_6.[203] Authors of both references claimed that their low-temperature phases are AFE although they did not measure hysteresis loops. Here we would like to stress that both materials are likely antipolar and only hysteresis loop measurements can distinguish between AFE (switchable polarization) and antipolar (non-switchable) behavior.

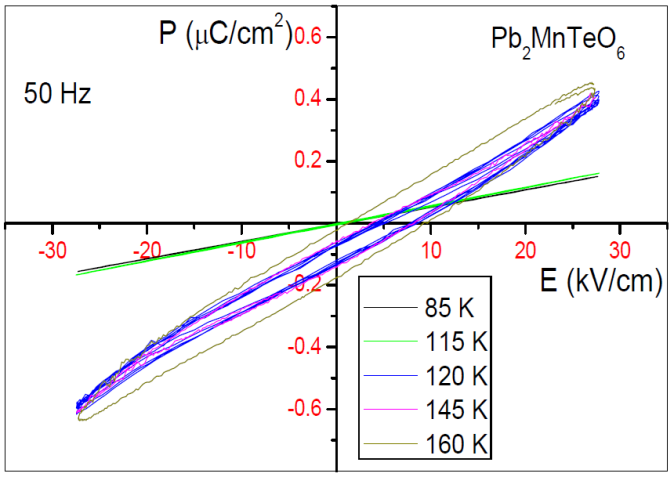

Figure 3.11 Polarization hysteresis loops measured at 50 Hz and at selected temperatures. Loose oval loops are seen above T_C due to leakage conductivity in the ceramics. Straight line seen below T_C is characteristic for paraelectric behavior. Similar, just slightly more opened loops were observed at 10 Hz.

3.2.3.6 Infrared and THz Spectroscopy

Intrinsic ε' is determined by the sum of phonon and electron contributions to the permittivity (it corresponds to the low-frequency edge of THz ε' in Figure 3.12(b) and (c)), so if $\varepsilon'(T)$ changes near T_C (120–150 K), some phonon shifts and splittings are expected. For that reason, IR reflectivity and THz transmission spectra were measured down to 12 K. Dramatic changes of the reflectivity with temperature can be observed in Figure 3.12(left (a)). Four asymmetric reflection bands abruptly split below T_C. Fits of IR reflectivity and experimental THz permittivity reveal 16 IR active (i.e. polar) phonons above 150 K and 30 phonons at lower temperatures (see mode parameters in SI of Ref. 143). Jumps in phonon frequencies are clearly seen near T_C in the temperature dependence of polar phonon frequencies (Figure 3.13(left)). For the explanation of the number of observed phonons, we performed factor group analysis of lattice vibrations, using the known site symmetries of atoms, obtained from our structural investigations. In the high-temperature phase *I*2/*m*, the primitive unit cell contains one formula unit with 10 atoms with 30 degrees of freedom, and therefore, 30 phonons are expected. The following phonon counts and symmetries in the Brillouin Zone (BZ) center were obtained:

$$\Gamma_{I2/m} = 7A_g(x^2, xy) + 7A_u(z) + 5B_g(xz, yz) + 11B_{1u}(x, y) \qquad 3.1$$

Here, *x*, *y*, and *z* mark electric polarizations of the IR radiation for which the phonons are IR active, whereas the rest of the symbols are components of the Raman tensor. After subtraction of

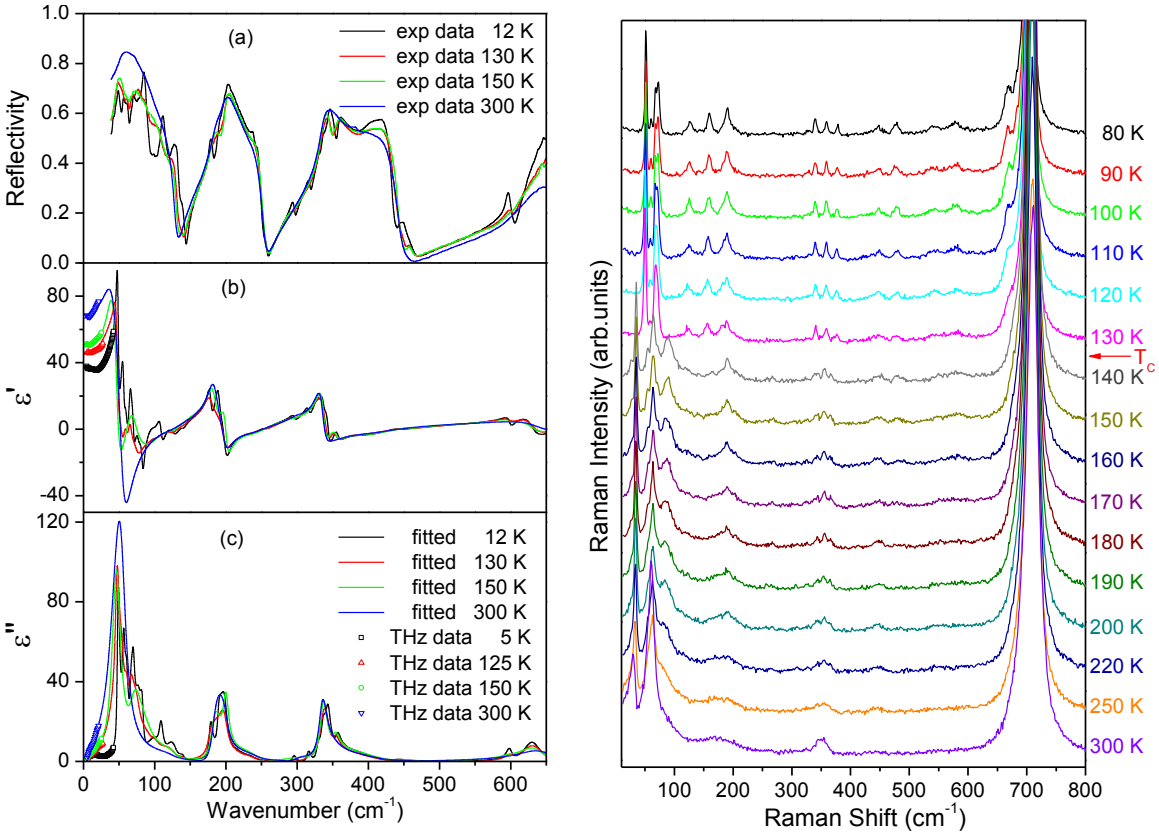

Figure 3.12 (left) (a) IR reflectivity spectra at selected temperatures together with (b) real and (c) imaginary part of complex dielectric permittivity obtained from fits of IR reflectivity. Symbols at low frequencies are experimental data obtained from time-domain THz spectrometer. (right) Raman scattering spectra taken at various temperatures. Abrupt change typical for structural phase transition of the first order is seen between 130 and 140 K.

$1A_u$ and $2B_{1u}$ symmetry acoustic phonons, 15 IR and 12 Raman active phonons are expected in the spectra of the high-temperature phase.

In the low-temperature phase the crystal structure changes to *C2/c* and the unit cell doubles, so 60 phonons are expected. We obtained the following symmetries and activities of the phonons:

$$\Gamma_{C2/c} = 13\boldsymbol{A_g}(x^2, xy) + 16\boldsymbol{A_u}(z) + 14\boldsymbol{B_g}(xz, yz) + 17\boldsymbol{B_u}(x, y) \qquad 3.2$$

Likewise after subtraction of 3 acoustic modes, 30 phonons are IR active and 27 phonons should be active in the Raman spectra. As expected, 30 phonons were observed in the IR spectra below 130 K (Figure 3.12(left)) and 15 polar phonons in the high-temperature *I*2/*m* phase, which exactly correspond to the factor group analysis. One extra mode observed in both phases can be a geometrical resonance in anisotropic media, caused by two LO modes with similar frequencies.[228] An alternative possible explanation is that the extra mode is very weak (one near 20 cm^{-1} – see SI of Ref. 143, Figure S8), which can be a central mode, that describes dynamical hopping of Pb cations among several equivalent positions. This central mode is seen only in the

THz dielectric loss and can be as well caused by multiphonon absorption. The only surprising observation is, that this very weak and heavily damped mode remains in the THz spectra even in the low-temperature phase, where both central mode and multiphonon absorption should disappear. The last and most probable explanation for the extra mode is that it is a defect-induced mode, which can be heavily damped, if its frequency lies in the range of acoustic phonons.[229]

3.2.3.7 Raman Spectroscopy

Phonons in the Raman scattering spectra (Figure 3.12(right)) exhibit gradual decrease of damping on cooling and an abrupt change between 140 and 130 K, where Pb_2MnTeO_6 undergoes the phase transition. Some of the modes shift and some of them split below T_C (see temperature dependence of mode frequencies in Figure 3.13(right)). We can again compare the number of observed phonons with theoretically predicted phonons. In the high-temperature phase, we see 11 Raman active phonons instead of 12 allowed by symmetry. At low temperatures we observed 15 Raman active modes instead of the 27 allowed.

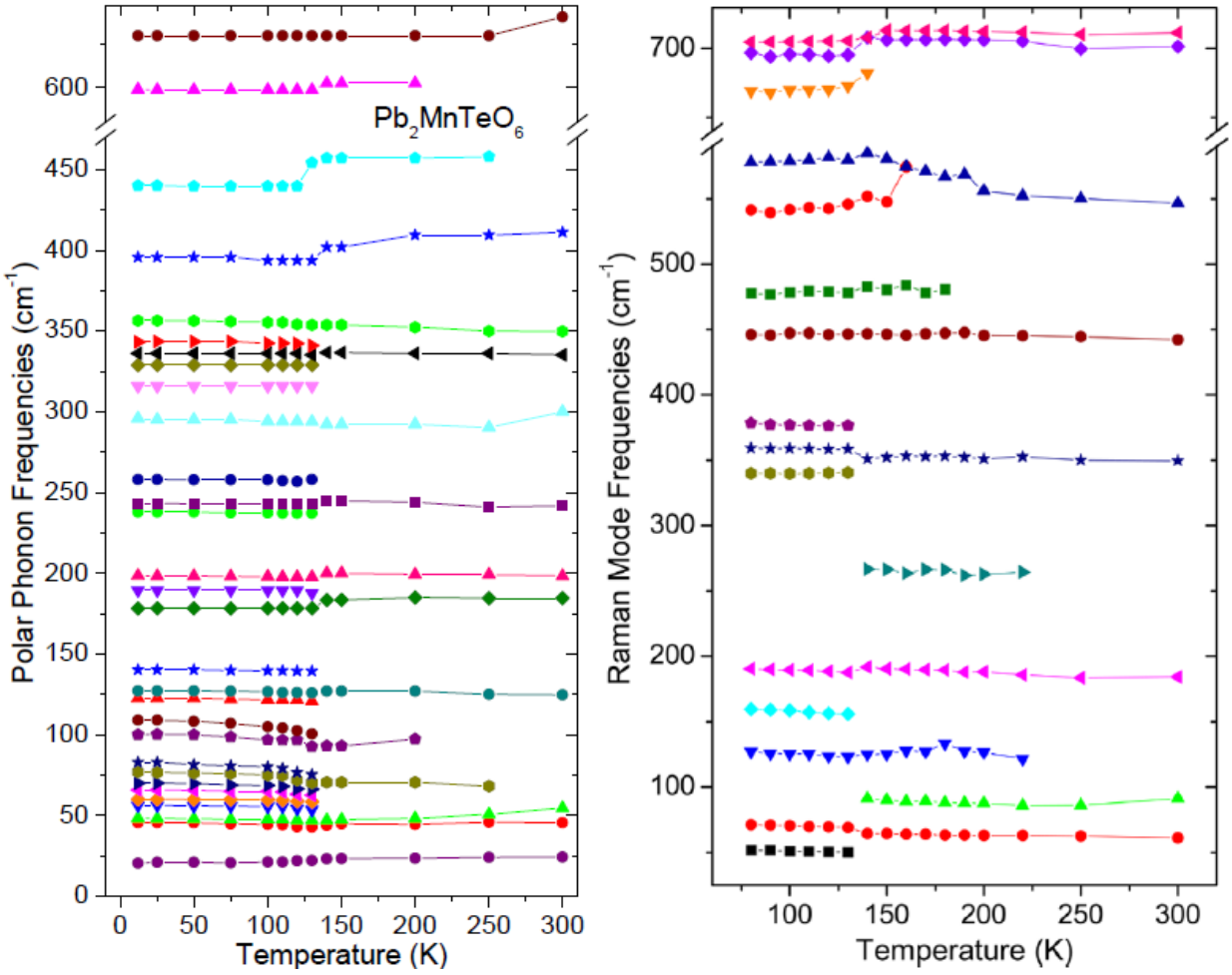

Figure 3.13 Temperature dependence of frequencies of (left) IR- and (right) Raman-active phonons obtained from the fit of IR reflectivity and Raman spectra respectively.

The missing modes can be explained by their weak intensity, by their overlapping with other strong modes, or by contributions of multiple differently oriented grains to the spectra, if the grain size is smaller than the laser-spot size (about 2 μm). The grain size of Pb_2MnTeO_6 is around 130-200 nm. More detailed Raman scattering experiments performed on Pb_2MnTeO_6 single crystals are required to resolve all allowed Raman-active modes.

Both Raman and IR spectra support a first order structural phase transition. Most of the phonons exhibit abrupt shifts and splitting at T_C. Changes of polar phonon frequencies and related changes of their dielectric strengths, due to Lyddane–Sachs–Teller relation, are responsible for the drop down of $\varepsilon'(T)$ below T_C. On the other hand, no soft mode activated from high-temperature BZ boundary due to multiplication of the unit cell was observed in the spectra below T_C. The latter indicates that the structural, and highly probable, antipolar phase transition is not driven by a soft phonon from the BZ boundary. Such soft phonons were observed in the Raman spectra of $SrTiO_3$ below its antiferrodistortive phase transition at 105 K.[230] Note as well that BZ-center phonon softening was observed near T_C in both IR and Raman spectra[226,231] of canonical AFE $PbZrO_3$, although no phonon softening was observed at the BZ boundary in this material.[232]

3.2.3.8 Density Functional Theory Calculations

Pb_2MnTeO_6 was relaxed in the expected high symmetry cubic $Fm\bar{3}m$ structure. The computed cubic $Fm\bar{3}m$ structure has a lattice constant for the conventional cell of 8.073 Å and the Mn-O bond lengths are 0.172 Å shorter than the Te-O bond lengths. We computed the phonons at the zone center and zone boundary points, showing that the cubic structure is unstable to polar distortions and to a variety of oxygen octahedron rotation patterns. *I*2/*m* symmetry is established by the addition of an $a^-a^-c^0$ octahedral rotation pattern to the cubic structure, and *C*2/*c* symmetry by the addition of an L_3^+ mode, which primarily corresponds to a complex pattern of oxygen octahedra rotations about the [001] cubic axis. The L_3^+ mode also allows the Pb ions to offcenter along the *b* axis in an antipolar ordering, accounting for most of the observed offcentering pattern. A small deviation of the Pb ions displacement from the *b* direction is from GM5+ mode – see the lattice distortion in *C2/c* structure in Figure 3.14. The *I*2/*m* and *C*2/*c* structures were relaxed with a variety of spin orderings on the Mn ions. The lowest energy magnetic ordering for each structure is the AFM ordering observed experimentally (Figure 3.8(right)). The relaxed AFM *C2/c* structure is our calculated ground state, in agreement with the experimental low temperature structure (the structural parameters of the relaxed *I*2/*m*

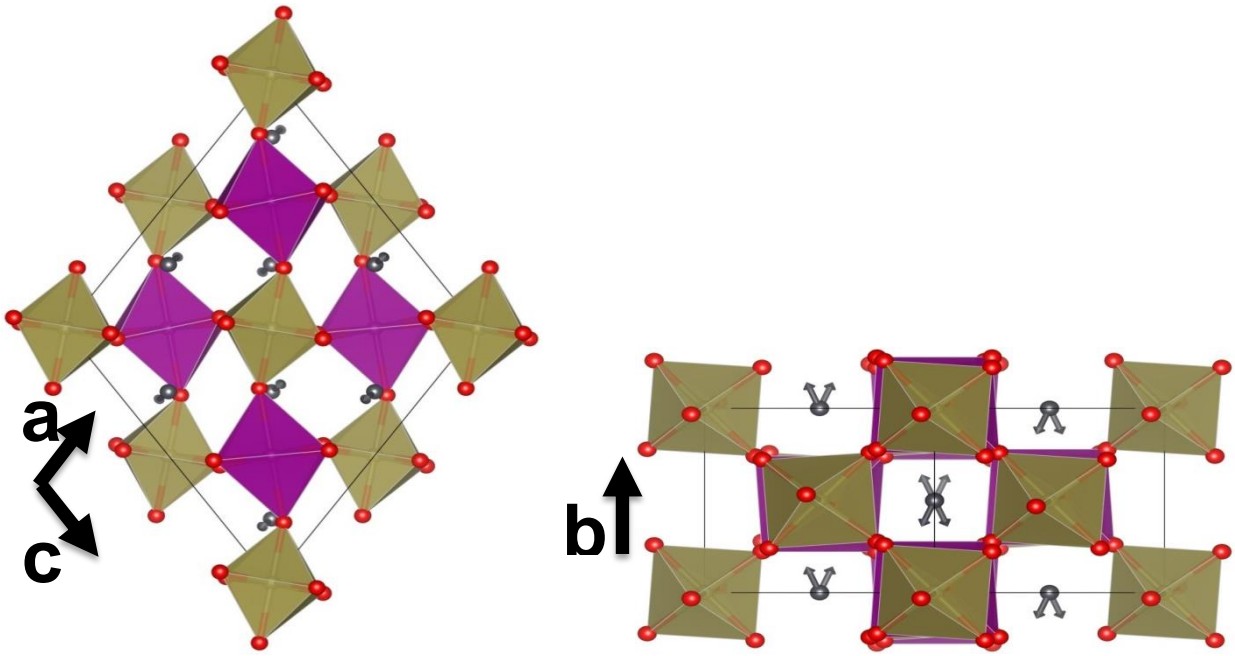

Figure 3.14 Antipolar C2/c structure from DFT calculations. Pb and oxygen atoms are shown in black and red, respectively. MnO_6 and TeO_6 octahedra are shaded in purple and brown, respectively. Pb atoms are shown at their high symmetry positions with arrows indicating the direction of their displacements in C2/c. (a) View down the [110] cubic direction. The octahedral rotations in the C2/c structure are clearly seen. (b) View down the [001] cubic direction. The complex rotation pattern about the [001] axis is evidenced. The motion of Pb along the b axis is set by the L3+ mode. The remainder of Pb ion motion is set by the GM5+ mode.

and *C*2/*c* structures are presented in Table S3 of SI of Ref. 143, showing excellent agreement with the structures of the phases experimentally observed at RT and 14 K, respectively).

The presence of an antipolar ordering of Pb cation displacements in the *C*2/*c* phase suggests the possibility of antiferroelectricity. To explore this, we searched for a low energy metastable polar structure that could be induced by an applied electric field.[233] First, we relaxed the structures obtained by freezing in the unstable polar mode along various directions ([100], [110] and [111]) leading to structures with 10 atoms/primitive cell and space groups *I*4*mm*, *Imm*2, and *R*3*m*, respectively. These structures are much higher in energy than the *C*2/*c* ground state. Furthermore, none of these polar structures are local minima of the energy – each has multiple instabilities corresponding to various octahedral rotation patterns. In each case, the addition of octahedral rotation distortions and further relaxation yields a nonpolar structure (detailed in Table 3 of Ref. 143), with the exception of *Imm*2 combined with $a^0a^0c^+$. In this case, the structure has $Pmn2_1$ symmetry, with a nonzero polarization along the [110] cubic direction, but is not a local minimum of the energy, exhibiting an instability corresponding to the $a^-a^-c^0$ rotation pattern. Relaxing this rotation pattern into the $Pmn2_1$ structure leads to the nonpolar $P2_1/n$ structure. While a low-energy metastable polar phase with a more complex structure is not ruled

out by our search, switching would require a change in the octahedral rotation pattern that would almost certainly result in a large switching barrier, and consequently a coercive field above the breakdown field. Therefore, we conclude that AFE switching is unlikely to be observed in Pb_2MnTeO_6.

3.2.4 **Conclusions**

We have successfully prepared the novel double perovskite Pb_2MnTeO_6. This compound exhibits a first-order phase transition from a room temperature *I2/m* structure to a low temperature (below ~120 K) *C2/c* structure.

The number of phonons observed in the IR and Raman spectra correspond to the number of phonons expected from the factor group analysis in both phases. Abrupt changes at T_C in both IR and Raman spectra confirm first-order character of the phase transition seen as well in thermal capacity and dielectric permittivity measurements. The low temperature phase is characterized by large displacements of the Pb atoms, forming a PbO_3E environment with shorter Pb–O bonds. This distortion induces off-centering of Mn^{2+} magnetic cations from the center of the octahedra. Due to this strong antiparallel displacement the possible AFE character of the compound was investigated, but no AFE loops were detected, which suggests that the structure is only antipolar.

First principles calculation confirms that AFE switching is unlikely to be observed in Pb_2MnTeO_6. Near 20 K, magnetic, heat capacity and PND studies revealed an AFM phase transition with a collinear AFM structure at low temperatures. Thus, Pb_2MnTeO_6 belongs to a rare group of antipolar antiferromagnets with a potential large magnetoelectric coupling.

3.3 Ni-based Tellurides

The last subchapter of the experimental results of the current thesis incorporates the investigation of dynamical magnetoelectric effect in the spin-induced multiferroic Ni_3TeO_6, followed by the examination of the role of Mn- and Co-doping in the multiferroic properties. The current section consists of four subsections: The first one is dedicated to the dynamical magnetoelectric coupling of Ni_3TeO_6, the second to the novel multiferroic Ni_2MnTeO_6, the third to the Co-doped Ni_3TeO_6 compounds Ni_2CoTeO_6 and $NiCo_2TeO_6$, and the last one covers a comparison among the counterparts of the $Ni_{3-x}B_xTeO_6$ (B=Mn, Co) family.

The table below summarizes the main findings of the forthcoming subchapter (previously reported studies on Ni_3TeO_6 are included for comparison). All compounds present the non-centrosymmetric *R*3 space group symmetry, AFM spin structure, and spin-flop transition. The critical temperatures of the temperature- and/or magnetic field-induced magnetic transitions vary among the compounds. Spin excitations were observed in all compounds. In addition to the pure magnons, Ni_3TeO_6 and $NiCo_2TeO_6$ also display electromagnons.

	Ni_3TeO_6	Ni_2MnTeO_6	Ni_2CoTeO_6	$NiCo_2TeO_6$
crystal symmetry	***R*3**[234]	***R*3**	***R*3**	***R*3**
T_N	**53 K**[63]	**73 K**	**55 K**	**52 K**
$H_{spin\text{-}flop}$	**8 T**[63]	**5 T**	**7 T**	**3 T**
magnons	**2**[144]	**2**	**4**	**6**
electromagnons	**2**[144]	**-**	**-**	**2**

3.3.1 **Magnetoelectric excitations in multiferroic Ni_3TeO_6**

The spin-order-induced FE antiferromagnet Ni_3TeO_6 transcends the magnetoelectric performance of all other single-phase multiferroics, because it exhibits non-hysteretic colossal magnetoelectric coupling.[63]

Spin and lattice excitations in Ni_3TeO_6 were investigated by a combination of IR, Raman and THz spectroscopies. Two spin excitations (near 13 and 35 cm^{-1}) were observed simultaneously in Raman and time-domain THz spectra below the Néel temperature T_N=53 K. We propose to assign them to electromagnons, which are activated by the dynamic magnetoelectric coupling. A third magnon is seen only in the Raman spectra near 206 cm^{-1}.

The figure below previews the two electromagnons observed in Ni_3TeO_6 by THz and Raman spectroscopies, as published in Ref. 144.

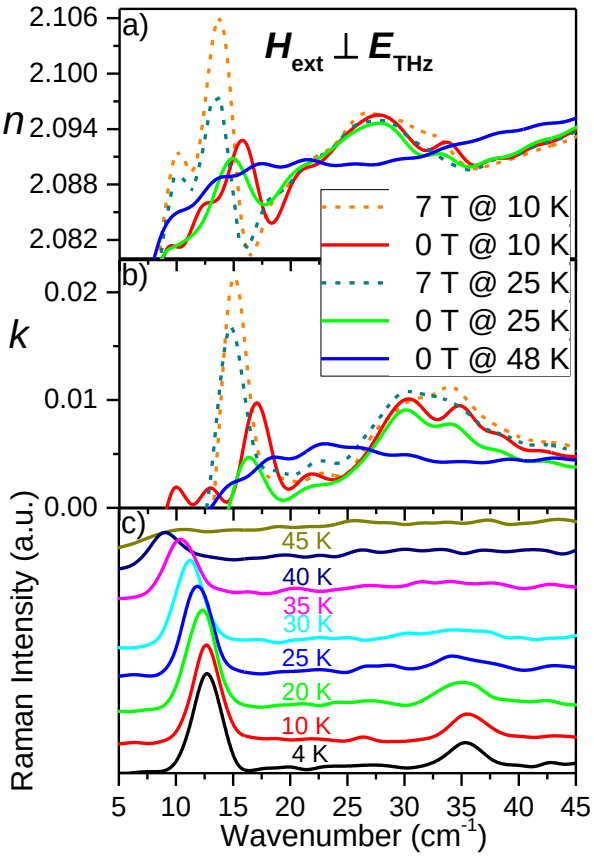

3.3.1.1 Introduction

The high demands for energy and cost efficiency of the technological world have led to the necessity of multifunctional devices. Magnetoelectric multiferroics are strong candidates for such novel applications owing to the potential use of electrical field to tune their magnetic properties.[1,2]

However, only a few single-phase multiferroics manifest a strong magnetoelectric coupling[63,235–238] and all those materials are type-II multiferroics, where the FE polarization is spin-order-induced.[63,70,235–237] Among them, only Ni_3TeO_6 exhibits a non-hysteretic colossal magnetoelectric effect. However, this occurs only at magnetic fields near 8.5 T[63] and 53 T,[239] where spin-flop and metamagnetic phase transitions occur, respectively. The absence of hysteretic behavior in the magnetic-field dependence of magnetization and FE polarization precludes losses, which is highly promising for a number of magnetoelectric applications.

At room temperature, Ni_3TeO_6 has a corundum-related structure with the polar R3 space group.[234,240] A collinear AFM order appears below T_N = 53 K,[241] giving rise to a spin-induced FE ordering (Figure 3.15).[63] The previous report of a FE phase transition at 1000 K[242] is questionable, because the reported dielectric dispersion is typical of the Maxwell-Wagner relaxation in conducting systems,[225] and no switchable FE polarization has been observed above 53 K. Lattice dynamics of Ni_3TeO_6 were investigated above 150 cm^{-1} using IR spectroscopy as a function of temperature and magnetic field.[243] Phonon anomalies due to spin-phonon coupling were observed near T_N and a spin-flop transition close to 9 T, but also near 30 T, which suggest another magnetic phase transition at 30 T.[243] In addition, interlocked chiral and polar domain walls were observed at room temperature, unveiling a complex coupling between the chiral and polar order parameters.[244]

Due to sum rules, the static magnetoelectric coupling should be governed by magnetoelectric excitations (electromagnons) in the GHz and/or THz regions.[245] These spin excitations can contribute to the dynamic magnetoelectric coupling between the magnetic permeability and dielectric permittivity, and if the magnetic structure is sensitive to the static magnetic or electric field, the electromagnons can be tuned by these fields.[82,246] The possibility to modulate the index of refraction could promote the design of novel optoelectronic devices. Since electromagnons very often lie in the THz range of the electromagnetic spectrum, THz spectroscopy is an essential tool for detecting such excitations.

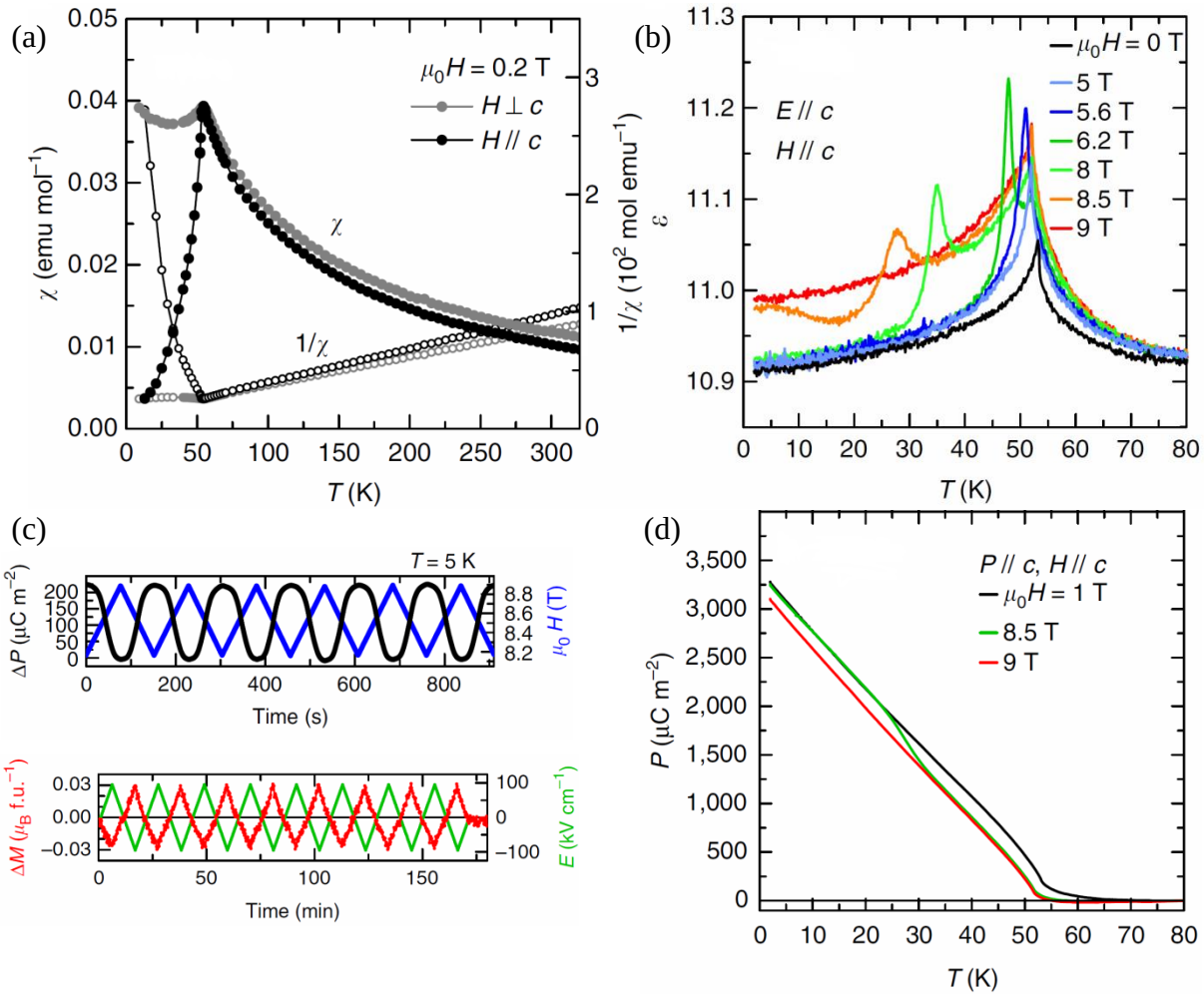

Figure 3.15 (a) Antiferromagnetic phase transition occurring at 53 K, as seen from susceptibility measurements. (b) Magnetic field evolution of the dielectric anomaly. (c) Colossal magnetoelectric coupling at the vicinity of the spin-flop transition, ~8 T. (d) Spin-induced polarization, reaching ~3,000 μC/m^2 below 5 K.[63]

However, a combination of spectroscopic techniques are required to account for the nature of the detected excitations, since the spin excitations can be pure magnons (contributing only to the magnetic permeability μ) or electromagnons (contributing also to the permittivity ε^*). Polarized THz or IR spectroscopy of single crystals is commonly used for distinguishing between magnons and electromagnons,[5,239,245] but, to this aim, all possible polarized spectra or the directional dichroism should be measured. Such experiments require relatively large single crystals with dimensions of the order of several millimeters, which are often unavailable. Since each polar excitation should be both IR and Raman active in a non-centrosymmetric FE phase,[142] the combination of both these techniques can be used for identifying the electromagnons even in polycrystalline samples.

In that fashion, we studied Ni_3TeO_6 single crystals and ceramics by Fourier-Transform IR, Raman and time-domain THz spectroscopies, in a temperature range between 4 and 300 K. We show that Ni_3TeO_6 exhibits dynamic magnetoelectric coupling, inducing at least 2 excitations simultaneously detected by Raman and THz spectroscopy, interpreted as electromagnons.

3.3.1.2 Experimental Details

Ni_3TeO_6 was prepared as polycrystalline powders and single crystals. Green Ni_3TeO_6 powders were synthesized by solid state methods from stoichiometric amounts of analytical-grade NiO and TeO_2, and heating the mixture at 800 ºC for 12 hours in O_2 flow. The single crystals were grown from a flux composed of the previously prepared powders of Ni_3TeO_6, V_2O_5, TeO_2, NaCl and KCl in a molar ratio of 1:5:10:10:5. The mixture was heated for three days at 830ºC and then cooled down to 600ºC during five days. Plate-shaped green single crystals ~2 mm in diameter and with thickness 60-100 μm were obtained.

The experimental details of IR reflectivity, Raman and time-domain THz spectroscopies used for the study of spin and lattice excitations were according to Chapter 2.

3.3.1.3 Results

Lattice excitations in Ni_3TeO_6

The IR reflectivity spectra of the Ni_3TeO_6 ceramics for selected temperatures from 7 to 300 K are shown in Figure 3.16(a). We present the spectra only from 150 cm^{-1}, because other weak excitations are seen only below 40 cm^{-1} and these are better resolved in the THz spectra, which will be discussed below. As predicted by the factor group analysis for the crystal structure with *R*3 symmetry,[234,240] 9 $E(x,y,x^2-y^2,xy,xz,yz)$ and 9 $A(x^2+y^2,z^2,z)$ modes are expected, both IR and Raman active.[243] All 18 modes can be seen in the IR spectra up to 300 K.

No significant changes in phonon eigenfrequencies and/or respective damping are observable as a function of temperature, apart from the expected decrease on damping upon cooling. The spectra reveal similar mode frequencies as the previously studied Ni_3TeO_6,[243] with 10 of the modes seen above 360 cm^{-1} corresponding to the vibrations of the TeO_6 octahedra.[247] Since there is no change of crystal symmetry at the AFM phase transition, no change in phonon selection rules is expected. The phonon parameters obtained from the IR spectra fits are listed in Table 3.2, together with the frequencies reported by Yokosuk et al.[243] and with phonon frequencies obtained from our polarized Raman spectra of the single crystal.

The complex permittivity calculated from IR spectra fits is presented in Figure 3.16(b) and (c). One can notice that the static permittivity $\varepsilon(0)$ attains a value of ca. 4.5 only, which is common among the spin-induced FEs. The difference between our static permittivity and its value of nearly 11 observed in the radio-frequency region by Oh *et al.*[63] could be explained by the high porosity of our ceramics (about 58%).

In the inset of Figure 3.16(b), the mode around 310 cm^{-1} shows a remarkable increase in intensity upon cooling towards 40 K due to a decrease in phonon damping, accompanied by a slight hardening. Below $T_N \approx 53$ K, the same phonon exhibits a small decrease in intensity. Since the structure displays no anomaly at T_N, this is probably linked to the transfer of its dielectric strength to a lower-energy spin excitation appearing in the THz spectra in the AFM phase. The anomalous temperature behavior of this mode was reported already by Yokosuk *et al.*,[243] who observed its hardening by 2.5 cm^{-1} on cooling down to T_N and its softening below T_N, which they explained by spin-phonon coupling.

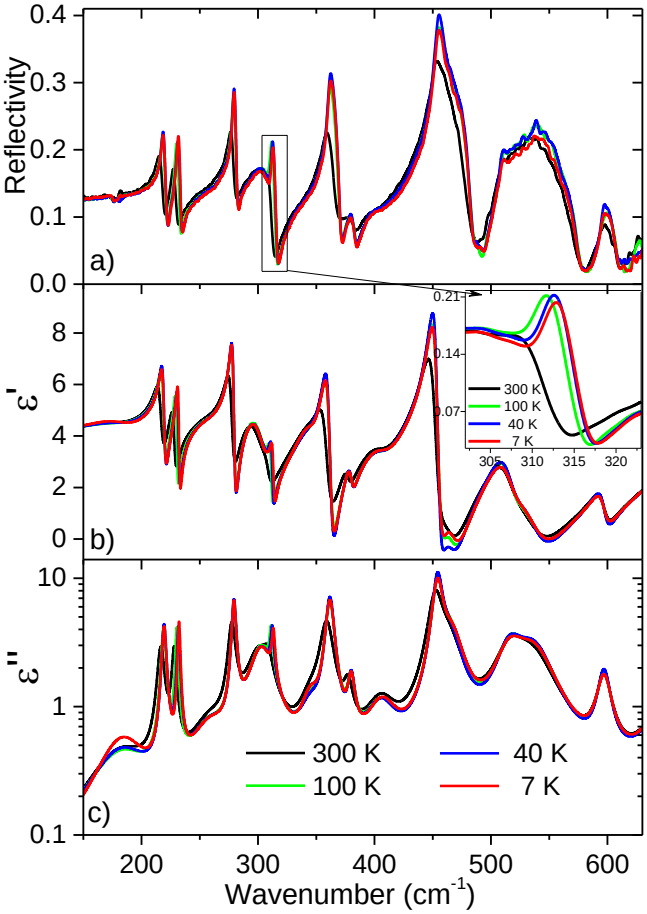

Figure 3.16 (a) Experimental IR reflectivity spectra of Ni_3TeO_6 ceramics at selected temperatures from 7 to 300 K. (b) Real and (c) imaginary parts of permittivity, as obtained from the fits. Inset: Temperature dependence of IR reflectivity of the mode around 310 cm^{-1} showing, on cooling, a marked decrease in its damping, accompanied by a frequency increase (hardening).

We measured polarized Raman back-scattering spectra of the Ni_3TeO_6 single crystals in all possible polarization configurations and at temperatures from 4 to 300 K. Raman spectra measured in four polarization configurations at 4 K are shown in Figure 3.17. The temperature dependence of the cross-polarized $z(xy)\bar{z}$ Raman spectra (according to the Porto notation)[248] can be seen in Figure 3.18, where 13 phonons were observed.

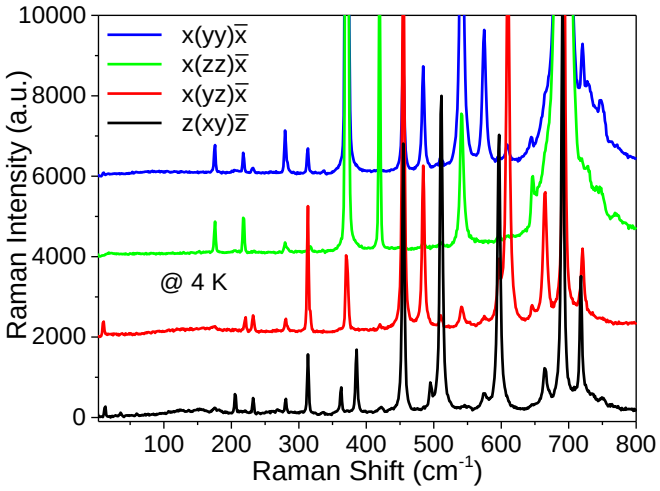

Figure 3.17 Raman spectra of the Ni_3TeO_6 single crystal collected at different polarization configurations at 4 K.

In the notation followed in this paper *x*, *y* and *z* directions are mutually perpendicular; z direction is parallel to the hexagonal *c*-axis, while *x* and *y* directions are lying in the *ab*-plane. The combination of $x(zz)\bar{x}$ and $z(xy)\,\bar{z}$ spectra reveals all 18 predicted modes. The eigenfrequencies of different configurations ($x(yy)\,\bar{x}$, $x(yz)\,\bar{x}$, $x(zz)\,\bar{x}$ and $z(xy)\,\bar{z}$), together with the respective symmetry assignment, are listed in Table 3.2, which provides their comparison with the polar phonon frequencies obtained from our IR spectra. The frequencies of Raman and IR modes correspond to each other, confirming the prediction of the factor group analysis that these modes should have the same symmetry. Five *A(LO)*-symmetry modes near 179, 385, 495, 691 and 720 cm^{-1}, which are allowed in $z(xx)\bar{z}$ spectra, appear as well in the $z(xy)\bar{z}$ spectra (*E* symmetry), possibly due to polarization leakage. Such mode mixing could be attributed to sample misalignment, crystal imperfections or depolarization effect.[249–251] Finally, two modes observed in the IR spectra were not seen in any of the Raman spectra.

Below 210 cm^{-1}, in the AFM phase, a number of new modes are activated in the $z(xy)\bar{z}$ Raman spectra (Figure 3.18). Among them, the mode near 206 cm^{-1} becomes very sharp and intense on cooling, whereas the mode activated on the low-frequency edge of our spectra at 9.9 cm^{-1} (40 K) hardens on cooling to 12.7 cm^{-1} (4 K). These modes, together with other ones resolved below 200 cm^{-1}, cannot be new phonons, because the space group R3 does not change below T_N. These must be spin excitations. This conclusion will be confirmed below, because two modes seen below 40 cm^{-1} in the THz transmission spectra are highly sensitive to external magnetic field. Lastly, the weak modes between 130 and 190 cm^{-1} originate probably in multimagnon scattering.

Electromagnons in Ni_3TeO_6

In order to investigate the far-IR domain, we measured time-domain THz spectra of Ni_3TeO_6 ceramics (crystals were too small) in a temperature range from 10 to 300 K in an external magnetic field $\boldsymbol{H}_{ext}$ up to 7 T. The THz spectra for selected temperatures and magnetic fields are shown in Figure 3.19. Both configurations with $\boldsymbol{H}_{ext} \parallel \boldsymbol{E}_{THz}$ and $\boldsymbol{H}_{ext} \perp \boldsymbol{E}_{THz}$ were measured, and both orientations reveal similar features. Here we present only the latter spectra.

The THz spectra were fitted together with the IR ones, according to the model mentioned above. Two spin excitations are clearly seen in both real and imaginary parts of the refractive index spectra, corresponding to frequencies of approximately 16 and 32 cm^{-1}, at 7 K (see Table 3.2). These two modes are not active above T_N. Upon cooling, one weak and broad excitation appears at 48 K near 25 cm^{-1} and hardens to 32 cm^{-1}. Another sharp mode activates near 16 cm^{-1}. This excitation markedly softens with $\boldsymbol{H}_{ext}$ (Figure 3.19). Unfortunately, we could use magnetic field only up to 7 T, so we could not see the influence of the spin flop transition occurring at approximately 8 T on the mode frequencies. The second mode seen near 32 cm^{-1} seems to exhibit splitting upon applying $\boldsymbol{H}_{ext}$, but it is not well resolved, because the sample is polycrystalline. Since both excitations activate only below T_N and their frequencies are sensitive to magnetic field, these must be spin excitations.

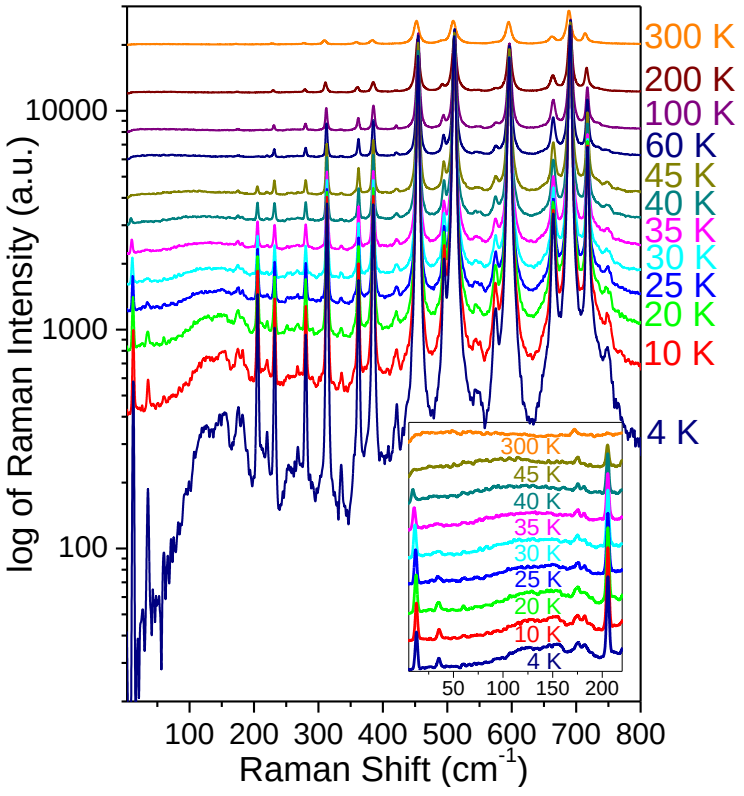

Figure 3.18 Temperature dependence of $z(xy)\bar{z}$ Raman spectra of the Ni_3TeO_6 single crystal. Inset: Detail of the lower spectral range, where the two spin excitation modes around 12 and 35 cm^{-1} appear below 45 K, and harden upon cooling. The activation of other modes up to 206 cm^{-1} is discussed in the text.

Table 3.2.Frequencies of the IR active modes in the Ni_3TeO_6 ceramics at 7 K and Raman active modes in Ni_3TeO_6 single crystal at 4 K, as obtained by the fits of IR reflectivity with ε_∞ =2.2. The first column corresponds to the IR mode frequencies (300 K) from Yokosuk *et al.*[243] Apart from the frequency, we list the damping constants and dielectric strength of the IR-active modes. The LO modes observed in Raman spectra are marked by + in superscript.

		Raman 4 K				IR 7 K		
ω_{TO} [243]	Symmetry	$x(yy)\bar{x}$ $\omega_{TO}(cm^{-1})$	$x(yz)\bar{x}$ $\omega_{TO}(cm^{-1})$	$x(zz)\bar{x}$ $\omega_{TO}(cm^{-1})$	$z(xy)\bar{z}$ $\omega_{TO}(cm^{-1})$	$\omega_{TO}(cm^{-1})$	$\gamma_{TO}(cm^{-1})$	$\Delta\varepsilon$
–	electromagnon		10.5		12.7	16.2	2.1	0.004
–	electromagnon				35.3	32.4	8.3	0.007
171	*A*	176.0		176.0	179.4^+	185.0	46.4	0.12
–	(electro)magnon				205.6			
214	*A*	217.5		217.5		219.3	4.4	0.08
217	*E*		220.6		220.5			
228	*E*				232.0	232.1	2.6	0.05
–						259.2	37.0	0.07
278	*E*				280.4	279.3	4.2	0.09
278	A	279.6		279.7		303.1	24.2	0.21
310	*E*	313.5	313.4		313.2	313.2	3.1	0.02
–	*A*			317.0		345.2	17.8	0.04
360	*E*				362.2	361.7	8.3	0.14
370	*A*	370.0		370.0		380.0	6.7	0.02
–					385.1^+			
451	*A*			419.1		406.6	30.0	0.06
456	*E*	454.7	454.9		454.5	454.2	10.0	0.18
–		484.3^+	484.5^+		494.8^+	466.1	23.2	0.15
513	*E*		510.7		510.7	516.5	27.4	0.11
541	*A*	540.9	541.8	542.0		536.6	41.3	0.18
597	*E*	574.8^+	609.5^+		596.1	597.1	13.7	0.03
649	*A*			646.9				
666	*E*		664.9		664.0	661.2	25.0	0.10
692	*A*	693.0	693.0	693.0	690.5^+	690.5	45.4	0.06
–			720.4^+		717.7^+			

In order to compare the results of the two distinct spectroscopic techniques, we present in Figure 3.19(c) the Raman spectra in the low-frequency region at temperatures up to 45 K. The frequencies of the two spin excitations in Raman spectra are approximately 13 and 35 cm^{-1} in the single crystal, whereas those observed in the ceramics by time-domain THz experiments amount to 16 and 32 cm^{-1}. If we take into account the different crystallinity of the samples, such discrepancies lie within the experimental error, therefore we assert that both experiments reveal the same pair of excitations and we propose that these are electromagnons. Magnons are usually extremely weak in Raman spectra, but if a magnon becomes electrically active, it can be stronger and it should follow the same IR and Raman selection rules in polar crystal structure.[22] Since the electromagnons are active in *xy* Raman spectra, they must have *E* symmetry.

Below T_N, another sharp and strong excitation activates in $z(xy)\bar{z}$ Raman spectra at 206 cm^{-1} (Figure 3.18). It probably also has a spin origin and, because it has *E* symmetry, it could also be an electromagnon. Nevertheless, this mode is resolved in neither our nor previous[16] IR studies, so we cannot confirm its polar character.

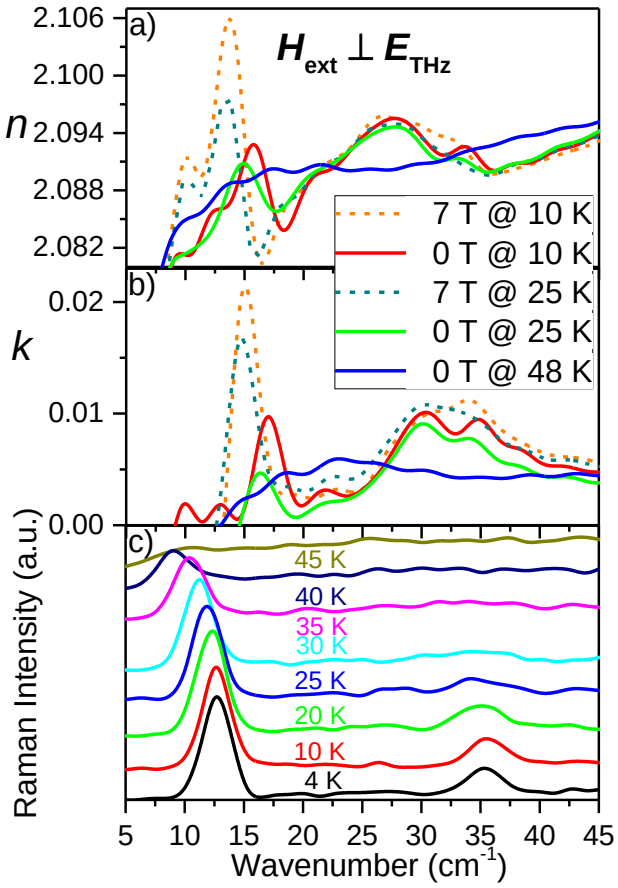

Figure 3.19 Temperature dependence of (a) real and (b) imaginary part of index of refraction, as obtained by the THz measurements at $\boldsymbol{H}_{ext} \perp \boldsymbol{E}_{THz}$ for the Ni_3TeO_6 ceramics. Two excitations appear below 48 K (close to $T_N \approx 53$ K). Upon application of $\boldsymbol{H}_{ext}$ up to 7 T, softening of the lowest frequency mode is observed. (c) Temperature evolution of $z(xy)\bar{z}$ Raman spectra of the Ni_3TeO_6 single crystal below 45 K.

3.3.1.4 Discussion

Ni_3TeO_6 has a polar $R3$ structure at least up to 1000 K,[225] and its non-switchable polarization must be, due to the space group symmetry, oriented along the c axis. Below T_N, the exchange striction ($\propto \mathbf{S}_i \cdot \mathbf{S}_j$) between collinear spins of Ni cations changes the bond lengths between these atoms.[238] The question arises whether Ni_3TeO_6 is truly FE, or rather merely pyroelectric with a spontaneous polarization which is just influenced by the magnetic order. The second scenario is also supported by the experimental fact that the external magnetic field *reduces* the spontaneous polarization and this polarization change is most remarkable at the spin flop transition near 9 T.[238]

Our electromagnons have the E symmetry, because they are active in the $x(zz)\bar{x}$ and $z(xy)\bar{z}$ polarized Raman spectra, and therefore they must be IR active in the $E \perp z$ spectra. Since the spontaneous static polarization is oriented along z axis and the electromagnons are polarized perpendicularly to this direction, the spin excitations become electrically active due to dynamic

fluctuations of spins (and the related polarization) out of the *z* axis. This dynamic polarization can be induced by the same exchange striction mechanism as the static polarization. Generally, electromagnons must receive their dielectric strength from polar phonons of the same symmetry. In Ni_3TeO_6 Yokosuk et al.[243] observed 3 IR-active phonons of *E* symmetry (at 310, 597 and 668 cm^{-1}) exhibiting anomalies at T_N, while no *A*-symmetry phonon exhibited any anomaly at the AFM phase transition. As discussed earlier, we observed frequency hardening and an intense decrease in the damping of the 310 cm^{-1} mode on cooling, however, no trace of anomaly was seen for the higher frequency modes (597 and 668 cm^{-1}). Therefore, the electromagnons are coupled with the *E*-symmetry phonon near 310 cm^{-1}. The above-mentioned anomalous *E* phonons are related to stretching or bending of the octahedral cages of TeO_6 and NiO_6 inducing a further modulation of the superexchange interaction between the Ni ions along the *c*-axis.[243]

Even though polycrystalline ceramic samples were used for the THz experiments, the electromagnons are still reasonably sharp. Unfortunately, the size of the single-crystalline samples (≤ 1 mm diameter) was not sufficient for the IR and THz spectroscopies, since large and well-polished surfaces are needed for these techniques. Studying oriented single-crystalline samples by THz spectroscopy would help to confirm the *E*-symmetry and polar character of the electromagnons, and the possible directional dichroism could be investigated. In addition, splitting of electromagnons in an external magnetic field might be observed.

One can argue that the dielectric strengths of the electromagnons should enhance ε' below T_C, however such behavior was not observed in the temperature dependence of ε' reported in Ref. 63. This is due to the small dielectric strength of both electromagnons ($\Delta\varepsilon_1 + \Delta\varepsilon_2 = 0.011$ at 7 K – see Table 3.2). Such small contribution cannot be resolved in $\varepsilon'(T)$. Note that $\varepsilon'(T)$ exhibits only small peak in permittivity at T_C ($\Delta\varepsilon = 0.15$), and this dielectric anomaly can be caused by a softening of the electromagnons down to microwave range near T_C. Similar effect was recently observed in the multiferroic $MnWO_4$ by Niermann *et al.*.[252]

Lastly, we performed Raman studies of the Ni_3TeO_6 single crystal in an external electrical field parallel to the *c*-axis (up to 60 kV/cm), in order to investigate the behavior of the electromagnons on external bias. However, no significant effect was observed. Bad quality of contact electrodes, non-uniformly applied electrical field and/or defects in the crystal may have hindered our efforts for such observation.

3.3.1.5 Conclusions

To conclude, we studied the dynamic magnetoelectric coupling in the multiferroic Ni_3TeO_6 by a combination of IR, Raman and time-domain THz spectroscopic techniques. A thorough investigation of lattice and spin excitations was conducted by Raman spectroscopy of single crystals, measuring all possible polarization configurations, and reported for the first time in literature.

At least two spin excitations around 15±2 cm^{-1} and 35 cm^{-1} appear simultaneously in the AFM phase in both THz and Raman spectra, thus corresponding to electromagnons. The lowest-frequency electromagnon displays a strong sensitivity to external magnetic field, by increasing its intensity and decreasing its frequency. Another sharp excitation appears below T_N near 206 cm^{-1}. Since it is not resolved in unpolarized IR reflectivity spectra of ceramics, we assume it is a magnon. Nevertheless, we cannot exclude that it is also an electromagnon, which would be screened by a stronger *A*-symmetry polar phonon near 219 cm^{-1}.

Further studies of Ni_3TeO_6 single crystals by polarized time-domain THz spectroscopy are required for a detailed polarization analysis of electromagnons, a possible detection of a directional dichroism, and for determining the dependence of the electromagnon frequency on the external magnetic field strength (including a possible splitting). A better understanding of the electromagnonic behavior can lead to a deeper insight into the mechanisms of dynamic magnetoelectric coupling in multiferroics.

3.3.2 **The novel multiferroic Ni_2MnTeO_6**

In section 3.3.1, we saw the impressive colossal magnetoelectric effect of the polar anti-ferromagnet Ni_3TeO_6,[63] in combination with the presence of elementary magnetoelectric excitations.[144] Aiming at higher critical temperatures, immensely convenient for applications, one can consider substitution of Ni by other transition metals.

In the current, as well as the next section, we will see the effect of Ni substitution by Mn and Co, however keeping the same polar crystal structure with *R*3 space-group. Here, the novel compound Ni_2MnTeO_6 is presented. An AFM phase transition takes place at approximately 73 K, almost 20 K higher than the counter-compounds. THz spectra revealed one new excitation below T_N, which is tuned by external magnetic field, thus assigned as a magnon.

The impressive increase of the T_N by Mn-doping is displayed in the figure below, in comparison with the Co-doped compounds, by the temperature dependence measurements of magnetization and permittivity. Traces of a lower temperature phase transition at 23 K suggest the presence of Mn_3TeO_6.

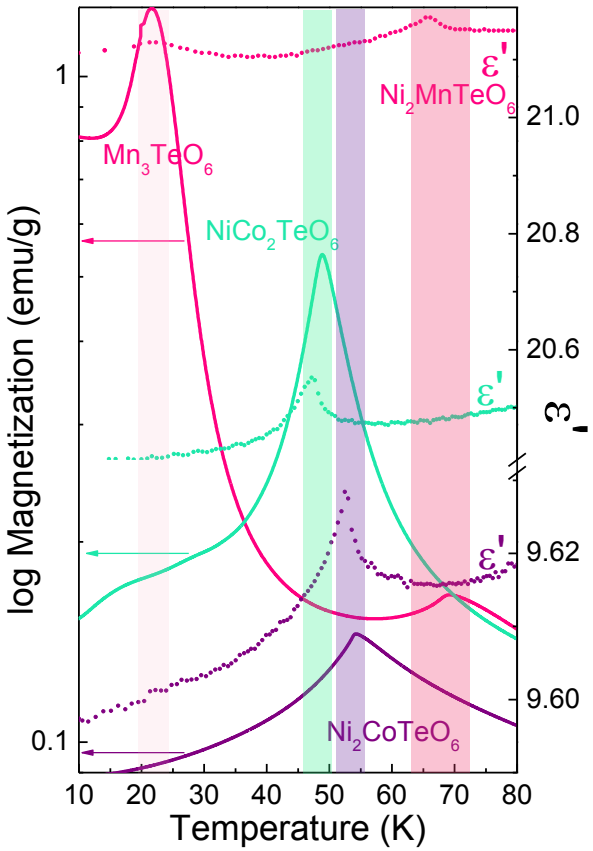

3.3.2.1 Introduction

In pursuit of multiferroic compounds with crystal structure other than that of the perovskites, the corundum-related (Al_2O_3) family with structural formula A_3BO_6, with A being a divalent or trivalent paramagnetic cation, and B a pentavalent or hexavalent (usually) diamagnetic cation, scores a success among the magnetic,[242,253–260] and lately, due to Ni_3TeO_6, the multiferroic community.[63,144,239,244]

During the 80s, a few studies on corundum- and cryolite-related (a-Na_3AlF_6) compounds suggested FE properties for a series of M_3TeO_6 compounds, with M corresponding to paramagnetic cations, and the reported Curie points lied around 500 K.[253,254] However, no evidence of non-centrosymmetric structure for any of the above compounds at room temperature was reported ever since, apart from Ni_3TeO_6. Mg_3TeO_6 and Mn_3TeO_6 correspond to a rhombohedral $R\bar{3}$ space group, Cd_3TeO_6 and Ca_3TeO_6 to monoclinic $P2_1/n$, Co_3TeO_6 to monoclinic $C2/c$, and Cu_3TeO_6 to cubic $Ia\bar{3}$. To this point, the only compounds in literature that present non-centrosymmetricity are Ni_3TeO_6 and $(Mn_{0.2}Ni_{0.8})_3TeO_6$ (Ni substitution with 20% Mn).[260] The latter compound preserves the non-centrosymmetric $R3$ space group, and interestingly enough, displays higher AFM transition temperature T_N=67 K. The phase diagram of the Mn-doped M_3TeO_6 structures with M=Ni, Co, Cu is shown in Figure 3.20, where the respective space groups and AFM transition temperatures T_N for each composition are indicated. The diagram suggests that by increasing the Mn concentration in the $Ni_{3-x}Mn_xTeO_6$ compound, and considering stabilization of the $R3$ space group, T_N is expected to continue increasing.

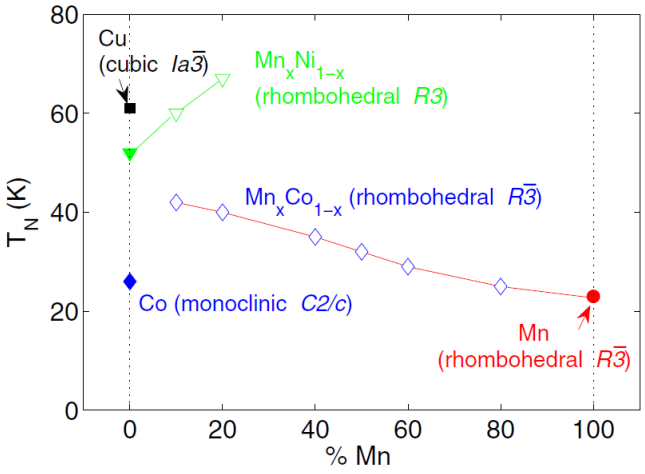

Figure 3.20 Phase diagram for M_3TeO_6 compounds, with M=Ni, Co, Cu, as a function of Mn doping. The only non-centrosymmetric branch of the diagram (both above and below T_N) corresponds to Ni_3TeO_6, and subsequent substitutions of Ni with Mn, up to 20%, accompanied by striking increase of the AFM transition temperature, from 52 to 67 K. (image taken from Ref. 260)

In that fashion, the novel Ni_2MnTeO_6 was synthesized for the first time. The magnetic and dielectric properties of Ni_2MnTeO_6 in the form of single crystals and ceramics were studied, together with the investigation of lattice and spin dynamics. The prediction on the increase of T_N for Mn-doped Ni_3TeO_6 by Mathieu *et al.*[260] is confirmed, since Ni_2MnTeO_6 exhibits AFM transition at 73 K. In addition, THz spectra unveil a spin excitation below T_N.

3.3.2.2 Experimental Section

The samples were synthesized by the co-authors of Ref. 144, from Rutgers University. Polycrystalline Ni_2MnTeO_6 was prepared from stoichiometric amounts of analytical grade NiO, TeO_2 and $MnCO_3$. The mixture of the starting materials was heated in a tubular furnace under oxygen flux at 800ºC with intermediate grindings between 700 and 800ºC. Single crystals were prepared in a following step by flux method: Ni_2MnTeO_6: V_2O_5: TeO_2: NaCl: KCl in a molar ratio of 1:5:10:10:5. The mixture was kept two days at 800ºC and then cooled down to 600ºC during three days. Plate shaped green crystals of 1-2 mm of diameter were obtained. To identify the phase and purity of the polycrystalline powders the sample was characterized by powder X-ray diffraction (XRD) (Cu Kα, λ= 1.5406 Å). For the structural refinements powder neutron diffraction (PND) and synchrotron X-ray diffraction (SXRD) were performed. PND was collected at the ILL, Grenoble. The data at room temperature (RT) was collected in the High Resolution instrument, D2B (λ= 1.5940 Å). For the determination of the magnetic structure we used D20 (λ= 2.410 Å) instrument between 5 and 100 K. SXRD data were collected on beam line X-16C (λ= 0.70019 Å) at the Brookhaven National Synchrotron Light Source (NSLS) at RT. Diffraction data analysis and Rietveld refinements[209] were performed with the Fullprof software[210] and TOPAS package.[211] The structure of the single crystals was determined by the use of single-crystal X-ray data (SCD) collected on a Bruker Smart APEX CCD diffractometer with graphite monochromatized Mo K_α radiation (λ= 0.71073Å) at 100 K. The structural characterization data will not be presented in the current thesis. Magnetic measurements for Ni_2MnTeO_6 single crystal were performed on a Quantum Design SQUID system, whereas for polycrystalline Ni_2MnTeO_6 on ACMS and VSM options (extraction and vibrating sample magnetometers) of the PPMS apparatus (Quantum Design) in fields up to 14 T and temperatures down to 2 K.

The IR reflectivity and THz complex permittivity spectra were fitted assuming a sum of N independent three-parameter damped harmonic oscillators (see section 2.1.2.1, equation 2.11).

3.3.2.3 Results

Structural Characterization

Based on the RT PND characterization (the structural analysis data will not be presented in the current thesis for brevity purposes), Ni_2MnTeO_6 was defined with Ni_3TeO_6 structural type (rhombohedral, space group of *R*3 (No. 146), Z = 3); as a $A_2BB'O_6$-type corundum derivative. The structure contains two crystallographically distinct Ni atoms at the A-sites, defined here as Ni^{I} and Ni^{II}, ordered Mn and Te on both B sites, and two independent oxygen atoms. The structure is formed by layers in the *ab* plane of edge sharing octahedra. The layers are formed by TeO_6 and $Ni^{I}O_6$ octahedra, and MnO_6 and $Ni^{II}O_6$ octahedra, alternated between them. The layers are connected along *c* forming $TeO_6/Ni^{II}O_6$ and $MnO_6/Ni^{I}O_6$ dimers that share faces.

Due to electrostatic repulsions, the cations inside the octahedra that are sharing faces are displaced from the center of the octahedra along the *c* direction, getting in all cases closer to the octahedra vacancies and farther away to the other cation in the dimer. It produces three long and three short octahedra distances. This effect is more pronounced in the case of Ni_2MnTeO_6 than Ni_3TeO_6.[234] The same effect has been observed in similar compounds as Mn_2FeWO_6 with the same structure.[261]

Magnetic Structure

PND was performed at low temperatures in order to determine the magnetic structure. The thermal evolution of the PND and the evolution of the volume and magnetic moments with the temperature are illustrated in Figure 3.21(a) and (b). By PND, the magnetic transition at 73 K is clearly seen (Figure 3.21(c)), 20 K higher than pure Ni_3TeO_6. The magnetic structure is defined as an AFM structure with propagation vector k=(0 0 3/2). The structure is formed by FM *ab*-planes coupled antiferromagnetically along *c*-axis as FM-FM-AFM-AFM, as illustrated in Figure 3.21(d). The magnetic moments at Ni^{I}, Ni^{II} and Mn positions have been refined at 5 K as $2.7\mu_B$/mol for both Ni positions and $2.8\mu_B$/mol for Mn respectively (Ni^{I} and Ni^{II} moments have been constrained). The moments over Ni positions are larger than the ones expected for Ni^{2+} spin state S=1, but it can be explained by the disorder with Mn^{2+}, which is expected to be in a spin state of S=5/2.

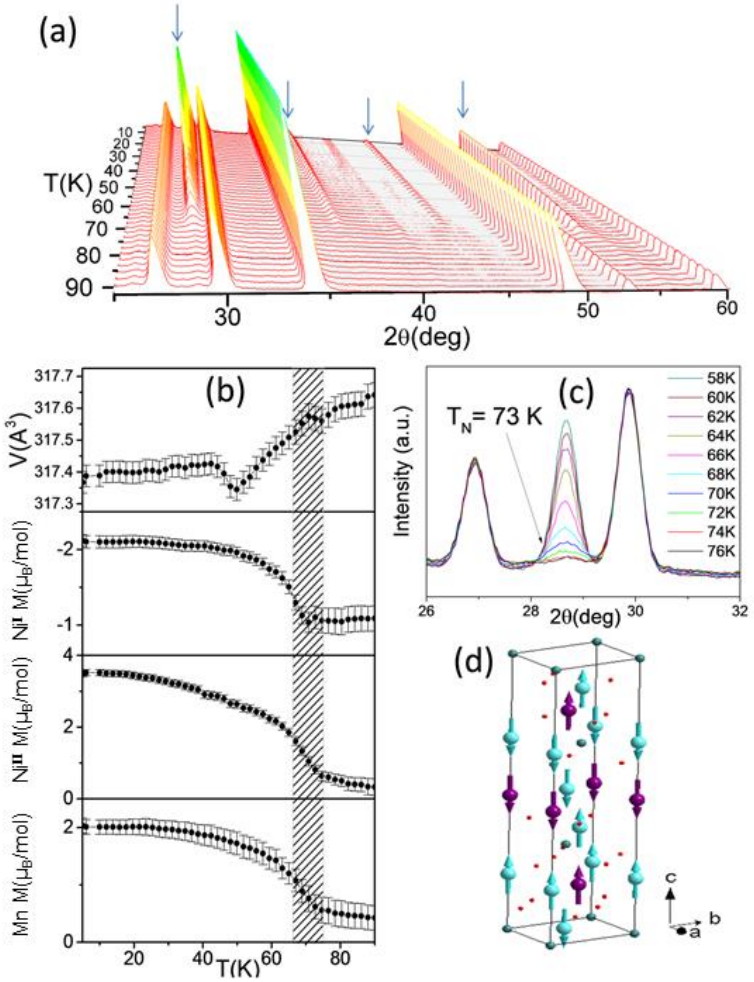

Figure 3.21 (a) Thermal evolution of the PND pattern of polycrystalline Ni_2MnTeO_6, demonstrating the peaks related to the antiferromagnetic transition occurring at 73 K. (b) Temperature dependence of the volume and magnetic moments per magnetic cation. (c) Prominent magnetic transition at 73K, as seen by the evolution of the PND peak. (d) Schematic representation of the magnetic structure of Ni_2MnTeO_6 (purple: Mn, cyan: Ni).

Multiferroic properties

The temperature dependence of the magnetic susceptibility measurements for Ni_2MnTeO_6 single crystal is displayed in Figure 3.22, for two orientations of the magnetic field: $\boldsymbol{H}_{ext} \parallel c$-axis and $\boldsymbol{H}_{ext} \parallel ab$-plane. The antiferromagnetic transition is manifested approximately at 67 K, with a salient preference along *c*-axis, as expected due to the magnetic structure (Figure 3.21). The discrepancy between the attributed Néel temperature of 73 K from PND data and 67 K from the magnetic measurements, can be ascribed to the different experimental techniques, as well as the different samples, that being polycrystalline for the first case and single crystal for the second.

In Figure 3.22(right), the temperature dependence of permittivity in ceramics is shown, as measured at 1 MHz. The anomaly appearing at 67 K, at the vicinity of the AFM transition, indicates interplay of the magnetic and FE phase transition. Additional dielectric anomaly is clearly seen at 23 K. This temperature corresponds to the AFM phase transition in Mn_3TeO_6.

Although XRD did not reveal any secondary Mn_3TeO_6 phase in the Ni_2MnTeO_6 ceramics, a small concentration (less than 3%) may have been overlooked. According to literature, Mn_3TeO_6 should hold the non-centrosymmetric rhombohedral $R\bar{3}$ space group down to 5 K.[258] Nevertheless, it is possible that Mn_3TeO_6 undergoes a not yet recorded spin-order induced FE phase transition at 23 K, but the FE distortion is so small that it is not seen in previously published PND. Note that most of spin-order induced FEs were not resolved in diffraction experiments, but only in dielectric measurements.[194]

In Figure 3.23, the magnetic field dependence of magnetization for both Ni_2MnTeO_6 single crystal (left) and ceramics (right) is presented. The single crystal experiment was done at 5 K and for two magnetic field orientations: $\boldsymbol{H}_{ext} \parallel c$-axis and $\boldsymbol{H}_{ext} \parallel ab$-plane, up to 5 T. The ceramics

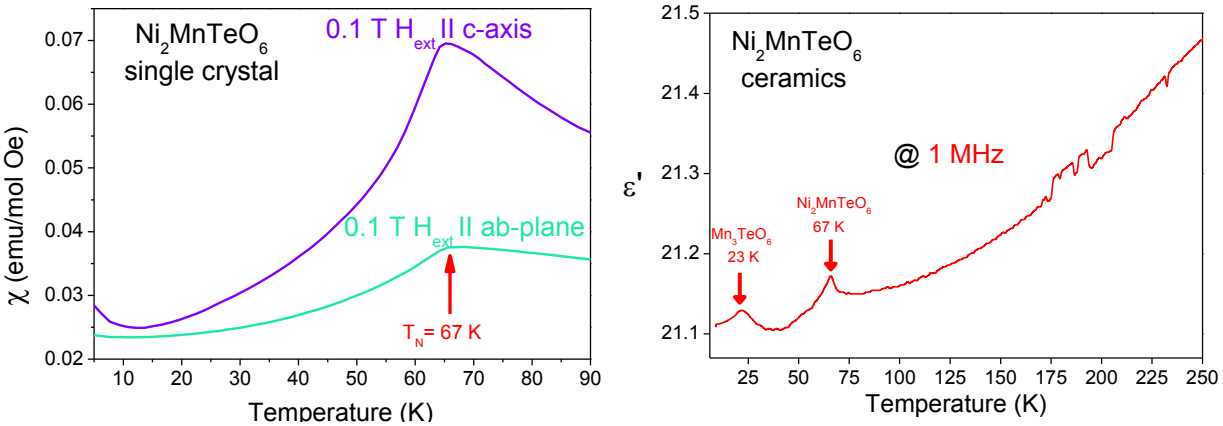

Figure 3.22 Temperature dependence of: (left) magnetic susceptibility for Ni_2MnTeO_6 single crystal, at 0.1 T with two distinct orientations: $\boldsymbol{H}_{ext} \parallel c$-axis and $\boldsymbol{H}_{ext} \parallel ab$-plane. The anomaly appears at around 67 K. (right) Temperature dependence of permittivity of Ni_2MnTeO_6 ceramics, recorded at 1 MHz. The AFM transition for Ni_2MnTeO_6 occurring around 67 K is responsible for the dielectric anomaly. Secondary phase of Mn_3TeO_6 is probably responsible for the anomaly at 23 K.

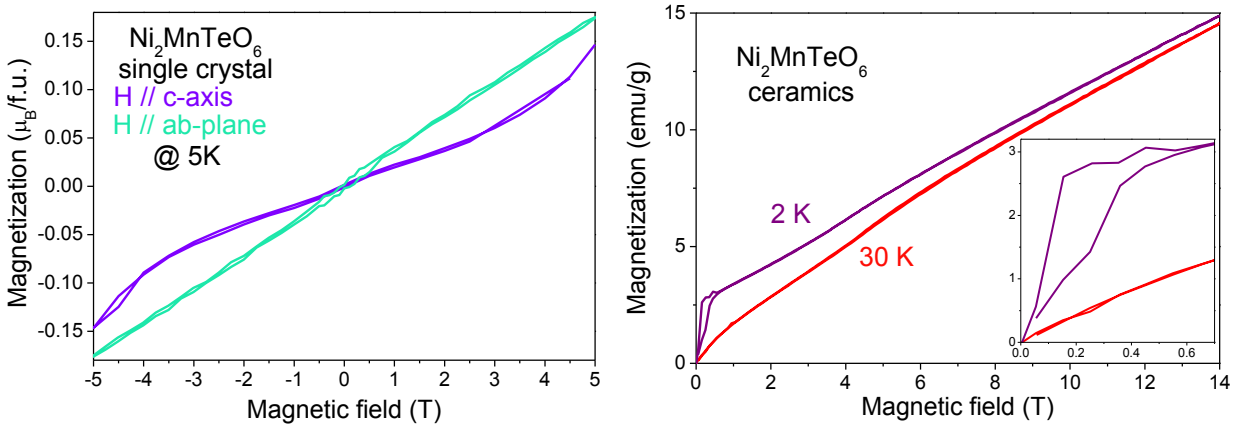

Figure 3.23 Magnetic field dependence of magnetization for Ni_2MnTeO_6 (left) single crystal and (right) ceramics. In the single crystal a spin-flop transition occurs at around 4.5 T, however not visible in the ceramics. Right inset: the low magnetic field hysteretic behavior in ceramics, most possibly in Mn_3TeO_6 secondary phase.

were measured at 2 and 30 K, up to 14 T. The single crystal shows along the *c*-easy-axis of magnetization a non-hysteretic spin-flop transition around 4 T, resembling its undoped counterpart Ni_3TeO_6, yet appearing at ~3 T lower value of magnetic field. Curiously, the ceramics barely present a negligible bend of the magnetization curve approximately at 4.5 T, whereas a hysteretic behavior of possibly FM origin appears at very low fields, below 0.3 T.

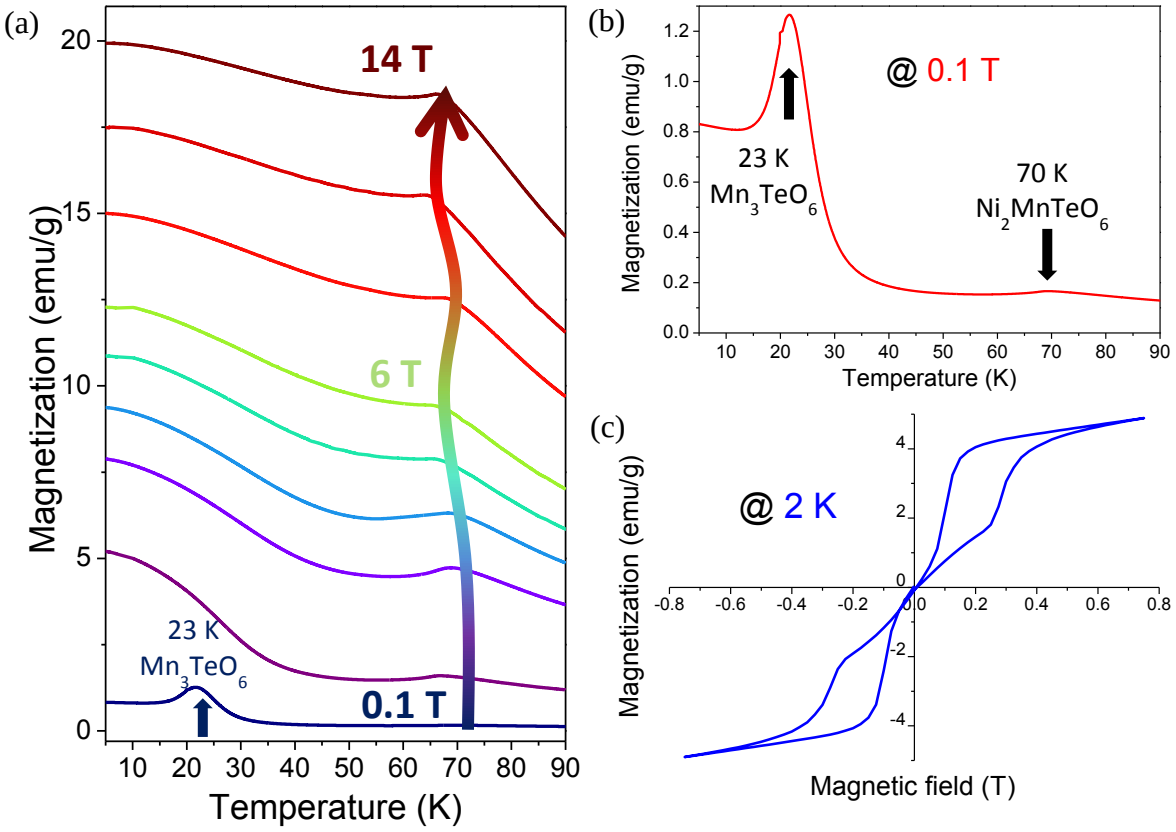

Figure 3.24 Temperature dependence of magnetization at a) up to 14 T, b) at 0.1 T of Ni_2MnTeO_6 ceramics. Two conspicuous AFM transition temperatures at 23 and 70 K attest the presence of two distinct phases, Mn_3TeO_6 and Ni_2MnTeO_6 respectively. d) A hysteretic magnetic field dependence of magnetization, recorded at low magnetic fields up to 0.8 T and at 2 K.

Figure 3.24(a) presents the temperature dependence of magnetization for the polycrystalline Ni_2MnTeO_6. The magnetic transition takes place at around 70 K, presenting proximity to the PND results. Oddly, a noteworthy anomaly at 23 K, suggests a secondary magnetic transition. However, no trace of any other phase transition was present at neither the PND nor the single crystal susceptibility measurements. Interestingly, the magnetic transition of Mn_3TeO_6 occurs at 23 K, a fact that implies the presence of a secondary phase in the polycrystalline sample. Another possible explanation for the noted feature might be impurities from the grain boundaries, which can contribute to the total magnetization. The magnetic structure changes above 0.4 T (double hysteresis loop is seen - Figure 3.24(c)), and therefore the low-temperature

anomaly in M(T) (Figure 3.24(a)) disappears at higher fields. The magnetization peak seen near 70 K exhibits an interesting anomaly with magnetic field. It shifts from 70 K (at 0.1 T) to 65 K (at 14 T) with some nonlinearity around 6 T.

Spin and lattice excitations

The IR reflectivity spectra of the Ni_2MnTeO_6 ceramics are shown in Figure 3.25(a) for selected temperatures from 10 to 300 K, together with the fitted complex permittivity. As predicted by factor group analysis for the *R*3 structure, 9 $E(x,y,x^2-y^2,xy,xz,yz)$ and 9 $A(x^2+y^2,z^2,z)$ modes are expected, both IR and Raman active, analogously as for the Ni_3TeO_6 case.[144,243] All 18 modes are clearly visible in the IR spectra up to 300 K. Similarly to Ni_3TeO_6, the phonon eigenfrequencies are practically unaffected by temperature changes, since the *R*3 space group is preserved up to RT. Merely the damping of the modes slightly decreases upon cooling, as expected. A few of the mode frequencies lie close to the values of those reported for Ni_3TeO_6,[144,243] most of them corresponding to the vibrations of the TeO_6 octahedra.[247] The eigenfrequency values of the measured IR active modes at 10 K, together with the respective damping and dielectric strength, are presented in Table 3.3. The previously published Ni_3TeO_6 IR modes at 7 K by Skiadopoulou *et al.*[144] are also listed, for comparison. The possible structural distortion at the AFM (and FE) transition at 67 K suggested by the anomaly in the permittivity data (Figure 3.22(right)) should have only a negligible effect on the IR spectra.

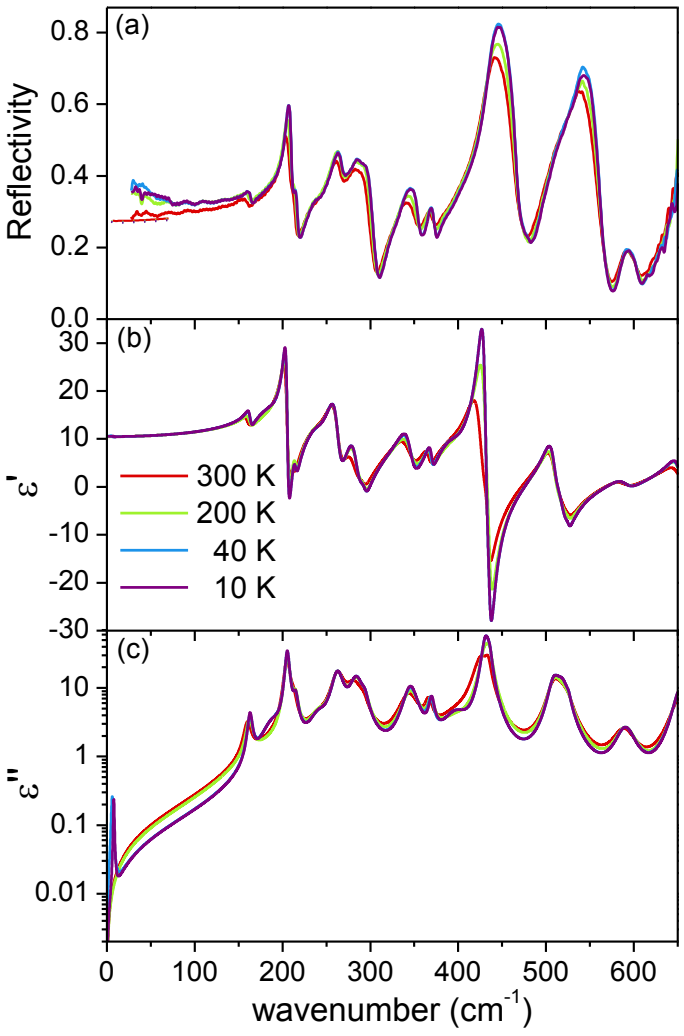

Figure 3.25 (a) IR reflectivity experimental spectra at selected temperatures from 10 to 300 K. (b) Real and (c) imaginary part of permittivity, as obtained from the fits.

In Figure 3.25(b) and (c), the real and imaginary parts of permittivity are displayed, respectively, after fitting the reflectivity spectra of Figure 3.25(a), by the use of three-parameter damped harmonic oscillators (see Section 2.1.2.1, equation 2.11). The static permittivity corresponds to approximately 10, quite close in agreement with the value reported for Ni_3TeO_6 by Oh *et al.*[63] who reported permittivity around 11 in radio-frequency range. Note that the static permittivity of Ni_3TeO_6 ceramic pellets observed by Skiadopoulou *et al.*[144] was significantly lower (~5), due to the presence of high porosity in the samples. The ceramic samples of Ni_2MnTeO_6 of the current study are exceptionally dense, resulting in almost doubling of the absolute value of the reflectivity, and therefore nearly double static permittivity. 1 MHz permittivity of our ceramics seen in Figure 3.22(right) has value even higher than 20, but it is probably enhanced by a contribution of interlayer barriers on grain boundaries, which are responsible for Maxwell-Wagner contribution to permittivity,[225] dominant especially above 100 K.

The highly dense ceramics allowed micro-Raman studies with the possibility of focusing at a single grain, since the grain size of 50 μm was much larger than the ~2 μm size of the laser spot. The spectra were collected at back-scattering geometry, in both parallel and crossed polarizations, at temperatures from 4 to 300 K. Here, only the crossed polarized spectra are presented, since no significant differences were observed between the two polarizations, apart from the intensity magnitudes. A logarithmic plot of the Raman spectra, at selected temperatures from 4 to 300 K, is shown in Figure 3.26. The Raman mode frequencies at 4 K are presented in Table 3.3, in comparison with the IR modes at 10 K. The polycrystalline nature of the samples does not allow for symmetry analysis of the observed modes. From the 18 modes observed in the spectra, 6 are quite weak (noted with "w" subscript in Table 3.3), presumably originating from polarization leakage, since each grain has a random orientation in respect to the beam propagation. Some of the Raman modes might also be LO modes (similarly

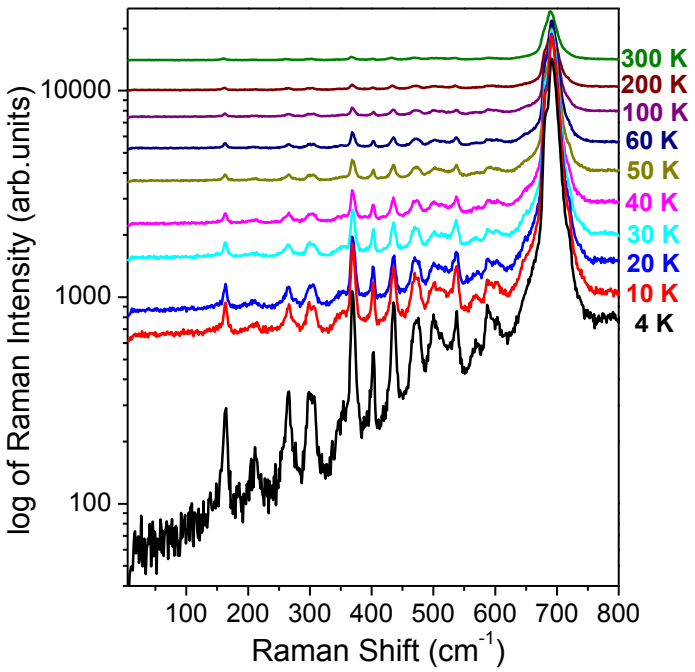

Figure 3.26 Raman cross-polarized spectra for different temperatures from 4 to 300 K.

as in Ni_3TeO_6 – see the table Table 3.2). As for the case of IR spectra, no substantial temperature changes are evidenced up to RT.

Time-domain THz transmission measurements were performed for the Ni_2MnTeO_6 ceramics (thickness 1.9 mm), at temperatures from 4 to 300 K. In Figure 3.27 the temperature dependence of the THz spectra is presented for selected temperatures. A gradual decrease of the real part of the index of refraction occurs on cooling. The increase of *n* towards the higher frequency range comes from the phonon contribution, and its value of approximately 3 is in agreement with the static permittivity value obtained from the IR spectra. A new low frequency excitation at around 6 cm^{-1} appears at 60 K, below the AFM transition of ~70 K, and upon cooling it sharpens and shifts to 8 cm^{-1} at 4 K. Note that the signal is rather noisy below 8 cm^{-1}, since it is on the border of our frequency region. The emergence of the new excitation below the magnetic transition, in combination with the fact that all 18 phonons predicted by factor group analysis are resolved in IR and Raman spectra, and lie above ~160 cm^{-1}, suggest that this new excitation has magnetic origin. A broader excitation is also notable at higher frequencies (~40cm^{-1}) in $k(\omega)$ spectra, and also emerging below T_N, possibly due to multimagnon absorption. However, it is also possible to correspond to a single magnon excitation, since a similar excitation was observed at 32 cm^{-1} in Ni_3TeO_6; the high value of damping could be attributed to the chemical disorder of Mn in the lattice (PND revealed Mn in B sites of $A_2B_2O_6$ (B=Mn, Te)).

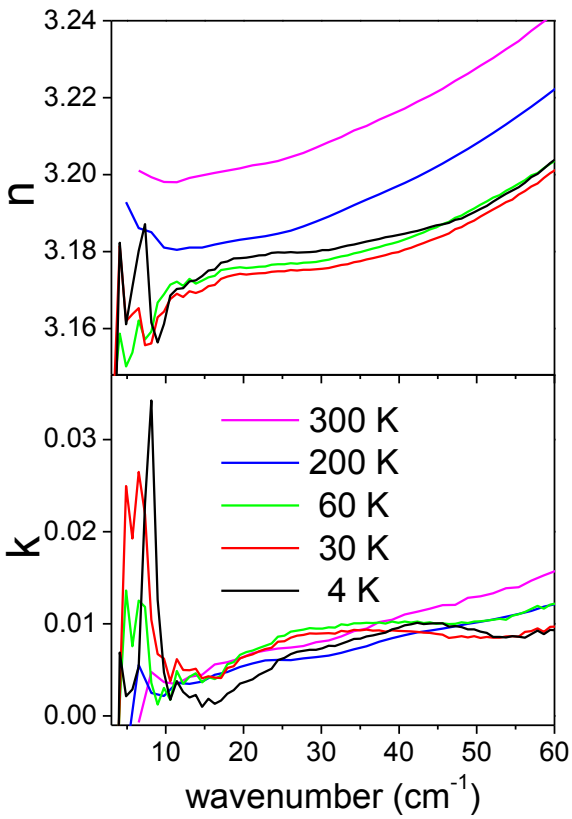

Figure 3.27 Temperature dependence of the (a) real and (b) imaginary part of the complex index of refraction, obtained from THz time-domain spectroscopy.

Table 3.3 Frequencies of the IR active modes in the Ni_2MnTeO_6 ceramics at 10 K and Raman active modes at 4 K, as obtained by the fits of IR reflectivity with ε_∞ =3.9. The low frequency mode in the first line comes from the THz spectra. The first column corresponds to the IR mode frequencies of Ni_3TeO_6 ceramics at 7 K from Skiadopoulou *et al.*[144] The damping constants and dielectric strength of the IR-active modes are also listed. The modes observed as weak in Raman spectra are marked by w in subscript.

Ni_3TeO_6[144]	Ni_2MnTeO_6			
IR 7 K	Raman 4 K	IR 10 K		
ω_{TO} (cm^{-1})	ω_{TO}(cm^{-1})	ω_{TO}(cm^{-1})	γ_{TO}(cm^{-1})	$\Delta\varepsilon$
16.2		7.9	1.3	0.04
32.4				
	164.6	163.1	5.8	0.12
185.0	185.5_w	189.2	28.5	0.34
	211.2	205.4	5.4	0.85
219.3		214.8	6.4	0.16
232.1		240.9	23.9	0.23
259.2	266.0	262.8	14.5	0.83
279.3		284.2	17.3	0.74
303.1	300.0	293.6	8.7	0.07
313.2	354.1_w	345.8	18.1	0.50
345.2	369.7	369.8	7.2	0.10
361.7	403.2	397.2	33.4	0.25
380.0		431.4	9.8	1.17
406.6	436.5	435.7	6.3	0.21
454.2	475.6			
466.1	484.3			
516.5	501.6	509.3	14.4	0.29
536.6	538.0	518.7	17.1	0.31
	570.8_w	525.5	5.5	0.01
597.1	590.6	590.6	24.6	0.09
661.2	603.4_w	653.9	17.7	0.27
	681.0_w			
	693.6			
	720.0_w			

We investigated THz spectra also in external magnetic field up to 7 T in the Voigt configuration with $\boldsymbol{H}_{ext}$ parallel and perpendicular to electric vector $\boldsymbol{E}^{\omega}$ of THz beam. Here, we present only the spectra with $\boldsymbol{H}_{ext} \perp \boldsymbol{E}^{\omega}$ (Figure 3.28), since the magnetic field effect upon the spin excitation was more pronounced (yet qualitatively the same). At 30 K (Figure 3.28(left)), the magnetic mode below 10 cm^{-1} shifts down and sharpens with increasing magnetic field. At 5 K (Figure 3.28(right)), a conspicuous sharpening up to 4 T takes place, followed by decrease of

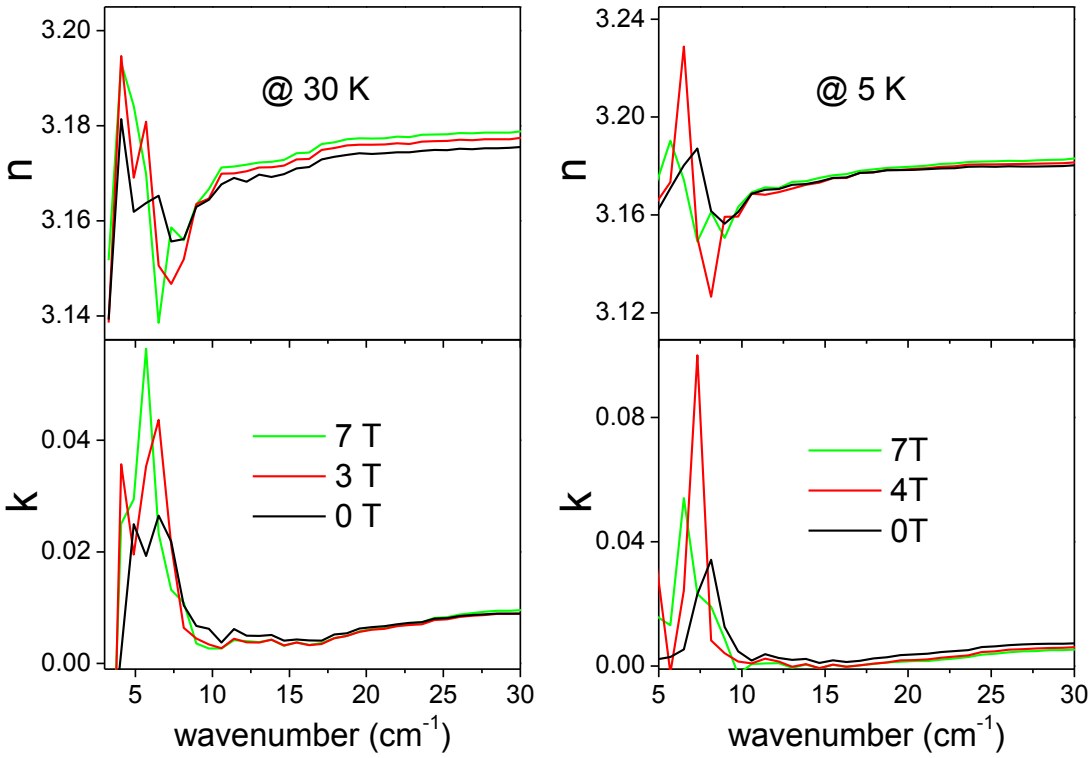

Figure 3.28 Real and imaginary part of index of refraction from the THz measurements of Ni_2MnTeO_6 ceramics, at external magnetic field in Voigt configuration $\boldsymbol{H}_{ext} \perp \boldsymbol{E}^{\omega}$, for 30 K (left) and 5 K (right) as measured.

its intensity upon increasing $\boldsymbol{H}_{ext}$ up to 7 T. Such behavior might be related to the spin-flop transition occurring at around 4.5 T (Figure 3.23) or by reduced sensitivity of our detector at low frequencies. Nevertheless, at 5 K a clear magnon frequency softening is exhibited with increasing $\boldsymbol{H}_{ext}$, from 8 cm^{-1} at 0 T to 6 cm^{-1} at 7 T.

3.3.2.4 Discussion

The novel compound of Ni_2MnTeO_6 was successfully grown for the first time in form of single crystals and ceramics, obtaining the polar *R*3 space group symmetry. The magnetic order is AFM along *c*-axis, organized in FM *ab*-planes. It exhibits multiferroic properties, since magnetic and dielectric anomalies appear at the same critical temperature of approximately 70 K. Ni_2MnTeO_6 behaves quite similarly as its undoped counterpart Ni_3TeO_6,[63,239] however with the advantage of higher AFM transition temperature of ~70 K, almost 20 K higher than the 53 K of Ni_3TeO_6. Such behavior was predicted by Mathieu *et al.*,[260] who studied 20% Mn-doped Ni_3TeO_6 presenting T_N=67 K, with the same *R*3 polar space group symmetry as the undoped one. Their study revealed the increase of AFM interaction strength upon increase of Mn concentration, since T_N and θ_{CW} are co-varying, thus leaving the magnetic frustration parameter

$f = -\theta_{cw}/T_N$ unchanged. It is noteworthy to mention that the non-polar (space group $R\bar{3}$) Mn_3TeO_6 presents a highly frustrated long-range incommensurate magnetic structure, which orders below 23 K,[258,260] however Ni_2MnTeO_6 crystalizes in the polar *R*3 symmetry and keeps the low magnetic frustration values of Ni_3TeO_6.

In addition, a spin-flop transition was observed in the single crystal at ~5 T, however only slightly seen in the ceramic sample. Ni_3TeO_6 exhibits colossal static magnetoelectric coupling at the spin-flop transition, which occurs at ~8 T. Pyrocurrent or capacitance measurements at external magnetic field are required, in order to investigate the possibility of similar behavior, which would favor applications, being at higher temperature and lower magnetic field.

Surprisingly, a second anomaly at 23 K was observed in the dielectric and magnetic measurements of polycrystalline Ni_2MnTeO_6 samples. This anomaly was absent in the single-crystal data. The natural suspicion is to consider that it arises from the presence of a secondary phase of Mn_3TeO_6, since the latter presents magnetic ordering at 23 K. Previously published structural study by PND claims a non-centrosymmetric rhombohedral $R\bar{3}$ structure below T_N,[258] but it cannot explain the anomaly seen in permittivity at T_N. A dielectric anomaly is a signature of a FE phase transition, so the low-temperature structure is probably *R*3, but it was not revealed in PND, probably due to a small FE distortion induced by the spin order. Further chemical analysis of the ceramic samples should be made, in order to investigate for secondary phases and/or impurities. Preliminary energy dispersive spectroscopy (EDS) studies revealed stoichiometric Ni_2MnTeO_6 composition.

The lattice excitations studies of Ni_2MnteO_6 ceramics by IR and Raman spectroscopy record all 18 IR and Raman active modes, as predicted by the factor group analysis for the *R*3 space group. The high quality dense ceramic samples produce almost double reflectivity values in comparison with the porous Ni_3TeO_6 samples studied previously by the same authors.[144] As a result, the obtained value of static permittivity of about 10 lies closer to 11, which was observed by Oh *et al*.[63] in Ni_3TeO_6 at the radio-frequency range.

The time-domain THz spectroscopy spectra reveal a low-frequency excitation below the AFM transition of about 70 K. The excitation is tuned by the application of external magnetic field $\boldsymbol{H}_{ext}$, up to 7 T. A similar excitation was seen in Ni_3TeO_6, however, appearing simultaneously in both THz and Raman spectra, thus corresponding to a magnetoelectric excitation, or else electromagnon. In Ni_2MnTeO_6 the excitation is not seen in Raman spectra, most possibly because its frequency is much lower, starting from 6 cm^{-1} at 30 K (it was not possible to resolve it at higher temperatures) and reaching 8 cm^{-1} at 5 K. These frequencies are

quite low for the Raman studies, since they are screened by the strong quasi-elastic scattering of the laser beam and/or cutoff limit of the Bragg filter, which in the current case is around 8 cm^{-1}. In order to moderate the screening effect, as well as the heating of the sample by the laser beam, we reduced the laser power down to 10%, but still no excitation was seen. Moreover, the Ni_3TeO_6 Raman data were recorded with a single crystal, whereas the polycrystalline Ni_2MnTeO_6 could reduce the magnon intensity. Nevertheless, numerous grains were studied to make sure that it is not a crystallite orientation effect. What is more, further Raman studies of multiple grains and/or angular dependence of the spectra would assist for a detailed symmetry analysis.

Lastly, the very small size of the single crystals did not allow for the proper spectroscopic studies based on the orientation of the crystal structure. For example, directional dichroism could reveal the character of the spin excitation observed in the THz spectra, whether that corresponds to a pure magnon or electromagnon, like in its undoped counterpart Ni_3TeO_6. In addition, by using the single crystals one can avoid the possible impurities often present on the grain boundaries of polycrystalline samples, thus the mysterious anomaly seen at 23 K could be clarified. And last but not least, capacitance and pyrocurrent measurements at external magnetic field of Ni_2MnTeO_6 single crystals could shed more light on the multiferroic properties of Ni_2MnTeO_6, since the very similar compound of Ni_3TeO_6 presents colossal magnetoelectric effect, among the highest observed in single phase multiferroics.

3.3.2.5 Conclusions

Single crystals and polycrystalline ceramic samples of the novel compound of Ni_2MnTeO_6 were synthesized for the first time. The Mn-doping of Ni_3TeO_6 induces increase of the AFM transition temperature by 20 K, thus reaching approximately 70 K, while at the same time it preserves the polar *R*3 space group of the undoped Ni_3TeO_6. An anomaly at the same critical temperature is also seen in the low-frequency permittivity spectrum. However, the second anomaly at 23 K requires further investigation. Moreover, a spin-flop transition is triggered by external magnetic field above 5 T, i.e. ~3 T lower than that of Ni_3TeO_6.

The high quality dense ceramic samples revealed all expected IR and Raman active modes of the *R*3 symmetry. A magnetic field-tunable spin excitation at approximately 8 cm^{-1} is clearly seen in the THz spectra, below T_N. The marginally low frequency of the magnon does not allow simultaneous detection in Raman spectra, leaving the question open on whether it bears a magnetoelectric character or not.

3.3.3 **Co-doped Ni_3TeO_6**

Analogously as for Ni_2MnTeO_6, the case of Ni substitution by Co in Ni_3TeO_6 follows the same concept of modifying the magnetic structure, while keeping the non-centrosymmetricity of *R*3 space group. The $Ni_{3-x}Co_xTeO_6$ compounds do not present higher T_N than their undoped counterpart Ni_3TeO_6, as the impressive 20 K increase of T_N performed by Ni_2MnTeO_6. However, they demonstrate markedly rich spin-wave spectra, strongly influenced by temperature changes and external magnetic field.

Below, the impressive magnetic excitations in the THz spectra (at 5 K and as a function of the external magnetic field) are displayed, as a preview to the coming section. At least two of them correspond to electromagnons, due to simultaneous detection by THz and Raman spectroscopies.

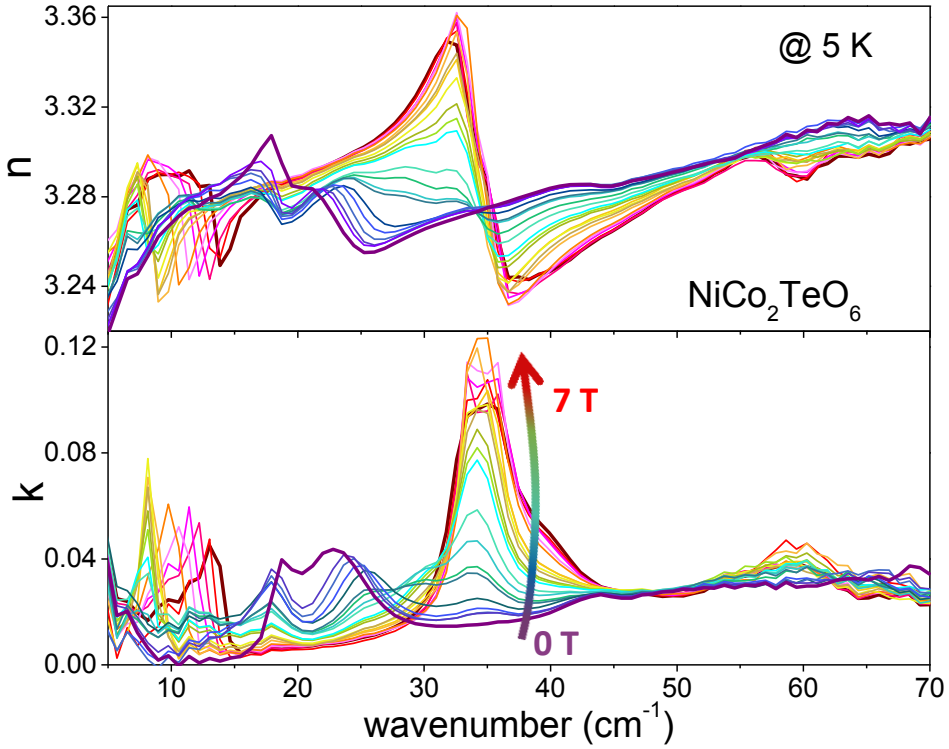

3.3.3.1 Introduction

The foundation of the multiferroicity hypothesis for $Ni_{3-x}Co_xTeO_6$ compounds is the same as described for Ni_2MnTeO_6 in paragraph 3.3.2.1. The striking difference though is that no previous attempt of Co-doped Ni_3TeO_6 was ever reported, in contradiction to $(Mn_{0.2}Ni_{0.8})_3TeO_6$ (20% Mn-doped Ni_3TeO_6),[260] thus one might say that $Ni_{3-x}Co_xTeO_6$ surpass Ni_2MnTeO_6 in novelty terms.

Interestingly enough though, the cryolite-related Co_3TeO_6 with a monoclinic *C*2/*c* space group symmetry down to 1.9 K,[259] undergoes at least 3 magnetic phase transitions at approximately 26, 21 and 18 K.[257,259,262–265] The last one manifests a first-order phase transition, as seen by anomalies in lattice parameters, heat capacity and dielectric measurements,[257,262] suggesting multiferroic character. PND experiments,[259] supported by symmetry considerations,[263,264] yield an uncommon to spin-induced FEs coexistence of magnetic order parameters with distinct propagation wavevectors (Figure 3.29). The critical temperatures mentioned above might slightly differ among the various publications, possibly due to the high complexity of magnetic interactions and/or mixed valence states of Co^{2+} and Co^{3+}.[265,266] The diversity among oxidation states of Co cations originates in the five different crystallographic sites, which coordinate Co in tetrahedral, octahedral and square-pyramidal geometries.[267] Each geometrical coordination of Co in the oxygen environment designates diverse crystal field splitting (Figure 3.30).

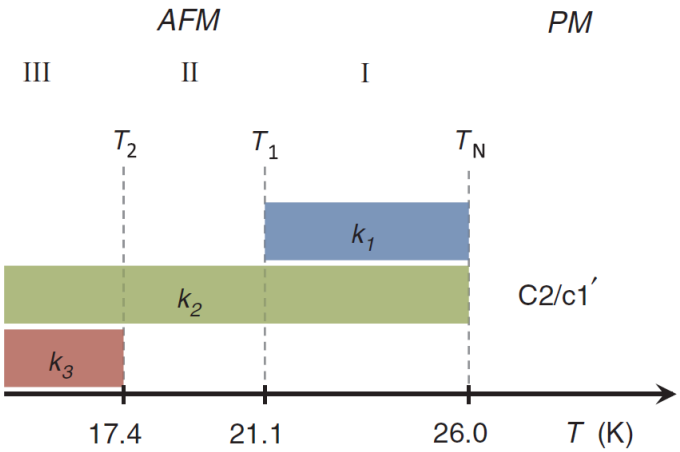

Figure 3.29 Phase diagram depicting the three magnetic phase transitions of the spin-induced ferroelectric Co_3TeO_6. Phase I corresponds to incommensurate structure, whereas Phases II and III to commensurate. The propagation vectors are: $\vec{k}_1 = (0,\ 0.480,\ 0.055)$, $\vec{k}_2 = (0,0,0), \vec{k}_3 = \left(0, {}^1/_2, {}^1/_4\right)$. (image taken from Ref. 263)

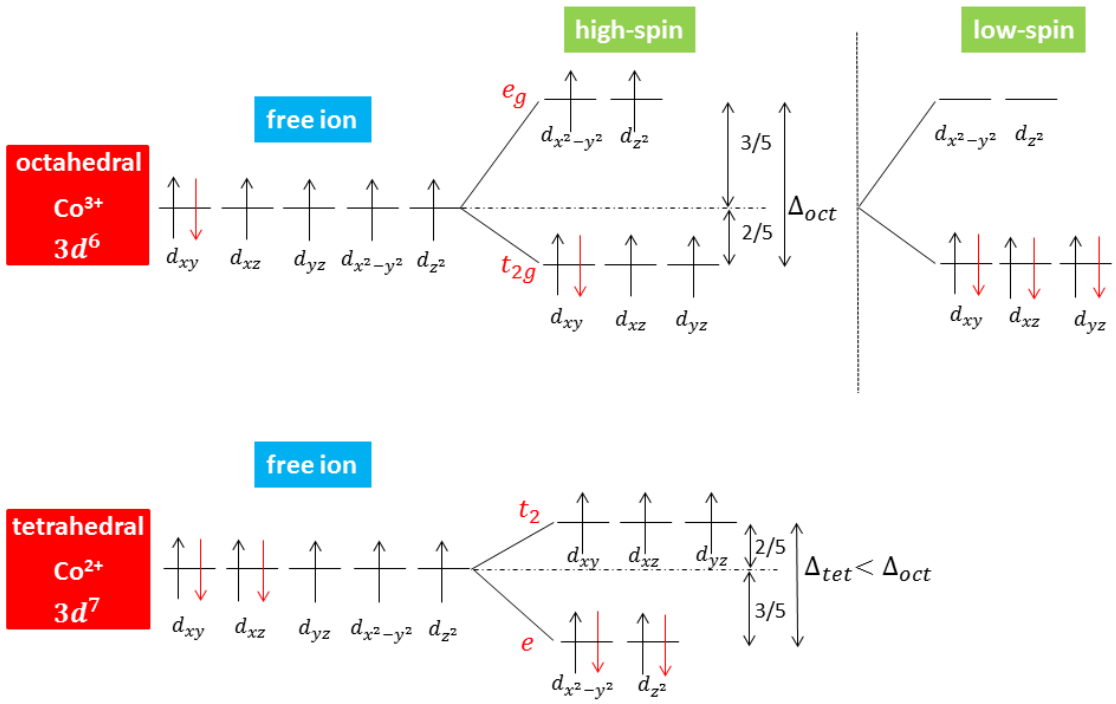

Figure 3.30 Crystal field splitting for the octahedral and tetrahedral geometry of Co in the lattice. (image created by the author)

The peculiar multiferroicity and magnetic ordering of Co_3TeO_6, in combination with the capital magnetoelectric coupling in Ni_3TeO_6, led to the concept of Co-doped Ni_3TeO_6. Ni_2CoTeO_6 and $NiCo_2TeO_6$ were synthesized for the first time, in form of single crystal and polycrystalline samples. They both crystallize in the polar *R*3 space group, such as the parent structure of Ni_3TeO_6. The AFM phase transitions occur at approximately 52 and 49 K for Ni_2CoTeO_6 and $NiCo_2TeO_6$, respectively. Anomalies in the permittivity were observed at the magnetic transitions for both compounds. The spin excitation spectra are remarkably rich, particularly for $NiCo_2TeO_6$. Two spin-wave modes are seen simultaneously in THz and Raman spectra, thus assigned as electromagnons.

3.3.3.2 Experimental details

Single crystal and polycrystalline pellets were successfully grown in the composition of Ni_2CoTeO_6 and $NiCo_2TeO_6$. The experimental procedure of sample preparation and characterization for the above compounds was identical to the one of Ni_2MnTeO_6 of section 3.3.2.2.

3.3.3.3 Results

Multiferroic properties

Single crystals and polycrystalline samples of Ni_2CoTeO_6 and $NiCo_2TeO_6$ were characterized by PND and XRD, revealing pure phases of the non-centrosymmetric *R*3 space group symmetry. The temperature dependence of susceptibility for Ni_2CoTeO_6 and $NiCo_2TeO_6$ single crystals reveals AFM phase transitions at 55 and 52 K, respectively (Figure 3.31(a) and (b)). Evidently, the magnetic transition of both samples resembles the one of Ni_3TeO_6, unlike the Mn-doped case of the Ni-based telluride family, which orders antiferromagnetically at around 70 K. The measurement was done after applying 0.1 T, at zero field cooling, and for two different magnetic field configurations: $\boldsymbol{H}_{ext} \parallel c$-axis and $\boldsymbol{H}_{ext} \parallel ab$-plane. In contradiction to the Ni_2MnTeO_6 behavior of *c*-easy-axis magnetization, both Co-doped compounds present *ab*-easy-plane magnetization. An additional anomaly at around 35 K is present in Ni_2CoTeO_6, possibly due to a second magnetic phase transition.

In a similar way, the polycrystalline samples exhibit AFM ordering, however at slightly lower temperatures of 52 and 49 K, for Ni_2CoTeO_6 and $NiCo_2TeO_6$ respectively, as demonstrated in the magnetization temperature dependence in Figure 3.31(c) and (d). At the same plot one can also see the magnetic field dependence of the magnetization curves, up to 8 T for Ni_2CoTeO_6 and up to 12 T for $NiCo_2TeO_6$. The first shows a slight increase of T_N up to 3 T and then gradual decrease, whereas the second displays a clear continuous decrease of T_N, approximately down to 35 K at 12 T. The lower temperature anomaly from Ni_2CoTeO_6 single crystal is not apparent in the ceramics, probably due to its weaker nature than the high-temperature one, the fact that it is only *ab*-plane sensitive, and most essentially, the averaging of the crystallite orientation in the polycrystalline sample.

The magnetic field dependence of magnetization is shown in Figure 3.32(a), (b) for single crystals and (c), (d) for ceramics. Ni_2CoTeO_6 presents a hysteretic spin-flop transition at approximately 7 T, very close to the one of Ni_3TeO_6 at 8 T. The spin-flop transition is not seen in the single crystal measurement, unfortunately because the experiment was only possible to be done up to 5 T. On the other hand, the spin-flop transition of $NiCo_2TeO_6$ appears at a lower magnetic field of around 3.5 T, and is simultaneously observed in both single crystal and

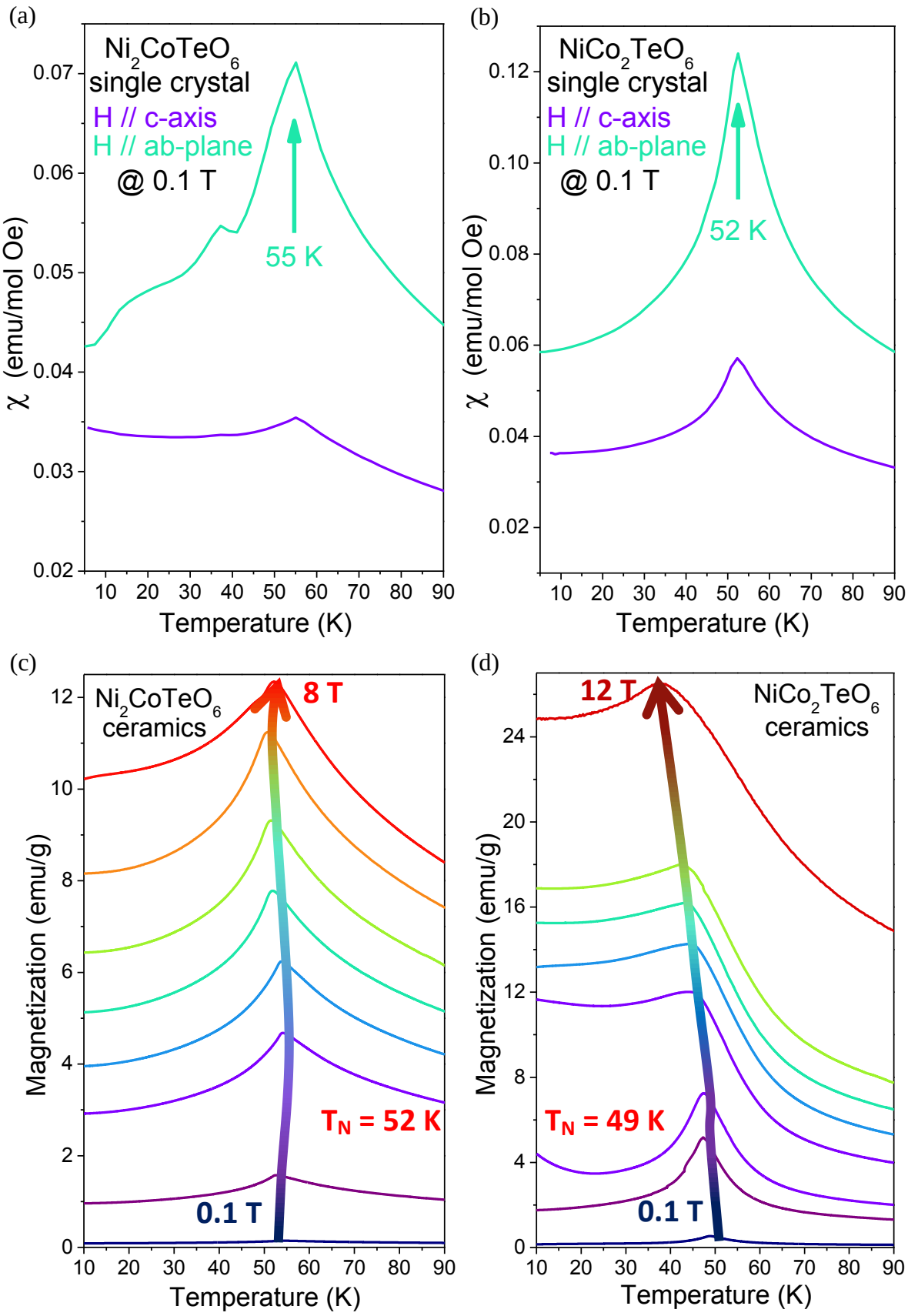

Figure 3.31 Temperature dependence of (a) Ni_2CoTeO_6 and (b) $NiCo_2TeO_6$ single crystal susceptibility at 0.1 T, for magnetic field parallel to *c*-axis and *ab*-plane. Temperature and magnetic field dependence of magnetization for (c) Ni_2CoTeO_6 and (d) $NiCo_2TeO_6$ ceramics.

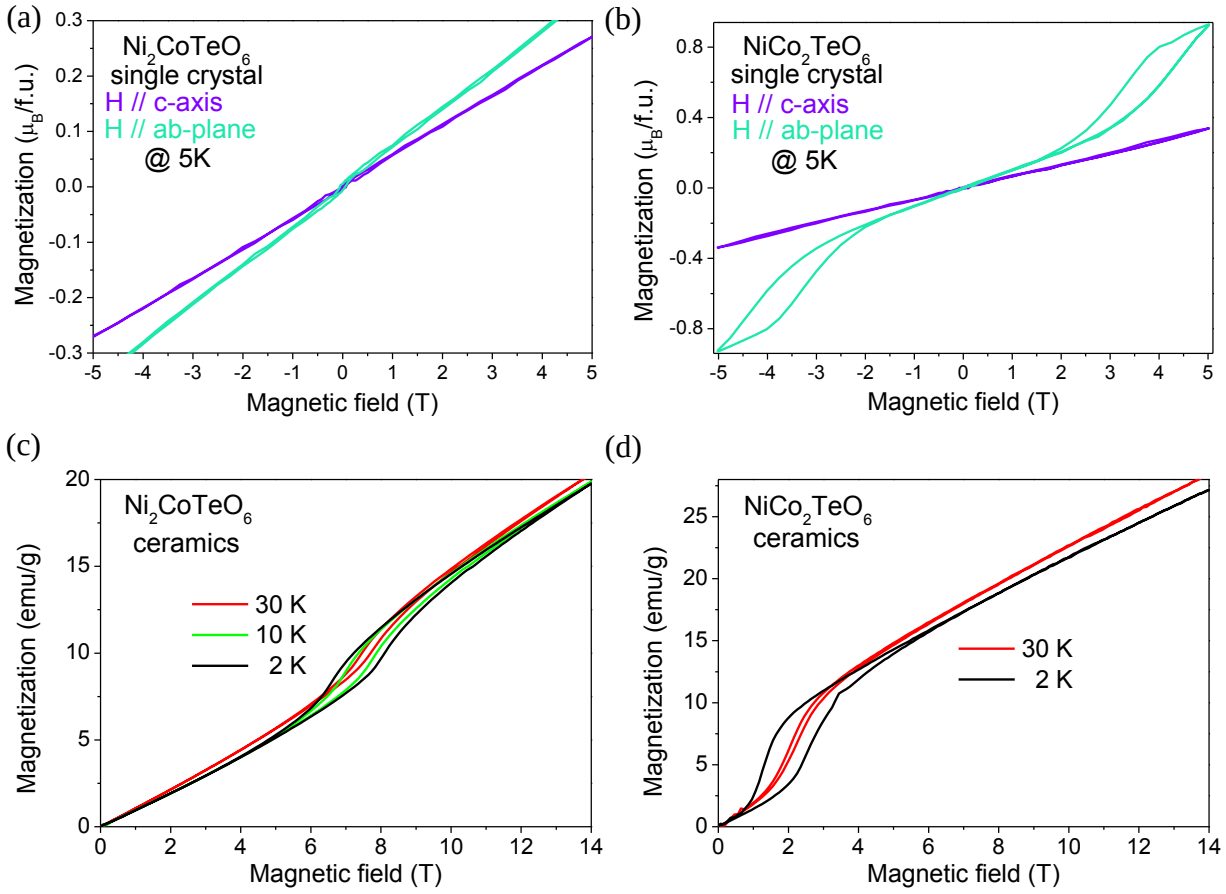

Figure 3.32 Magnetic field dependence of magnetization for (a), (c) Ni_2CoTeO_6 and (b), (d) $NiCo_2TeO_6$ single crystals and ceramics, respectively.

ceramics. Nevertheless, $NiCo_2TeO_6$ ceramics manifest the transition at almost 1 T lower field value. Finally, the hysteretic behavior increases for both samples on cooling.

As expected by the multiferroic behavior of both the undoped and Mn-doped Ni_3TeO_6, also the Co-doped counterparts express interplay of the magnetic and FE properties, as indicated by the dielectric anomaly seen at the Neél temperature (Figure 3.33). The critical temperatures appear at 53 and 47 K for Ni_2CoTeO_6 and $NiCo_2TeO_6$ ceramics respectively. The permittivity values differ among the two compounds, with Ni_2CoTeO_6 resembling Ni_3TeO_6.[63]

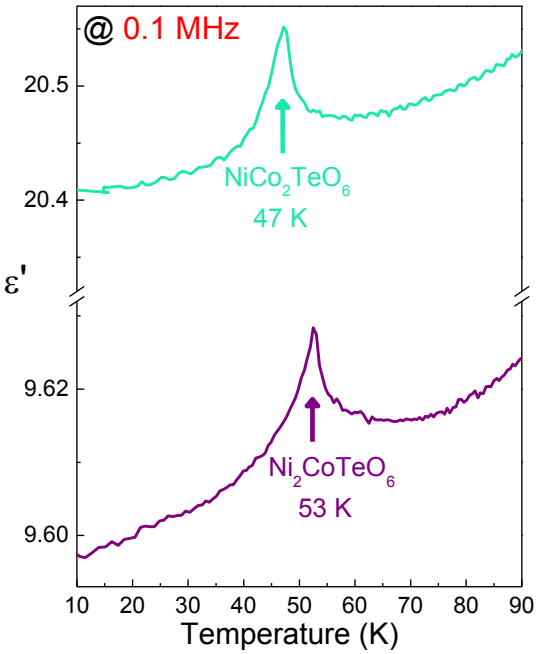

Figure 3.33 Temperature dependence of permittivity for Ni_2CoTeO_6 and $NiCo_2TeO_6$ ceramics, as measured at 0.1 MHz respectively.

Spin and lattice excitations

As will be more analytically discussed later in an attempt to compare and understand the effect of Co- and Mn-doping in Ni_3TeO_6, the main structural properties for the entire family of the compounds present almost identical vibrational spectra. Once more, all 18 vibrational modes of the *R*3 structure (9 $E(x,y,x^2-y^2,xy,xz,yz)$ and 9 $A(x^2+y^2,z^2,z)$), both IR and Raman active, as predicted by factor group analysis, are present in the IR reflectivity spectra of both Co-doped compounds in Figure 3.34(a) (left and right). The corresponding mode frequencies are listed in Table 3.4.

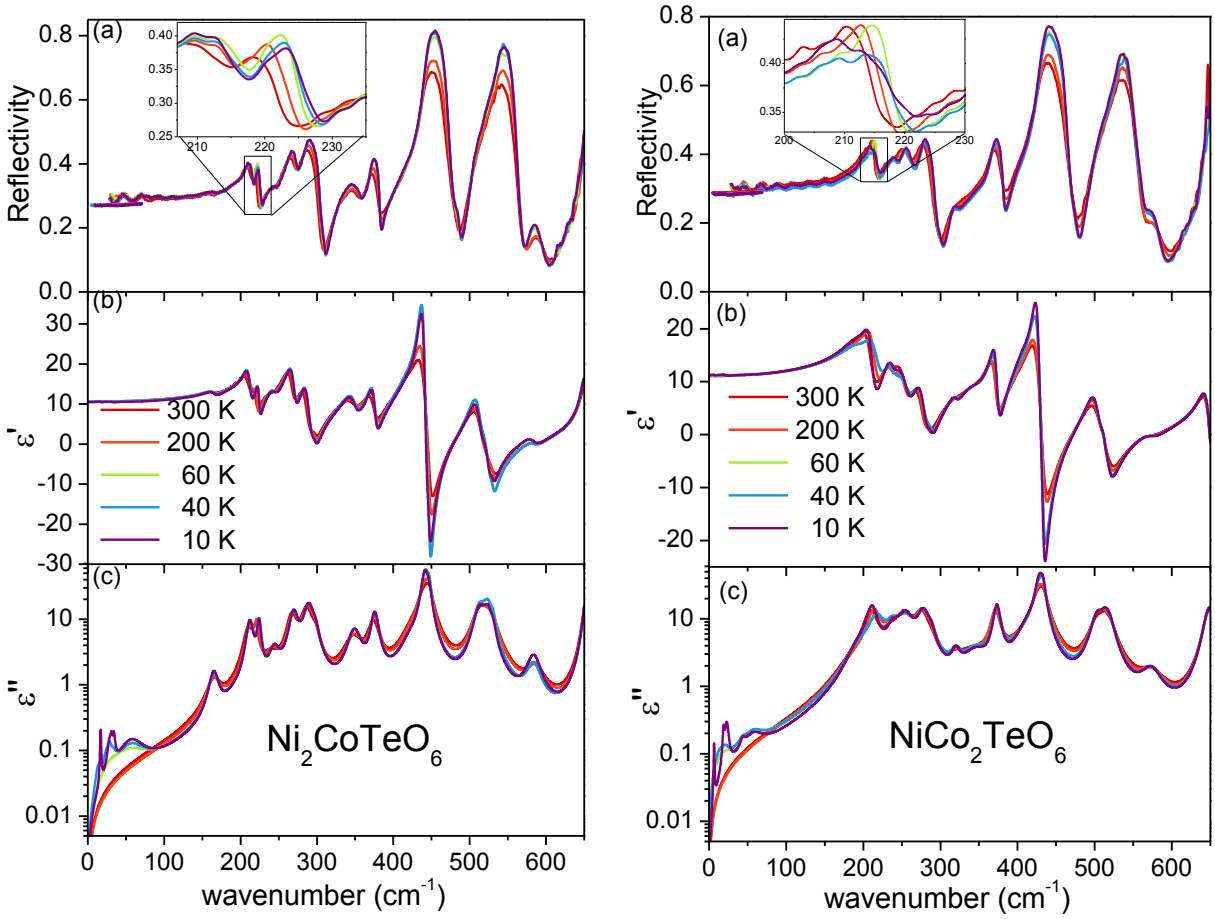

Figure 3.34 (a) Temperature dependence of IR reflectivity spectra for (left) Ni_2CoTeO_6 and (right) $NiCo_2TeO_6$ ceramics, at selected temperatures. The reflectivity spectra from the THz range are also presented, for frequencies below 70 cm^{-1}, with dotted lines. Inset: Temperature dependence of IR reflectivity of the modes (left) 220 cm^{-1} and (right) 215 cm^{-1}, showing conspicuous decrease of damping on cooling, accompanied by frequency hardening. (b) Real and (c) imaginary part of the complex permittivity, as obtained from the fits.

The anticipated lack of substantial temperature dependence of the IR reflectivity spectra of Ni_2CoTeO_6 and $NiCo_2TeO_6$ proves once more the resemblance among the four compounds. Naturally, the damping constants of the modes decrease on cooling. In a repeated manner as in Ni_3TeO_6 for the 310 cm^{-1} mode, the modes seen at 224 and 211 cm^{-1}, of Ni_2CoTeO_6 and

Table 3.4 Frequencies of the IR active modes in the Ni_2CoTeO_6 and $NiCo_2TeO_6$ ceramics at 10 K and Raman active modes at 4 K, as obtained by the fits of IR reflectivity with ε_∞ =4.6 and 4.1 respectively. The low frequency modes in the first lines come from the THz spectra. The damping constants and dielectric strength of the IR-active modes are also listed. The modes observed as weak in Raman spectra are marked by w in subscript.

Ni_2CoTeO_6				$NiCo_2TeO_6$			
Raman 4 K	IR 10 K			Raman 4 K	IR 10 K		
ω_{TO}(cm^{-1})	ω_{TO}(cm^{-1})	γ_{TO}(cm^{-1})	$\Delta\varepsilon$	ω_{TO}(cm^{-1})	ω_{TO}(cm^{-1})	γ_{TO}(cm^{-1})	$\Delta\varepsilon$
	16.87	1.5	0.02		6.6	1.1	0.02
	28.7	6.0	0.02		18.9	2.4	0.02
	31.0	2.5	0.006	21.9	23.1	5.3	0.05
	34.2	3.5	0.01		35.0	11.6	0.002
	60.0	38.3	0.06		43.7	7.0	0.007
				60.6	59.4	30.6	0.05
162.1	165.2	13.2	0.10	154.7			
	193.4	29.9	0.04	198.8	195.2	32.7	0.43
	212.3	10.0	0.41	213.5_w	211.4	15.8	0.98
	224.3	5.4	0.20		237.5	15.2	0.19
	244.4	15.4	0.16		241.4	23.9	0.23
278.5_w	269.6	12.4	0.52	254.9_w	255.1	22.7	0.83
	289.3	14.9	0.79		278.2	18.6	0.74
309.6_w	297.9	10.0	0.104	297.4	288.4	11.2	0.09
349.3_w	349.2	19.1	0.33	321.5	320.0	11.9	0.06
372.1	375.8	10.5	0.32		345.8	38.5	0.25
417.4	424.5	33.4	0.25	372.0	373.2	9.9	0.37
442.5	441.7	10.5	1.17	411.4	413.4	31.8	0.42
	446.8	6.7	0.19	430.5	428.8	12.2	1.12
481.5				473.2	433.1	6.3	0.19
505.1	513.0	16.7	0.42	500.3	504.1	19.1	0.36
536.9	523.7	13.4	0.28	526.2	512.7	5.3	0.01
	530.7	7.0	0.03		517.0	17.2	0.31
	583.7	19.8	0.08	561.4	573.0	29.2	0.06
644.0				578.9_w			
668.3_w				645.1			
683.2				685.5			
713.1_w				714.2_w			

$NiCo_2TeO_6$ respectively, exhibit a conspicuous frequency hardening, together with decrease of damping. The repeated phenomenon of mode intensity loss below T_N might again be related to coupling between the phonon and a lower energy magnon. As we will see below, both compounds evidence several spin excitations at the THz range, thus when the magnetic ordering occurs transfer of dielectric strength from the phonon to a spin excitation may take place.

Although the THz spectra will be analyzed later, here it is worth mentioning that the corresponding reflectivity values, as calculated by the complex index of refraction obtained from the THz spectra, coincide with the ones measured from the IR reflectivity experiment, and they are also plotted in Figure 3.34(a) (left and right), below 70 cm^{-1}.

A significant number of sharp modes can be seen in the temperature dependence of Raman spectra for both compounds (Figure 3.35). 14 modes are apparent in the Ni_2CoTeO_6 spectra, whereas 17 in the $NiCo_2TeO_6$, all listed in Table 3.4 in comparison with the IR modes. In an analogous way as mentioned for Ni_2MnTeO_6, it is not possible to resolve all Raman-active modes, due to the polycrystalline nature of the samples.

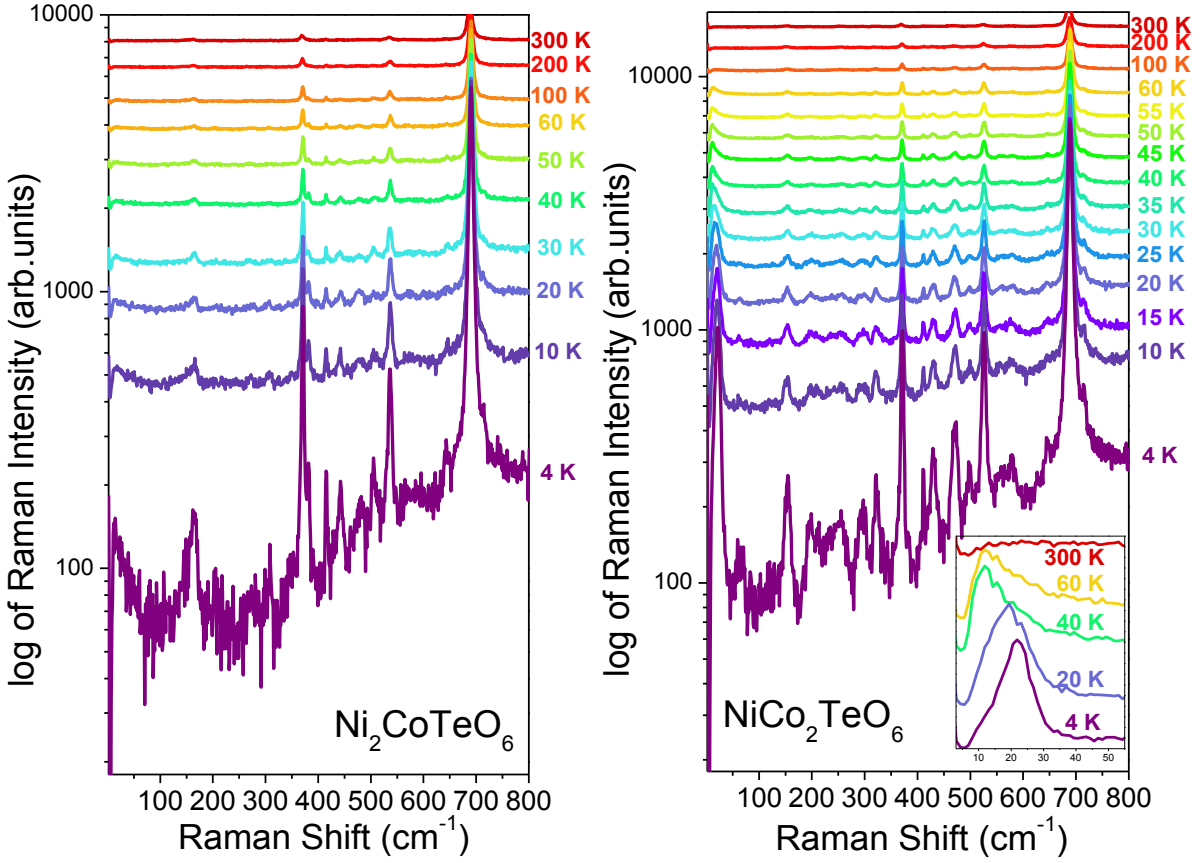

Figure 3.35 Temperature dependence of Raman spectra for (left) Ni_2CoTeO_6 and (right) $NiCo_2TeO_6$ ceramics. The inset in the left figure of $NiCo_2TeO_6$ shows the temperature evolution of a spin-wave below T_N.

$NiCo_2TeO_6$ shows two additional modes at the low-frequency range, at approximately 22 and 60 cm^{-1}, which develop below the AFM transition, therefore of magnetic origin. The one at 22 cm^{-1} is astonishingly strong (shown in the inset of Figure 3.35(right)). As we will see below, both modes are also observed in the THz spectra.

The most exciting finding from the whole family of Co,Mn-doped Ni_3TeO_6 is unveiled by the time-domain THz spectroscopy of the Co-doped ceramics. The temperature dependence of the

complex index of refraction in the THz range is shown in Figure 3.36 for (left) Ni_2CoTeO_6 and (right) $NiCo_2TeO_6$ ceramics of ~1.9 mm thickness. The spectra were measured from 300 down to 5 K. An initial decrease of the real part of the index of refraction on cooling is observed, followed by a pronounced development of two modes below T_N for both Ni_2CoTeO_6 (T_N≈52 K) and $NiCo_2TeO_6$ (T_N≈49 K). All excitations sharpen and harden on cooling, with evident splitting for the broader ones. The spectra were fitted simultaneously with the IR reflectivity spectra, and the corresponding frequencies, damping constants and mode strengths are listed in Table 3.4.

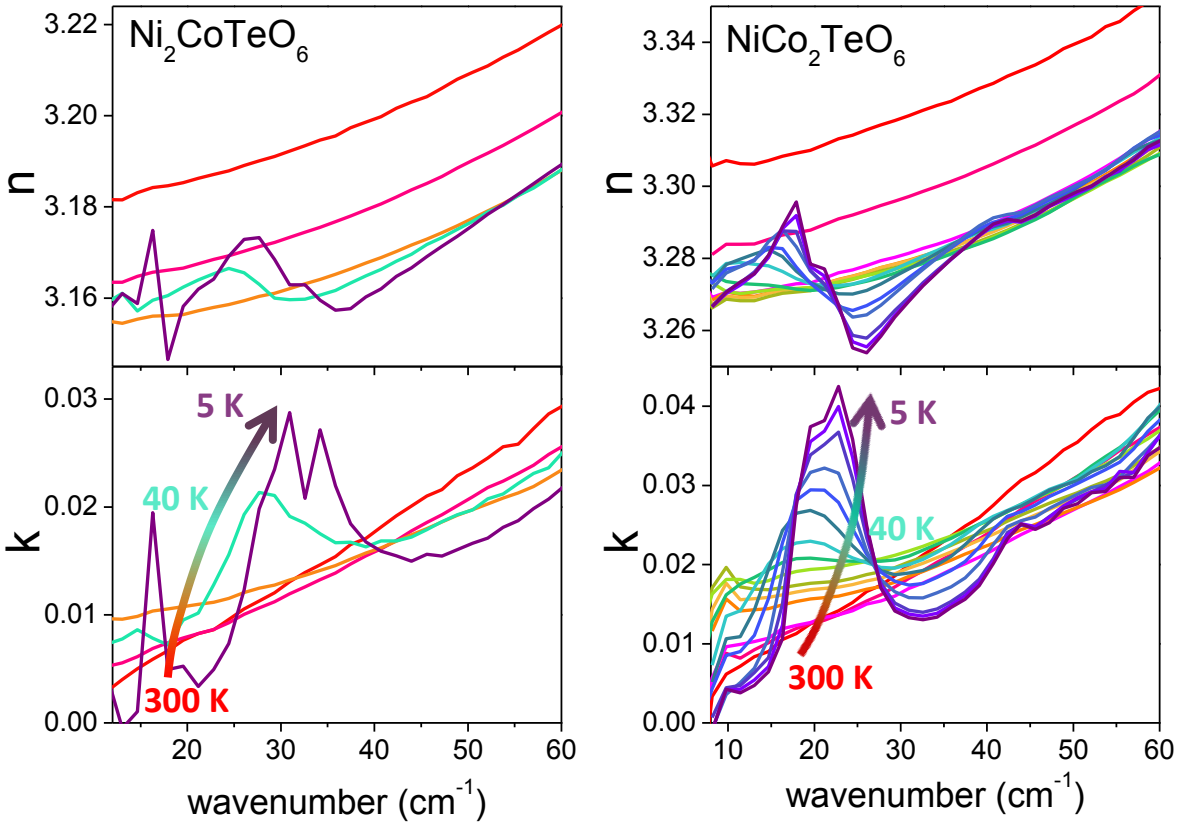

Figure 3.36 Temperature dependence of the real and imaginary parts of the index of refraction for (left) Ni_2CoTeO_6 and (right) $NiCo_2TeO_6$ for selected temperatures from 5 to 300 K. At least five spin excitations appear below T_N for both compounds.

Ni_2CoTeO_6 displays 5 modes at the lowest temperature of 5 K, whereas $NiCo_2TeO_6$ presents 6. The rapid development of these modes below T_N, especially the sharp ones, suggests that they correspond to spin excitations. As mentioned above, the 22 cm^{-1} mode of the latter sample is simultaneously seen in the Raman spectra, implying a polar character, therefore it is assigned as an electromagnon. The broader mode of 60 cm^{-1} is also seen in Raman, but it most probably corresponds to two-magnon scattering.

Time-domain THz measurements at the Voigt configuration with $\boldsymbol{H}_{ext} \perp \boldsymbol{E}^{\omega}$ up to 7 T and at temperatures of 30 and 5 K are presented in Figure 3.37. Both compounds show magnon tuning

at external magnetic field, since they exhibit peak sharpening and frequency shifts. The magnetic field dependence of the spin-wave frequencies, as obtained by the fits, is summarized in Figure 3.38 for both compounds ((left) and (right)). In Ni_2CoTeO_6, he sharp mode seen at 30 K around 17 cm^{-1} (0 T), softens down to 14 cm^{-1} at 7 T, whereas the higher-frequency mode near 30 cm^{-1} is less sensitive on $\boldsymbol{H}_{ext}$. The sharpening and softening of the latter more is even more pronounced at 5 K (Figure 3.37(c)). However, even more phenomenal is the behavior of the magnons at the presence of external magnetic field for $NiCo_2TeO_6$. At 30 K (Figure 3.37(b)) the two strongest modes of 7 and 23 cm^{-1} at 0 T, harden to 13 and 28 cm^{-1} respectively, with rising field up to 7 T.

Continuing with the staggering spin excitations in $NiCo_2TeO_6$, at 5 K the spectra are much richer. The magnon frequency modification by external magnetic field is best seen in Figure 3.38(right). Remarkable are the bold steps that at least four of the excitations manifest at approximately 3 T, close to the spin-flop transition, as defined by the magnetization measurements (Figure 3.32(b) and (d)). Two new modes seem to appear at around 30 cm^{-1} above 3 T. These new excitations might also correspond to splitting of the neighboring single mode, triggered by the spin-flop transition.

The mode 23 cm^{-1} at 0 T, which as mentioned above was also seen by Raman spectroscopy, shows a strong magnetic field dependence. Such behavior, in combination with the concurrent detection of the mode by both THz and Raman spectroscopies, suggests coupling of the spin-wave to a polar mode. Hence, the evidence strongly suggests that the mode in question is an electromagnon.

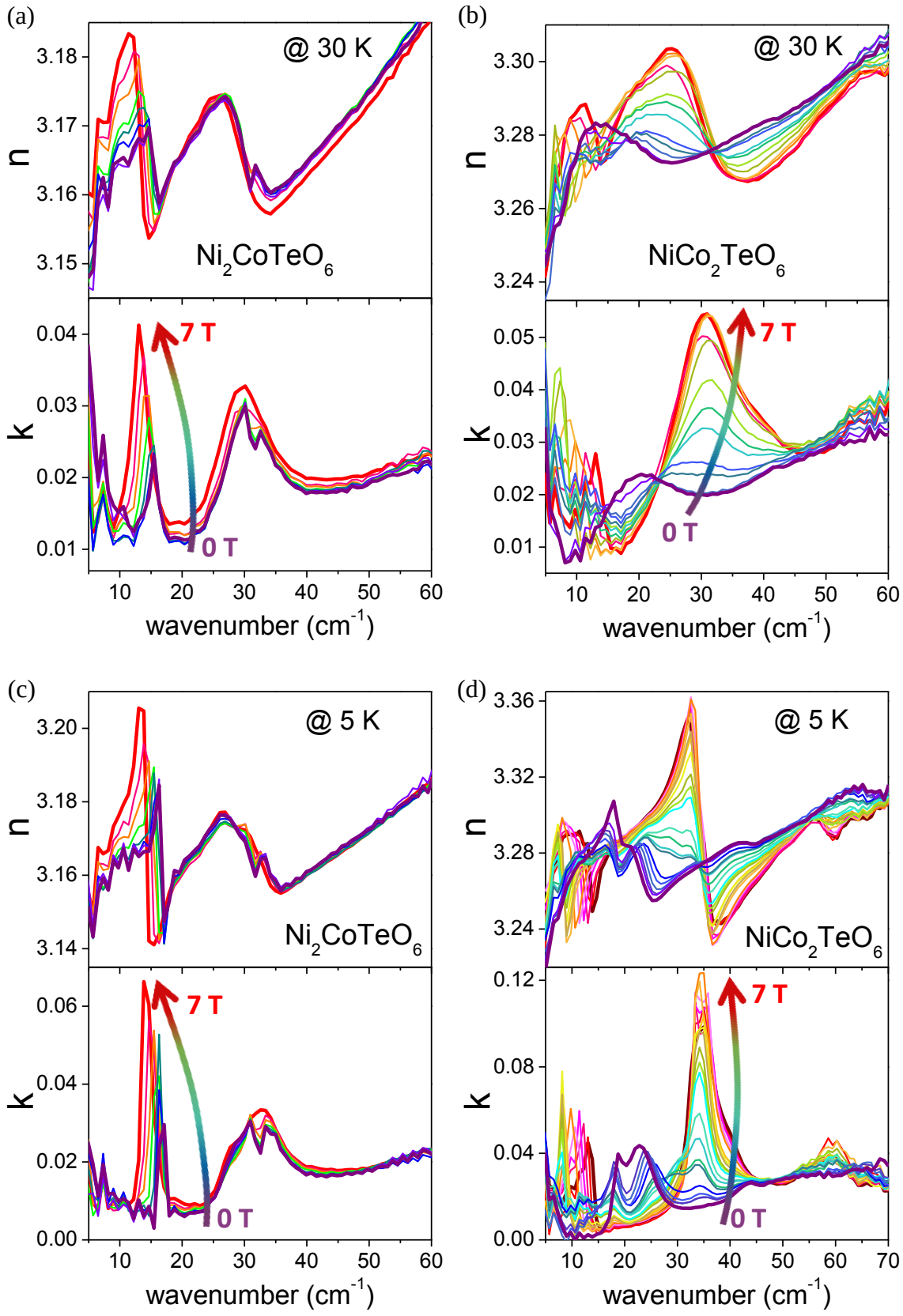

Figure 3.37 Magnetic field dependence of the complex index of refraction at (a), (b) 30 K, and (c), (d) 5 K of Ni_2CoTeO_6 and $NiCo_2TeO_6$ respectively, as obtained by the time-domain THz spectra, with $\boldsymbol{H}_{ext} \perp \boldsymbol{E}^{\omega}$ and up to 7 T.

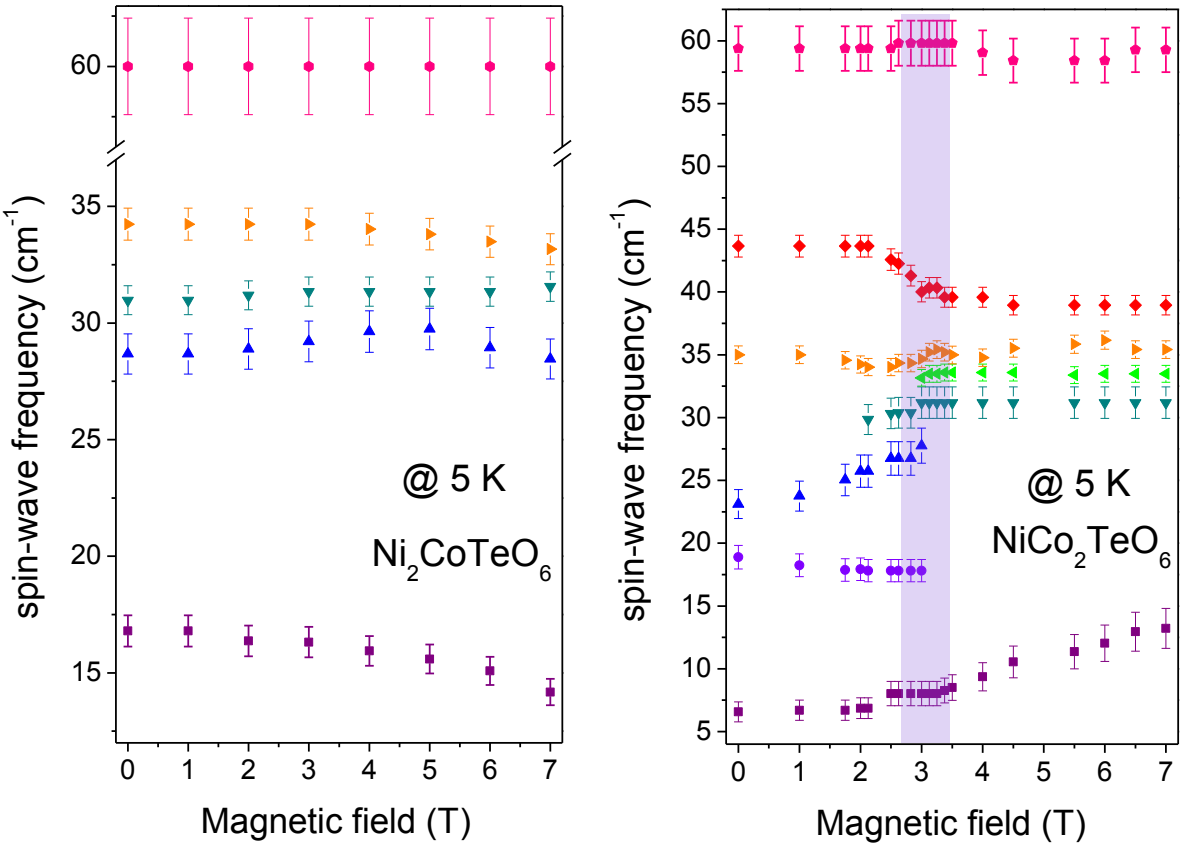

Figure 3.38 Magnetic field dependence of spin-wave frequency for (left) Ni_2CoTeO_6 and (right) $NiCo_2TeO_6$, at 5 K. In the latter, the spin-flop transition is clearly seen at approximately 3 T (designated by the violet stripe), by the steps on the magnon branches, as well as both the appearance of new modes and extinction of ones present in the low-field phase.

3.3.3.4 Discussion

The novel Co-doped Ni_3TeO_6 compounds, Ni_2CoTeO_6 and $NiCo_2TeO_6$, were successfully grown for the first time, in form of single crystals and ceramics. Both compounds, like the Mn-doped Ni_3TeO_6 case from section 3.3.2, preserve the non-centrosymmetric *R*3 space group symmetry of the pure Ni_3TeO_6,[234] as confirmed by PND. The crystal symmetry was also supported by the observation of all 18 predicted vibrational modes by IR and Raman spectroscopies. The magnetic ordering appearing below 55 (52) and 52 (49) K (single crystals (ceramics)), is accompanied by a FE transition, indicated by the dielectric anomaly (Figure 3.33), suggesting multiferroicity for both compounds.

In contradiction to the magnetic ordering in Ni_3TeO_6 and Ni_2MnTeO_6, both Co-doped compounds present *ab*-easy-plane magnetization, and not along the *c*-axis. Hysteretic spin-flop transitions were observed in both compounds, near 7 T (Ni_2CoTeO_6) and 3.5 T ($NiCo_2TeO_6$). However, Ni_3TeO_6 and Ni_2MnTeO_6 did not show any hysteretic behavior, apart from the Ni_2MnTeO_6 low-field (below 0.3 T) magnetic hysteresis of unknown origin (possibly due to

impurities in the polycrystalline sample). Further investigation by PND is required to gain a better insight in the complex magnetic structure of the new compositions. Especially for the Co-rich compound of $NiCo_2TeO_6$, an convoluted magnetic behavior is plainly foreseen due to the intriguing magnetism of Co_3TeO_6.[257,259,263]

The static permittivity value suggested by the IR and THz measurements corresponds to approximately 10, close to the one reported for Ni_3TeO_6 at the radio-range.[63] However, the permittivity spectra of $NiCo_2TeO_6$ at 0.1 MHz (Figure 3.33) reveal higher value of ~20, most probably due to Maxwell-Wagner contribution to permittivity, as a consequence of interlayer barriers at the grain boundaries.

Reoccurrence of the dielectric strength transfer from a phonon mode to a lower-frequency magnon in Ni_3-xCo_xTeO_6 (not seen in Ni_2MnTO_6), suggests the coupling between spin and lattice excitations. Similar coupling of the polar phonon with electromagnons was observed also in Ni_3TeO_6.[144,243]

The most fascinating results of these novel multiferroics are the spin excitations revealed by THz and Raman spectroscopies. Five and six low-frequency (THz-range) excitations are seen for Ni_2CoTeO_6 and $NiCo_2TeO_6$ respectively, at 5 K and at 0 T, most probably of magnetic origin, since they develop below T_N. Most spin-excitations present strong dependence on external magnetic field, with clear modifications at the spin-flop transition of ~3 T for the case of $NiCo_2TeO_6$. The 23 cm^{-1} in the latter compound is also seen in Raman spectra, thus assigned as electromagnon. Other spin-waves not observed in Raman spectra imply a pure magnonic character (non-polar). The discrepancies in the T_N values observed by the Raman spectroscopy could be explained by thermos-lag effects, laser-heating, and/or random crystallite orientation in the polycrystalline samples. Finally, the observed excitations cannot correspond to crystal field splitting due to the possible presence of various Co geometry coordinations (octahedral, tetrahedral, etc.), since the 3*d*-related crystal field splitting values lie in the range of UV and visible,[268] whereas the 4*f*-related splitting reaches down to the FIR range.[269]

As mentioned for the previous cases of the $Ni_{3-x}B_xTeO_6$ (B= Mn, Co) family, large enough single crystals are required for more extensive THz measurements, in order to resolve the relation between crystal symmetry and magnon propagation. Even more optimal would be to study directional dichroism. Finally, single crystals could also serve for performing pyrocurrent measurements at external magnetic field, in order to examine the static magnetoelectric coupling, and compare it with the colossal magnetoelectric effect observed in Ni_3TeO_6.

3.3.3.5 Conclusions

Co-substitution of Ni in the Ni_3TeO_6 preserves the multiferroic properties of the parent structure, while exhibiting enhanced dynamical magnetoelectric coupling. The non-centrosymmetric *R*3 space group is maintained at least up to RT for both Ni_2CoTeO_6 and $NiCo_2TeO_6$ compounds, even though Co_3TeO_6 has monoclinic non-polar structure with the space group *C*2/c. The FE phase transition is magnetically driven, as for the Mn-doped and pure Ni_3TeO_6, displaying dielectric anomalies at T_N. Magnetic ordering develops approximately at the same temperature range as the undoped Ni_3TeO_6, in contradiction to the Mn-doped case.

Both compounds demonstrate numerous spin-excitations below T_N in the THz range, which are markedly tuned by external magnetic field. The Co-rich compound of $NiCo_2TeO_6$ prevails, manifesting six magnons, by which two are simultaneously seen by Raman spectroscopy, thus assigned as electromagnons.

3.3.4 **A comparative analysis of Ni-based Tellurides**

The static (colossal)[63] and dynamical[144] magnetoelectric effects of Ni_3TeO_6 prompted the synthesis and study of compounds with Ni-substitution by Mn and Co. Here, the results presented in sections 3.3.1, 3.3.2 and 3.3.3 are summarized, in an attempt to compare and understand the role of Mn- and Co-doping in Ni_3TeO_6. The main findings of the Ni-based Telluride family are presented in Table 3.5.

Mn and Co-doping does not affect the parent non-centrosymmetric *R*3 crystal symmetry of Ni_3TeO_6,[234] which is maintained at least up to RT. As a reminder, the pure Mn_3TeO_6 and Co_3TeO_6 compounds possess the non-polar rhombohedral $R\bar{3}$[258] and monoclinic $C2/c$,[259] respectively.

All compounds present an AFM phase transition, accompanied by a FE one, suggesting spin-induced ferroelectricity. The critical temperatures do not differ significantly among the compounds, apart from the impressive ~20 K enhancement in Ni_2MnTeO_6, which presents $T_N \approx 70$ K. The slight inconsistency among the reported values of T_N possibly originates in the diverse experimental methods used for their determination, as well as the different forms of samples (single crystal and ceramics).

Table 3.5 Comparison of multiferroic features of the Ni-based Telluride family. $T_{N,M}$ and $T_{N,\varepsilon'}$ correspond to the T_N values obtained from the magnetization and permittivity measurements, respectively. The subscripts in the T_N values of Ni_2MnTeO_6 single crystal designate the type of experimental method used for its determination. Previously reported results of Ni_3TeO_6 are also included in the first column.

	Ni_3TeO_6	Ni_2MnTeO_6	Ni_2CoTeO_6	$NiCo_2TeO_6$
crystal symmetry	***R*3**[234]	***R*3**	***R*3**	***R*3**
T_N (single crystal)	**53 K**[63]	**73 K_{PND}** **67 K_χ**	**55 K**	**52 K**
$T_{N,M}$ (ceramics)	-	**70 K**	**52 K**	**49 K**
$T_{N,\varepsilon'}$ (ceramics)	**53 K**[63]	**67 K**	**53 K**	**47 K**
$H_{spin\text{-}flop}$	**8 T**[63]	**5 T**	**7 T**	**3 T**
magnons	**2**[144]	**2**	**4**	**6**
electromagnons	**2**[144]	-	-	**2**

The comparison of the magnetization and permittivity curves as a function of temperature is shown in Figure 3.39(left). Magnetization is plotted in the left-Y axis and permittivity in the

right. The colored stripes designate the multiferroic phase transitions for each compound. The possible impurity of Mn_3TeO_6 is also included.

Ni_3TeO_6 displays a rich magnetic phase diagram, with numerous magnetic phase transitions,[239,243] as mentioned in section 3.3.1.1. Apart from the paramagnetic to AFM one, a magnetically induced spin-flop transition occurs at ~8 T, and metamagnetic transition was observed at 52 T.[239] Analogously, the rest of Ni-based Tellurides discussed here undergo spin-flop transitions, however at slightly different magnetic fields, 5, 7 and 3 T for Ni_2MnTeO_6, Ni_2CoTeO_6 and $NiCo_2TeO_6$ respectively. The spin-flop transition is only slightly pronounced in Ni_2MnTeO_6, which in addition presents a second anomaly at 23 K, most possibly due to the presence of Mn_3TeO_6. Here, it is essential to mention that Mn_3TeO_6, although holding the non-polar $R\bar{3}$ symmetry, may demonstrate FE anomaly in permittivity, as it was reported for Co_3TeO_6.[257,262]

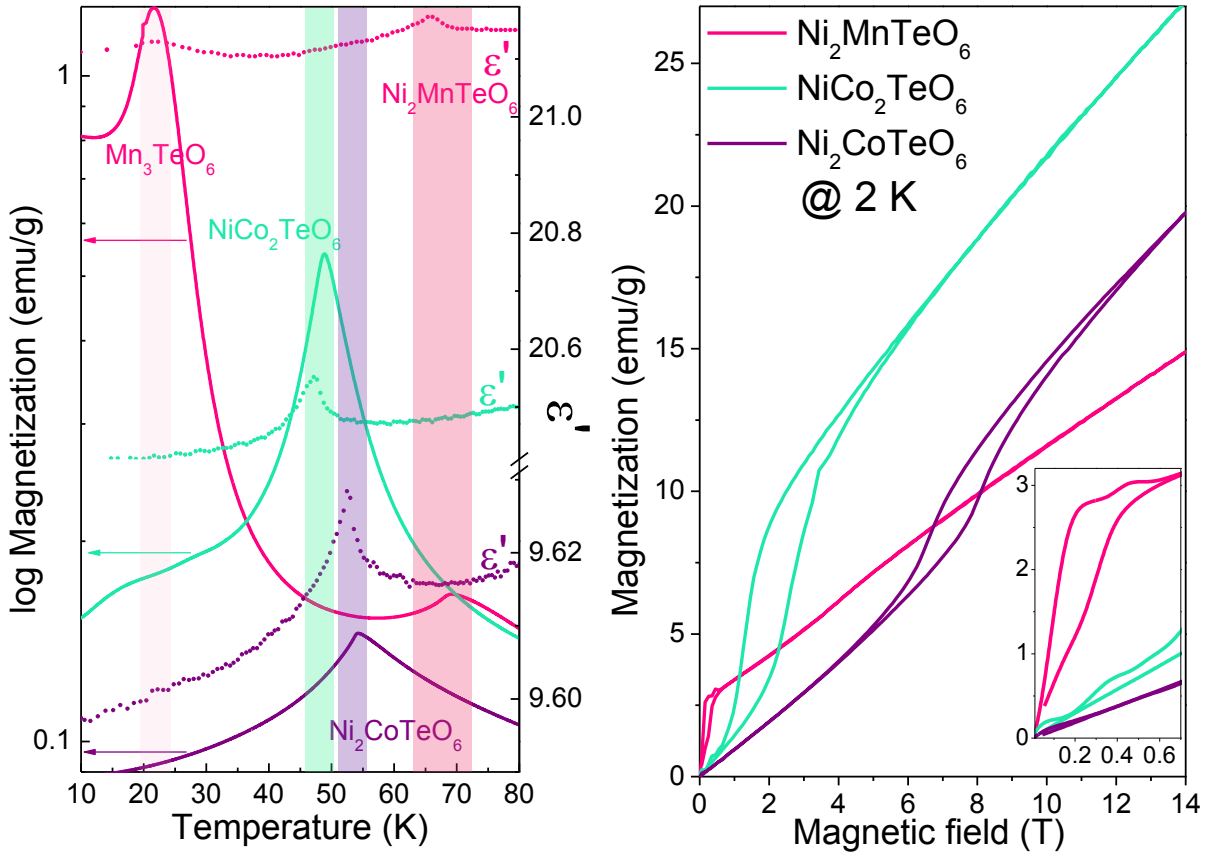

Figure 3.39 Comparison of (left) temperature dependence of magnetization and permittivity, and (right) magnetic field dependence of magnetization of the Mn- and Co-doped Ni_3TeO_6.

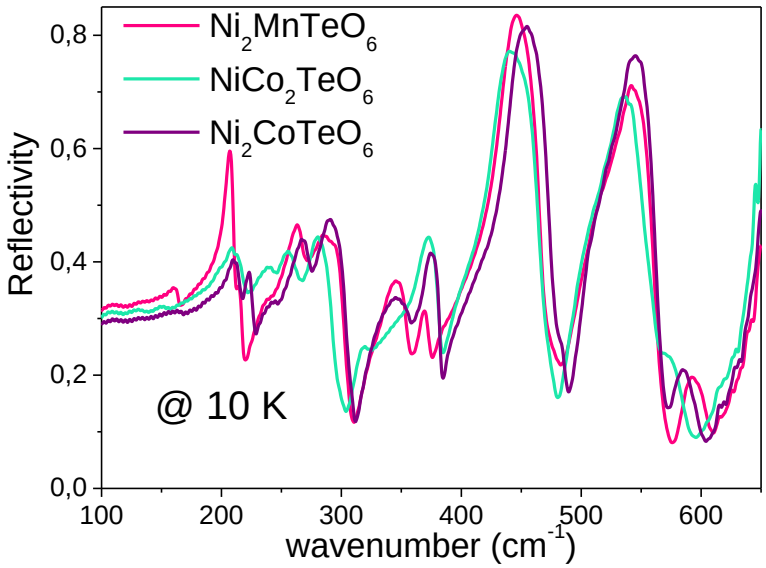

Figure 3.40 IR reflectivity spectra of Ni_2MnTeO_6, Ni_2CoTeO_6 and $NiCo_2TeO_6$ ceramics, obtained at 10 K.

Lattice excitations studied by IR and Raman spectroscopies reveal all 18 modes predicted by factor group analysis for the *R*3 space group (9 $E(x,y,x^2-y^2,xy,xz,yz)$ and 9 $A(x^2+y^2,z^2,z)$). As seen in Figure 3.40, the spectra do not differ substantially, apart from slight variations in frequency and dielectric strength. Ni_3TeO_6 spectra presented earlier in section 3.3.1.3 were not included for comparison due to the discrepancy in the values of reflectivity, result of the highly porous Ni_3TeO_6 ceramics. The phonon similarities among the compounds can also be seen in the Raman spectra in Figure 3.41(left).

In order to investigate the dynamical magnetoelectric coupling, a combination of spectroscopic techniques was used: FTIR, time-domain THz and Raman. Two electromagnons were observed in Ni_3TeO_6 and $NiCo_2TeO_6$. These spin-excitations were seen simultaneously in THz and Raman spectra, appearing below the AFM phase transition (Figure 3.41). Spin ordering results in coupling of the spin-waves to the lattice, attributing a polar character to the magnons. A clear dependence on external magnetic field, with frequency shifts and intensity variations, was recorded in the THz spectra. Especially for the case of $NiCoTeO_6$, the spin-flop transition at ~3 T was evident by steps and splittings of magnon branches (Figure 3.38(right)).

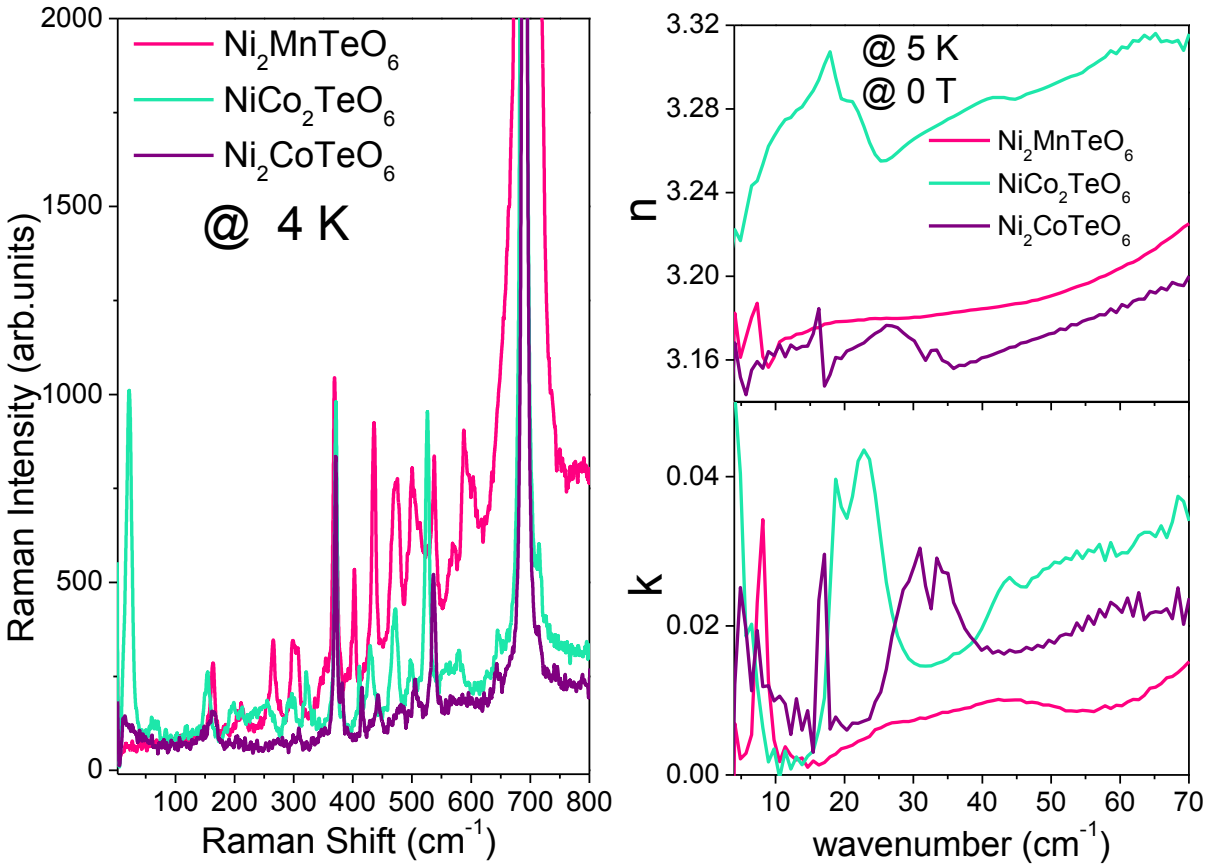

Figure 3.41 (left) Raman and (right) time-domain THz spectra of Ni_2MnTeO_6, Ni_2CoTeO_6 and $NiCo_2TeO_6$ ceramics, obtained at 4 and 5 K respectively. The THz spectra are at the absence of external magnetic field.

Even though Ni_2MnTeO_6 and Ni_2CoTeO_6 did not necessarily present dynamical magnetoelectric coupling, several spin excitations were observed in the THz range (Figure 3.41(right)). Table 3.5 summarizes the number of observed magnons and electromagnons for all compounds. However, the fact that electromagnons were not revealed in the spectra does not exclude the possibility of their existence, because the excitations lie almost at the edge of the experimental frequency range, and the polycrystalline nature of the samples restricts thorough symmetry-based investigation.

In short, it is evident that Mn-doping in Ni_3TeO_6 results in increase of the AFM phase transition temperature, and consequently the FE one, whereas Co-doping does not influence T_N, but enhances the spin dynamics, inducing a more pronounced dynamical magnetoelectric coupling.

Chapter 4

Conclusions

4 Conclusions

The scientific significance of dynamical magnetoelectric coupling, combined with the eminent implication of its technological applications, prompted the investigation of spin and lattice excitations of a series of materials. The main findings are summarized here. Below, a selection of figures with the most important experimental results for each material case is presented.

An extensive study of IR vibrational spectra of $BiFeO_3$ ceramics and an epitaxial thin film was conducted. The phonons in a $BiFeO_3/TbScO_3$ epitaxial thin film were studied for the first time, showing parameters similar to those in $BiFeO_3$ single crystals. In the thin film, an additional weak excitation near 600 cm^{-1} was detected, which apparently corresponds to a peak in the magnon density of states possibly activated due to the incommensurately modulated magnetic structure of $BiFeO_3$. Finally, two new IR-active modes near 55 cm^{-1} were observed at 5 K, which correspond to spin excitations previously theoretically predicted.

The novel double perovskite Pb_2MnTeO_6 was successfully prepared for the first time. Pb_2MnTeO_6 undergoes an antiferromagnetic phase transition at ~20 K, and a first-order structural phase transition (I2/m to C2/c) at ~120 K. Abrupt changes at T_C in both IR and Raman spectra confirm first-order character of the phase transition, seen as well in thermal capacity and dielectric permittivity measurements. Such behavior, suggests a possible antiferroelectric (AFE) character, however no AFE loops were detected. Thus, Pb_2MnTeO_6 belongs to a rare group of antipolar antiferromagnets with a potential large magnetoelectric coupling.

The spin-order-induced FE antiferromagnet Ni_3TeO_6 exhibits non-hysteretic colossal magnetoelectric coupling. Spin and lattice excitations in Ni_3TeO_6 were investigated by a combination of infrared, Raman and THz spectroscopies. Two spin excitations (near 13 and 35 cm^{-1}) were observed simultaneously in Raman and time-domain THz spectra below the Néel temperature T_N=53 K. These excitations correspond to electromagnons.

The static (colossal) and dynamical magnetoelectric effects of Ni_3TeO_6 prompted the synthesis and study of compounds with Ni-substitution by Mn and Co. All $Ni_{3-x}B_xTeO_6$ (B=Mn, Co) compounds present the non-centrosymmetric *R*3 space group symmetry, collinear antiferromagnetic spin structure, and spin-induced electric polarization below T_N. Mn-doping results in increase of the Néel temperature, whereas Co-doping in decrease of the magnetic field value of the spin-flop transition, at which the magnetoelectric coupling enhances. Spin excitations were observed in all compounds. In addition to the pure magnons, Ni_3TeO_6 and $NiCo_2TeO_6$ also display electromagnons.

$BiFeO_3$

2 new IR-active spin excitations

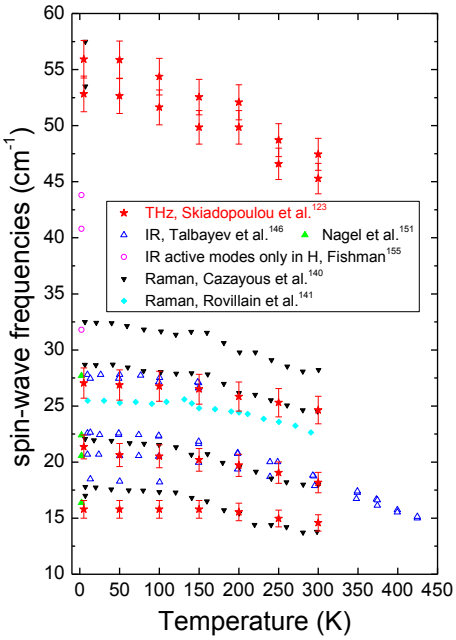

Pb_2MnTeO_6

rare case of antipolar antiferromagnet

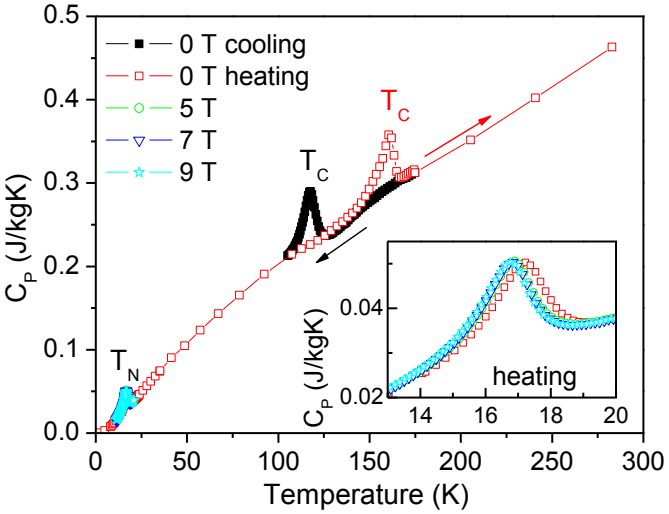

Ni-based Tellurides

Ni_3TeO_6

electromagnons

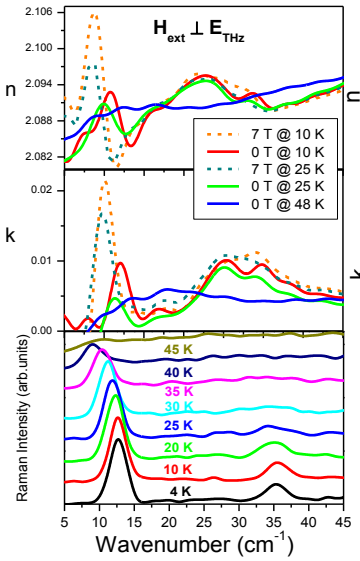

$NiCo_2TeO_6$

electromagnons

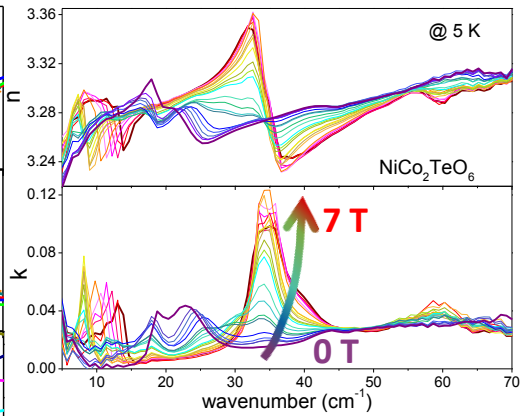

$Ni_{3-x}B_xTeO_6$ (B = Mn, Co)

Mn-doping: ↑ T_N

Co-doping: ↓ H_{sf}

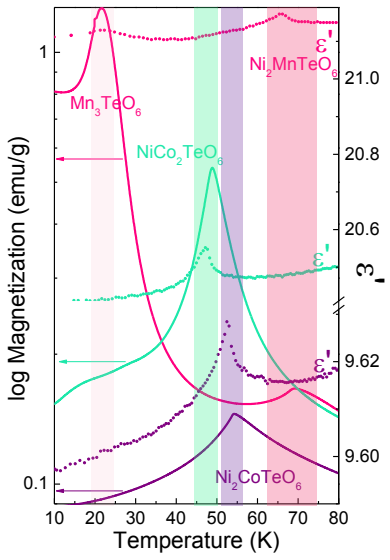

Bibliography

[1] M. Fiebig, J. Phys. D. Appl. Phys. **38**, R123 (2005).
[2] W. Eerenstein, N.D. Mathur, and J.F. Scott, Nature **442**, 759 (2006).
[3] R. Ramesh and N.A. Spaldin, Nat. Mater. **6**, 21 (2007).
[4] K.F. Wang, J.-M. Liu, and Z.F. Ren, Adv. Phys. **58**, 321 (2009).
[5] S. Dong, J.-M. Liu, S.-W. Cheong, and Z. Ren, Adv. Phys. **64**, 519 (2015).
[6] D.I. Khomskii, in *Multiferroic Mater. Prop. Tech. Appl.*, edited by J. Wang (Taylor & Francis, 2017), pp. 3–4.
[7] N.A. Spaldin and M. Fiebig, Science **309**, 391 (2005).
[8] W.C. Röntgen, Ann. Phys. **35**, 264 (1888).
[9] N.A. Hill, J. Phys. Chem. B **104**, 6694 (2000).
[10] D.I. Khomskii, in *Proc. Am. Phys. Soc.* (Seattle, 2001).
[11] P. Curie, J. Phys. Théorique Appliquée **3**, 393 (1894).
[12] H.A. Wilson, Philos. Trans. R. Soc. London A Math. Phys. Eng. Sci. **204**, (1905).
[13] P. Debye, Zeitschrift Für Phys. **36**, 300 (1926).
[14] I.E. Dzyaloshinskii, Sov. Phys. JETP **10**, 628 (1960).
[15] D.N. Astrov, JETP **11**, 708 (1960).
[16] R.M. Bozorth, *Ferromagnetism* (Van Nostrand, New York, 1951).
[17] E. Schrödinger, Sitzungsberichte Der Kais. Akad. Der Wissenschaften Wien. Math. Klasse **121**, 1937 (1912).
[18] K. Aizu, Phys. Rev. **146**, 423 (1966).
[19] K. Aizu, J. Phys. Soc. Japan **23**, 794 (1967).
[20] K. Aizu, J. Phys. Soc. Japan **27**, 387 (1969).
[21] K. Aizu, Phys. Rev. B **2**, 754 (1970).
[22] R.E. Newnham, Am. Mineral. **59**, 906 (1974).
[23] R.E. Newnham and L.E. Cross, Ferroelectrics **10**, 269 (1976).
[24] E. Ascher, H. Rieder, H. Schmid, and H. Stössel, J. Appl. Phys. **37**, 1404 (1966).
[25] H. Schmid, Ferroelectrics **162**, 317 (1994).
[26] S.-W. Cheong and M. Mostovoy, Nat. Mater. **6**, 13 (2007).
[27] D. Khomskii, Physics (College. Park. Md). **2**, 20 (2009).
[28] Y. Wang, J.M. Hu, Y.H. Lin, and C.W. Nan, NPG Asia Mater. **2**, 61 (2010).
[29] L.W. Martin and R. Ramesh, Acta Mater. **60**, 2449 (2012).
[30] L.D. Landau and E.M. Lifshitz, *Statistical Physics*, 3rd ed. (Pergamon Press, 1980).
[31] W.F. Brown, R.M. Hornreich, and S. Shtrikman, Phys. Rev. **168**, 574 (1968).
[32] B.K. Ponomarev, S.A. Ivanov, Y.F. Popov, V.D. Negrii, and B.S. Red'Kin, Ferroelectrics **161**, 43 (1994).
[33] C. Kadlec, V. Goian, K.Z. Rushchanskii, P. Kužel, M. Ležaic, K. Kohn, R.V. Pisarev, and S. Kamba, Phys. Rev. B **84**, 174120 (2011).
[34] I. Dzyaloshinsky, J. Phys. Chem. Solids **4**, 241 (1958).
[35] T. Moriya, Phys. Rev. **120**, 91 (1960).
[36] H. Katsura, N. Nagaosa, and A. V. Balatsky, Phys. Rev. Lett. **95**, 57205 (2005).
[37] I.A. Sergienko and E. Dagotto, Phys. Rev. B **73**, 94434 (2006).
[38] T. Arima, J. Phys. Soc. Japan **76**, 73702 (2007).
[39] Y. Tokura and N. Kida, Philos. Trans. R. Soc. London A Math. Phys. Eng. Sci. **369**, (2011).
[40] I.A. Sergienko, C. Şen, and E. Dagotto, Phys. Rev. Lett. **97**, 227204 (2006).
[41] Y.J. Choi, H.T. Yi, S. Lee, Q. Huang, V. Kiryukhin, and S.-W. Cheong, Phys. Rev. Lett. **100**, 47601 (2008).
[42] B. Lorenz, Y.-Q. Wang, and C.-W. Chu, Phys. Rev. B **76**, 104405 (2007).
[43] N. Lee, Y.J. Choi, M. Ramazanoglu, W. Ratcliff, V. Kiryukhin, and S.-W. Cheong, Phys. Rev. B **84**, 20101 (2011).
[44] N.A. Hill, (2000).
[45] H. Sakai, J. Fujioka, T. Fukuda, D. Okuyama, D. Hashizume, F. Kagawa, H. Nakao, Y.

Murakami, T. Arima, A.Q.R. Baron, Y. Taguchi, and Y. Tokura, Phys. Rev. Lett. **107**, 137601 (2011).
[46] P. Ravindran, R. Vidya, A. Kjekshus, H. Fjellvåg, and O. Eriksson, Phys. Rev. B **74**, 224412 (2006).
[47] D. V. Efremov, J. van den Brink, and D.I. Khomskii, Nat. Mater. **3**, 853 (2004).
[48] N. Hur, S. Park, P.A. Sharma, J.S. Ahn, S. Guha, and S.-W. Cheong, Nature **429**, 392 (2004).
[49] N. Ikeda, H. Ohsumi, K. Ohwada, K. Ishii, T. Inami, K. Kakurai, Y. Murakami, K. Yoshii, S. Mori, Y. Horibe, and H. Kitô, Nature **436**, 1136 (2005).
[50] B.B. Van Aken, T.T.M. Palstra, A. Filippetti, and N.A. Spaldin, Nat. Mater. **3**, 164 (2004).
[51] N. Kida, Y. Takahashi, J.S. Lee, R. Shimano, Y. Yamasaki, Y. Kaneko, S. Miyahara, N. Furukawa, T. Arima, and Y. Tokura, J. Opt. Soc. Am. B **26**, A35 (2009).
[52] A.M. Shuvaev, A.A. Mukhin, and A. Pimenov, J. Phys. Condens. Matter **23**, 113201 (2011).
[53] I. Sosnowska, T.P. Neumaier, and E. Steichele, J. Phys. C Solid State Phys. **15**, 4835 (1982).
[54] D. Lebeugle, D. Colson, A. Forget, M. Viret, A.M. Bataille, and A. Gukasov, Phys. Rev. Lett. **100**, 227602 (2008).
[55] Y. Yamasaki, S. Miyasaka, Y. Kaneko, J.-P. He, T. Arima, and Y. Tokura, Phys. Rev. Lett. **96**, 207204 (2006).
[56] T. Arima, Y. Yamasaki, T. Goto, S. Iguchi, K. Ohgushi, S. Miyasaka, and Y. Tokura, J. Phys. Soc. Japan **76**, 23602 (2007).
[57] T. Kimura, Annu. Rev. Condens. Matter Phys. **3**, 93 (2012).
[58] R.C. Pullar, Prog. Mater. Sci. **57**, 1191 (2012).
[59] J.H. Lee and R.S. Fishman, Phys. Rev. Lett. **115**, 207203 (2015).
[60] Y. Tokunaga, S. Iguchi, T. Arima, and Y. Tokura, Phys. Rev. Lett. **101**, 97205 (2008).
[61] C.Y. Ma, S. Dong, P.X. Zhou, Z.Z. Du, M.F. Liu, H.M. Liu, Z.B. Yan, J.-M. Liu, D.I. Khomskii, L.H. Tjeng, M.A. Señarís-Rodríguez, C.D. Batista, M. Wuttig, and R. Ramesh, Phys. Chem. Chem. Phys. **17**, 20961 (2015).
[62] H.Y. Zhou, H.J. Zhao, W.Q. Zhang, and X.M. Chen, Appl. Phys. Lett. **106**, 152901 (2015).
[63] Y.S. Oh, S. Artyukhin, J.J. Yang, V. Zapf, J.W. Kim, D. Vanderbilt, and S.-W. Cheong, Nat Commun **5**, 3201 (2014).
[64] R.M. Hornreich and S. Shtrikman, Phys. Rev. **171**, 1065 (1968).
[65] G.L.J.A. Rikken, C. Strohm, and P. Wyder, Phys. Rev. Lett. **89**, 133005 (2002).
[66] M. Mochizuki, N. Furukawa, and N. Nagaosa, Phys. Rev. Lett. **104**, 177206 (2010).
[67] I. Kézsmárki, N. Kida, H. Murakawa, S. Bordács, Y. Onose, and Y. Tokura, Phys. Rev. Lett. **106**, 57403 (2011).
[68] Y. Takahashi, R. Shimano, Y. Kaneko, H. Murakawa, and Y. Tokura, Nat. Phys. **8**, 121 (2011).
[69] I. Kézsmárki, D. Szaller, S. Bordács, V. Kocsis, Y. Tokunaga, Y. Taguchi, H. Murakawa, Y. Tokura, H. Engelkamp, T. Rõõm, and U. Nagel, Nat. Commun. **5**, (2014).
[70] Y. Tokura, S. Shinichiro, and N. Naoto, Reports Prog. Phys. **77**, 76501 (2014).
[71] D.M. Juraschek, M. Fechner, A. V. Balatsky, and N.A. Spaldin, Phys. Rev. Mater. **1**, 14401 (2017).
[72] J.C. Lashley, M.F. Hundley, B. Mihaila, J.L. Smith, C.P. Opeil, T.R. Finlayson, R.A. Fisher, and N. Hur, Appl. Phys. Lett. **90**, 52910 (2007).
[73] I.E. Dzyaloshinskii and D.L. Mills, Philos. Mag. **89**, 2079 (2009).
[74] J.F. Scott and J. F., Reports Prog. Phys. **42**, 1055 (1979).
[75] C.J. Fennie, Phys. Rev. Lett. **100**, 167203 (2008).
[76] W.F. Brown, S. Shtrikman, and D. Treves, J. Appl. Phys. **34**, 1233 (1963).
[77] B.B. Krichevtsov, V. V. Pavlov, R. V. Pisarev, and V.N. Gridnev, Phys. Rev. Lett. **76**, 4628 (1996).
[78] J.H. Jung, M. Matsubara, T. Arima, J.P. He, Y. Kaneko, and Y. Tokura, Phys. Rev. Lett. **93**, 37403 (2004).
[79] M. Kubota, T. Arima, Y. Kaneko, J. He, X. Yu, and Y. Tokura, Phys. Rev. Lett. **92**, 137401 (2004).
[80] Y. Takahashi, Y. Yamasaki, and Y. Tokura, Phys. Rev. Lett. **111**, 37204 (2013).
[81] D. Szaller, S. Bordács, V. Kocsis, T. Rõõm, U. Nagel, and I. Kézsmárki, Phys. Rev. B **89**, 184419 (2014).

[82] A. Pimenov, A.A. Mukhin, V.Y. Ivanov, V.D. Travkin, A.M. Balbashov, and A. Loidl, Nat Phys **2**, 97 (2006).
[83] V.G. Bar'yakhtar and I.E. Chupis, Sov. Phys. Solid State **10**, 2818 (1969).
[84] V.G. Bar'yakhtar and I.E. Chupis, Sov. Phys. Solid State **11**, 26288 (1970).
[85] G.A. Smolenskiĭ and I.E. Chupis, Sov. Phys. Uspekhi **25**, 475 (1982).
[86] R. Valdés Aguilar, A.B. Sushkov, C.L. Zhang, Y.J. Choi, S.-W. Cheong, and H.D. Drew, Phys. Rev. B **76**, 60404 (2007).
[87] H. Katsura, A. V. Balatsky, and N. Nagaosa, Phys. Rev. Lett. **98**, 27203 (2007).
[88] M.P. V. Stenberg and R. de Sousa, Phys. Rev. B **85**, 104412 (2012).
[89] K.M. Rabe, C.H. Ahn, and J.M. Triscone, *Physics of Ferroelectrics: A Modern Perspective* (Springer, Berlin, Heidelberg, New York, 2007).
[90] D. Damjanovic, Reports Prog. Phys. **61**, 1267 (1998).
[91] S.M. Yang, J.G. Yoon, and T.W. Noh, Curr. Appl. Phys. **11**, 1111 (2011).
[92] A. Gruverman and S. V Kalinin, J. Mater. Sci. **41**, 107 (2006).
[93] J. Valasek, Phys. Rev. **15**, 537 (1920).
[94] P. Weiss, Comptes Rendus **143**, 1136 (1906).
[95] W. Cochran, Phys. Rev. Lett. **3**, 412 (1959).
[96] S. Jesse, H.N. Lee, and S. V Kalinin, Rev. Sci. Instrum. **77**, 73702 (2006).
[97] C.J. Howard and H.T. Stokes, Acta Crystallogr. Sect. A **61**, 93 (2005).
[98] S.V. Kalinin, A.N. Morozovska, L.Q. Chen, and B.J. Rodriguez, Repoprts Prog. Phys. **73**, 67 (2010).
[99] S. Kamba, D. Nuzhnyy, M. Savinov, P. Tolédano, V. Laguta, P. Brázda, L. Palatinus, F. Kadlec, F. Borodavka, C. Kadlec, P. Bednyakov, V. Bovtun, M. Kempa, D. Kriegner, J. Drahokoupil, J. Kroupa, J. Prokleška, K. Chapagain, B. Dabrowski, and V. Goian, Phys. Rev. B **95**, 174103 (2017).
[100] F. Gervais, in *Chap. 7 High-Temperature Infrared Reflectivity Spectrosc. by Scanning Interf. Vol. 8 Infrared Millim. Waves*, edited by K.J. Button (Academic, New York, 1983), p. 279.
[101] M.A. Stroscio and M. Dutta, *Phonons in Nanostructures* (Cambridge University Press, 2001).
[102] C. Kittel, in *Instroduction to Solid State Phys.*, edited by S. Johnson, 8th ed. (John Wiley & Sons, Inc., 2005), pp. 321–357.
[103] O. (Olaf) Stenzel, in *Phys. Thin Film Opt. Spectra an Introd.*, edited by G. Ertl, H. Luth, and D.. Mills (Springer Berlin Heidelberg, 2016), pp. 9–15.
[104] R.H. Lyddane, R.G. Sachs, and E. Teller, Phys. Rev. **59**, 673 (1941).
[105] R. Loudon, J. Phys. A Gen. Phys. **3**, 515 (1970).
[106] E.A. Turov and V.G. Shavrov, Sov. Phys. Uspekhi **26**, 593 (1983).
[107] R. Ruppin and R., Phys. Lett. A **299**, 309 (2002).
[108] http://www.ska-polska.pl/en/lab/thz-see-invisible, (2013).
[109] I. Newton, Philos. Trans. R. Soc. **80**, 3075 (1672).
[110] W. Herschel, Philos. Trans. R. Soc. London **90**, 255 (1800).
[111] H. Rubens and B.W. Snow, Philos. Mag. Ser. 5 **35**, 35 (1893).
[112] H. Rubens and E.F. Nichols, Phys. Rev. (Series I) **4**, 314 (1897).
[113] E.F. Nichols, Phys. Rev. (Series I) **4**, 297 (1897).
[114] H. Rubens and K. Kurlbaum, Sitzungsberichte Der K. Preuss. Akad. Der Wissenschaften Zu Berlin **II**, 929 (1900).
[115] E. Brundermann, H.-W. Hubers, and M.F. Kimmitt, in *Terahertz Tech.*, edited by W.T. Rhodes (Springer-Verlag Berlin Heidelberg, 2012), p. 6.
[116] H. Rubens and R.W. Wood, Philos. Mag. Ser. 6 **21**, 249 (1911).
[117] E. Hagen and H. Rubens, Philos. Mag. Ser. 6 **7**, 157 (1904).
[118] F.A. Firestone, Rev. Sci. Instrum. **3**, 163 (1932).
[119] N. Wright and L.W. Herscher, J. Opt. Soc. Am. **37**, 211 (1947).
[120] M.R. Derrick, D. Stulik, and J.M. Landry, in *Sci. Tools Conserv. Infrared Spectrosc. Conserv. Sci.*, edited by B. Tevvy (1999), pp. 1–2.
[121] A.A. Michelson, Philos. Mag. **5**, 256 (1891).
[122] Lord Rayleigh, Philos. Mag. **5**, 407 (1891).
[123] P. Connes, Infrared Phys. **24**, 69 (1984).

[124] P. Jacquinot, Infrared Phys. **24**, 99 (1984).
[125] J.W. Cooley and J.W. Tukey, Math. Comput. **19**, 297 (1965).
[126] J.L. Servoin, F. Gervais, A.M. Quittet, and Y. Luspin, Phys. Rev. B **21**, 2038 (1980).
[127] A. Smekal, Naturwissenschaften **11**, 873 (1923).
[128] A. Compton, Phys. Rev. **21**, 483 (1923).
[129] C.V. Raman and K.S. Krishnan, Nature **121**, 711 (1928).
[130] G. Landsberg and L. Mandelstam, Naturwissenschaften **16**, 557 (1928).
[131] T.H. Maiman, Nature **187**, 493 (1960).
[132] W.S. Boyle and G.E. Smith, Bell Syst. Tech. J. **49**, 587 (1970).
[133] P. Brüesch, in *Phonons Theory Exp. II*, edited by M. Cardona, P. Fulde, K. von Klitzing, and H.-J. Queisser (Springer-Verlag Berlin Heidelberg, 1986), pp. 65–105.
[134] W. Hayes and R. Loudon, in *Scatt. Light by Cryst.* (Dover Publications, Inc, Mineola, New York, 1978), pp. 2–43.
[135] M. Tyunina, A. Dejneka, D. Rytz, I. Gregora, F. Borodavka, M. Vondracek, and J. Honolka, J. Phys. Condens. Matter **26**, 125901 (2014).
[136] M. Planck, Verhandlungen Der Dtsch. Phys. Gesellschaf **2(13)**, 202 (n.d.).
[137] M. Planck, Phys. Ges **2**, (1967).
[138] C.E. Cleeton and N.H. Williams, Phys. Rev. **45**, 234 (1934).
[139] A.M. Nicolson, IEEE Trans. Instrum. Meas. **17**, 395 (1968).
[140] K.H. Yang, P.L. Richards, and Y.R. Shen, Appl. Phys. Lett. **19**, 320 (1971).
[141] M.C. Nuss and J. Orenstein, in *Millim. Submillim. Wave Spectrosc. Solids*, edited by G. Gruner (Springer-Verlag Berlin Heidelberg, 1998), pp. 7–23.
[142] S. Skiadopoulou, V. Goian, C. Kadlec, F. Kadlec, X.F. Bai, I.C. Infante, B. Dkhil, C. Adamo, D.G. Schlom, and S. Kamba, Phys. Rev. B **91**, 174108 (2015).
[143] M. Retuerto, S. Skiadopoulou, M.-R. Li, A.M. Abakumov, M. Croft, A. Ignatov, T. Sarkar, B.M. Abbett, J. Pokorný, M. Savinov, D. Nuzhnyy, J. Prokleška, M. Abeykoon, P.W. Stephens, J.P. Hodges, P. Vaněk, C.J. Fennie, K.M. Rabe, S. Kamba, and M. Greenblatt, Inorg. Chem. **55**, 4320 (2016).
[144] S. Skiadopoulou, F. Borodavka, C. Kadlec, F. Kadlec, M. Retuerto, Z. Deng, M. Greenblatt, and S. Kamba, Phys. Rev. B **95**, 184435 (2017).
[145] R.S. Fishman, Phys. Rev. B **87**, 224419 (2013).
[146] N.A. Spaldin, S.W. Cheong, and R. Ramesh, Phys. Today **63**, 38 (2010).
[147] G. Catalan and J.F. Scott, Adv. Mater. **21**, 2463 (2009).
[148] R. Haumont, J. Kreisel, P. Bouvier, and F. Hippert, Phys. Rev. B **73**, 132101 (2006).
[149] H. Fukumura, S. Matsui, H. Harima, T. Takahashi, T. Itoh, K. Kisoda, M. Tamada, Y. Noguchi, and M. Miyayama, J. Phys. Condens. Matter **19**, 365224 (2007).
[150] R. Palai, H. Schmid, J.F. Scott, and R.S. Katiyar, Phys. Rev. B **81**, 64110 (2010).
[151] D. Kothari, V. Raghavendra Reddy, V.G. Sathe, A. Gupta, A. Banerjee, and A.M. Awasthi, J. Magn. Magn. Mater. **320**, 548 (2008).
[152] D. Rout, K.-S. Moon, and S.-J.L. Kang, J. Raman Spectrosc. **40**, 618 (2009).
[153] J. Hlinka, J. Pokorný, S. Karimi, and I.M. Reaney, Phys. Rev. B **83**, 20101 (2011).
[154] M.K. Singh, H.M. Jang, S. Ryu, and M.-H. Jo, Appl. Phys. Lett. **88**, 42903 (2006).
[155] R. Palai, J.F. Scott, and R.S. Katiyar, Phys. Rev. B **81**, 24115 (2010).
[156] S. Kamba, D. Nuzhnyy, M. Savinov, J. Šebek, J. Petzelt, J. Prokleška, R. Haumont, and J. Kreisel, Phys. Rev. B **75**, 24403 (2007).
[157] G.A. Komandin, V.I. Torgashev, A.A. Volkov, O.E. Porodinkov, I.E. Spektor, and A.A. Bush, Phys. Sol. State **52**, 734 (2010).
[158] N.E. Massa, L. del Campo, D. de Souza Meneses, P. Echegut, G.F.L. Fabbris, G. de M. Azevedo, M.J. Martínez-Lope, and J.A. Alonso, J. Appl. Phys. **108**, (2010).
[159] R.P.S.M. Lobo, R.L. Moreira, D. Lebeugle, and D. Colson, Phys. Rev. B **76**, 172105 (2007).
[160] J. Lu, M. Schmidt, P. Lunkenheimer, A. Pimenov, A.A. Mukhin, V.D. Travkin, and A. Loidl, J. Phys. Conf. Ser. **200**, 12106 (2010).
[161] K. Singh, V. Caignaert, L.C. Chapon, V. Pralong, B. Raveau, and A. Maignan, Phys. Rev. B **86**, 24410 (2012).
[162] M. Cazayous, Y. Gallais, A. Sacuto, R. de Sousa, D. Lebeugle, and D. Colson, Phys. Rev. Lett.

101, 37601 (2008).
163 P. Rovillain, de Sousa, Y. Gallais, A. Sacuto, M. A. M�asson, D. Colson, A. Forget, M. Bibes, A. Barthélémy, and M. Cazayous, Nat. Mater. **9**, 975 (2010).
164 P. Rovillain, M. Cazayous, Y. Gallais, A. Sacuto, R.P.S.M. Lobo, D. Lebeugle, and D. Colson, Phys. Rev. B **79**, 180411 (2009).
165 A. Kumar, J.F. Scott, and R.S. Katiyar, Appl. Phys. Lett. **99**, 62504 (2011).
166 A. Kumar, J.F. Scott, and R.S. Katiyar, Phys. Rev. B **85**, 224410 (2012).
167 D. Sando, A. Agbelele, D. Rahmedov, J. Liu, P. Rovillain, C. Toulouse, I.C. Infante, A.P. Pyatakov, S. Fusil, E. Jacquet, C. Carrétéro, C. Deranlot, S. Lisenkov, D. Wang, J.-M. Le Breton, M. Cazayous, A. Sacuto, J. Juraszek, A.K. Zvezdin, L. Bellaiche, B. Dkhil, A. Barthélémy, and M. Bibes, Nat. Mater. **12**, 641 (2013).
168 D. Talbayev, S.A. Trugman, S. Lee, H.T. Yi, S.-W. Cheong, and A.J. Taylor, Phys. Rev. B **83**, 94403 (2011).
169 J. Jeong, E.A. Goremychkin, T. Guidi, K. Nakajima, G.S. Jeon, S.-A. Kim, S. Furukawa, Y.B. Kim, S. Lee, V. Kiryukhin, S.-W. Cheong, and J.-G. Park, Phys. Rev. Lett. **108**, 77202 (2012).
170 O. Delaire, M.B. Stone, J. Ma, A. Huq, D. Gout, C. Brown, K.F. Wang, and Z.F. Ren, Phys. Rev. B **85**, 64405 (2012).
171 Z. Xu, J. Wen, T. Berlijn, P.M. Gehring, C. Stock, M.B. Stone, W. Ku, G. Gu, S.M. Shapiro, R.J. Birgeneau, and G. Xu, Phys. Rev. B **86**, 174419 (2012).
172 J. Jeong, M.D. Le, P. Bourges, S. Petit, S. Furukawa, S.-A. Kim, S. Lee, S.W. Cheong, and J.-G. Park, Phys. Rev. Lett. **113**, 107202 (2014).
173 U. Nagel, R.S. Fishman, T. Katuwal, H. Engelkamp, D. Talbayev, H.T. Yi, S.-W. Cheong, and T. Rõõm, Phys. Rev. Lett. **110**, 257201 (2013).
174 R. de Sousa and J.E. Moore, Phys. Rev. B **77**, 12406 (2008).
175 R.S. Fishman, N. Furukawa, J.T. Haraldsen, M. Matsuda, and S. Miyahara, Phys. Rev. B **86**, 220402 (2012).
176 R.S. Fishman, J.T. Haraldsen, N. Furukawa, and S. Miyahara, Phys. Rev. B **87**, 134416 (2013).
177 I. Kézsmárki, U. Nagel, S. Bordács, R.S. Fishman, J.H. Lee, H.T. Yi, S.-W. Cheong, and T. Rõõm, Phys. Rev. Lett. **115**, 127203 (2015).
178 J.-G. Park, M.D. Le, J. Jeong, and S. Lee, J. Phys. Condens. Matter **26**, 433202 (2014).
179 C.T. Nelson, P. Gao, J.R. Jokisaari, C. Heikes, C. Adamo, A. Melville, S.-H. Baek, C.M. Folkman, B. Winchester, Y. Gu, Y. Liu, K. Zhang, E. Wang, J. Li, L.-Q. Chen, C.-B. Eom, D.G. Schlom, and X. Pan, Science (80-.). **334**, 968 (2011).
180 P. Hermet, M. Goffinet, J. Kreisel, and P. Ghosez, Phys. Rev. B **75**, 220102 (2007).
181 R.H. Lyddane, R.G. Sachs, and E. Teller, Phys. Rev. **59**, 673 (1941).
182 V. Goian, S. Kamba, N. Orloff, T. Birol, C.H. Lee, D. Nuzhnyy, J.C. Booth, M. Bernhagen, R. Uecker, and D.G. Schlom, Phys. Rev. B **90**, 174105 (2014).
183 S. Kamba, V. Goian, D. Nuzhnyy, V. Bovtun, M. Kempa, J. Prokleška, M. Bernhagen, R. Uecker, and D.G. Schlom, Phase Transitions **86**, 206 (2013).
184 C.M. Folkman, H.W. Jang, C.B. Eom, C.T. Nelson, X.Q. Pan, Y.L. Li, L.Q. Chen, A. Kumar, V. Gopalan, and S.K. Streiffer, Appl. Phys. Lett. **94**, 251911 (2009).
185 M.P. V Stenberg and R. de Sousa, Phys. Rev. B **80**, 94419 (2009).
186 D. Nuzhnyy, J. Petzelt, S. Kamba, P. Kužel, C. Kadlec, V. Bovtun, M. Kempa, J. Schubert, C.M. Brooks, and D.G. Schlom, Appl. Phys. Lett. **95**, 232902 (2009).
187 A.K. Tagantsev, V.O. Sherman, K.F. Astafiev, J. Venkatesh, and N. Setter, J. Electroceramics **11**, 5 (2003).
188 Y. Takahashi, R. Shimano, H. Murakawa, and Y. Tokura, Nat. Phys. **8**, 121 (2012).
189 Y. Tokura, T. Kimura, H. Sawada, K. Terakura, and K.. Kobayashi, Nature **395**, 677 (1998).
190 N. Setter and L.E. Cross, J. Mater. Sci. **15**, 2478 (1980).
191 V.A. Isupov and N.N. Krainik, Phys. Sol. State **6**, 2975 (1965).
192 T.H. O'Dell, *The Electrodynamics of Magneto-Electric Media* (North-Holland: Amsterdam, 1970).
193 V.E. Wood and A.E. Austin, Int. J. Magn. **5**, 303 (1974).
194 Y. Tokura, S. Seki, and N. Nagaosa, Reports Prog. Phys. **77**, 76501 (2014).
195 J. Wang, J.B. Neaton, H. Zheng, V. Nagarajan, S.B. Ogale, B. Liu, D. Viehland, V.

Vaithyanathan, D.G. Schlom, U. V Waghmare, N.A. Spaldin, K.M. Rabe, M. Wuttig, and R. Ramesh, Science (80-.). **299**, 1719 (2003).
196 M. Azuma, K. Takata, T. Saito, S. Ishiwata, Y. Shimakawa, and M. Takano, J. Am. Chem. Soc. **127**, 8889 (2005).
197 R. Seshadri and N.A. Hill, Chem. Mater. **13**, 2892 (2001).
198 T. Kimura, T. Goto, H. Shintani, K. Ishizaka, T. Arima, and Y. Tokura, Nature **426**, 55 (2003).
199 P. Barone and S. Picozzi, C. R. Phys. **16**, 143 (2015).
200 K. Singh, C. Simon, E. Cannuccia, M.-B. Lepetit, B. Corraze, E. Janod, and L. Cario, Phys. Rev. Lett. **113**, 137602 (2014).
201 A. Walsh, D.J. Payne, R.G. Egdell, and G.W. Watson, Chem. Soc. Rev. **40**, 4455 (2011).
202 S.A. Larrégola, J.A. Alonso, J.C. Pedregosa, M.J. Martínez-Lope, M. Algueró, V. De la Peña-O'Shea, F. Porcher, F. Illas, and R.E. Carbonio, Dalt. Trans. **89**, 5453 (2009).
203 J. Blasco, R.I. Merino, J. García, and M.C. Sánchez, J. Phys. Condens. Matter **18**, 2261 (2006).
204 I.-K. Jeong, J.S. Ahn, B.G. Kim, S. Yoon, S.P. Singh, and D. Pandey, Phys. Rev. B **83**, 64108 (2011).
205 R. Martinez, R. Palai, H. Huhtinen, J. Liu, J.F. Scott, and R.S. Katiyar, Phys. Rev. B **82**, 134104 (2010).
206 R. Blinc, M. Kosec, J. Holc, Z. Trontelj, Z. Jaglicic, and N. Dalal, Ferroelectrics **349**, 16 (2007).
207 D.M. Evans, A. Schilling, A. Kumar, D. Sanchez, N. Ortega, M. Arredondo, R.S. Katiyar, J.M. Gregg, and J.F. Scott, Nat. Commun. **4**, 1534 (2013).
208 A. Huq, J.P. Hodges, O. Gourdon, and L.Z. Heroux, Krist. Proc. **1**, 127 (2011).
209 H.M. Rietveld and IUCr, J. Appl. Crystallogr. **2**, 65 (1969).
210 J. Rodríguez-Carvajal and Juan, Phys. B Condens. Matter **192**, 55 (1993).
211 A. Coelho, TOPAS-Academic http://www.topas (2007).
212 S.A. Ivanov, P. Nordblad, R. Mathieu, R. Tellgren, C. Ritter, M.A. Malitskaya, I.N. Zakharchenko, S.A. Prosandeev, D. Vakmin, A.J. Jacobson, N.A. Spaldin, K.M. Rabe, M. Wuttig, and R. Ramesh, Dalt. Trans. **39**, 11136 (2010).
213 G. Baldinozzi, G. Calvarin, P. Sciau, D. Grebille, and E. Suard, Acta Crystallogr. Sect. B **56**, 570 (2000).
214 R. Morrow, R. Mishra, O.D. Restrepo, M.R. Ball, W. Windl, S. Wurmehl, U. Stockert, B. Büchner, and P.M. Woodward, J. Am. Chem. Soc. **135**, 18824 (2013).
215 L. Ortega-San Martin, J.P. Chapman, L. Lezama, J. Sánchez-Marcos, J. Rodríguez-Fernández, M.I. Arriortua, T. Rojo, S.K. Sinha, D. Vaknin, and A.J. Jacobson, J. Mater. Chem. **15**, 183 (2005).
216 R.D. Shannon, Acta Crystallogr. Sect. A **32**, 751 (1976).
217 J. Blasco, S. Lafuerza, J. García, G. Subías, M.C. Sánchez, V. Cuartero, and J. Stankiewicz, Dalt. Trans. **40**, 3211 (2011).
218 S.A. Larrégola, J.A. Alonso, V.A. de la Peña-O'Shea, D. Sheptyakov, V. Pomjakushin, M.T. Fernandez-Díaz, and J.C. Pedregosa, Inorg. Chem. **53**, 5609 (2014).
219 S.A. Larreégola, J.A. Alonso, D. Sheptyakov, M. Algueró, A. Muñoz, V. Pomjakushin, and J.C. Pedregosa, J. Am. Chem. Soc. **132**, 14470 (2010).
220 N.E. Brese and M. O 'keeffe, Acta Cryst **47**, 192 (1991).
221 I.D. Brown, A. Dabkowski, and A. McCleary, Acta Crystallogr. Sect. B Struct. Sci. **53**, 750 (1997).
222 B.J. Campbell, H.T. Stokes, D.E. Tanner, and D.M.J. Hatch, J. Appl. Crystallogr. **39**, 607 (2006).
223 M. Retuerto, M. García-Hernández, M.J. Martínez-Lope, M.T. Fernández-Díaz, J.P. Attfield, J.A. Alonso, R.E. Carbonio, J. Simon, T. Walther, W. Mader, D. Topwal, and D.D. Sarma, J. Mater. Chem. **17**, 3555 (2007).
224 A.K. Azad, S.-G. Eriksson, A. Mellergard, S.A. Ivanov, J. Eriksen, and H. Rundlof, Mater. Res. Bull. **37**, 1797 (2002).
225 P. Lunkenheimer, S. Krohns, S. Riegg, S.G. Ebbinghaus, A. Reller, and A. Loidl, Eur. Phys. J. Spec. Top. **180**, 61 (2009).
226 T. Ostapchuk, J. Petzelt, V. Zelezny, S. Kamba, V. Bovtun, V. Porokhonskyy, A. Pashkin, P. Kuzel, M. Glinchuk, I. Bykov, B. Gorshunov, and M. Dressel, J. Phys. Condens. Matter **13**, 2677 (2001).

227 V. Dvořák, Ferroelectrics **7**, 1 (1974).
228 J. Hlinka, T. Ostapchuk, D. Noujni, S. Kamba, and J. Petzelt, Phys. Rev. Lett. **96**, 27601 (2006).
229 A.S. Barker and A. Sievers, J. Rev. Mod. Phys. **47**, S1 (1975).
230 P.A. Fleury, J.F. Scott, and J.M. Worlock, Phys. Rev. Lett. **21**, 16 (1968).
231 J. Hlinka, T. Ostapchuk, E. Buixaderas, C. Kadlec, P. Kuzel, I. Gregora, J. Kroupa, M. Savinov, A. Klic, J. Drahokoupil, I. Etxebarria, and J. Dec, Phys. Rev. Lett. **112**, 197601 (2014).
232 A.K. Tagantsev, K. Vaideeswaran, S.B. Vakhrushev, A. V Filimonov, R.G. Burkovsky, A. Shaganov, D. Andronikova, A.I. Rudskoy, A.Q.R. Baron, H. Uchiyama, D. Chernyshov, A. Bosak, Z. Ujma, K. Roleder, A. Majchrowski, J.-H. Ko, and N. Setter, Nat. Commun. **4**, 2229 (2013).
233 K. Rabe, in *Funct. Met. Oxides New Sci. Appl.*, edited by S. Ogale and V. Venkateshan (Wiley-VCH Verlag GmbH & Co. KGaA, 2013).
234 R. Becker and H. Berger, Acta Crystallogr. Sect. E **62**, 222 (2006).
235 T. Aoyama, K. Yamauchi, A. Iyama, S. Picozzi, K. Shimizu, and T. Kimura, Nat. Commun **5**, 4927 (2014).
236 S.H. Chun, Y.S. Chai, Y.S. Oh, D. Jaiswal-Nagar, S.Y. Haam, I. Kim, B. Lee, D.H. Nam, K.-T. Ko, J.-H. Park, J.-H. Chung, and K.H. Kim, Phys. Rev. Lett. **104**, 37204 (2010).
237 N. Lee, C. Vecchini, Y.J. Choi, L.C. Chapon, A. Bombardi, P.G. Radaelli, and S.-W. Cheong, Phys. Rev. Lett. **110**, 137203 (2013).
238 Y.S. Chai, S. Kwon, S.H. Chun, I. Kim, B.-G. Jeon, K.H. Kim, and S. Lee, Nat. Commun **5**, (2014).
239 J.W. Kim, S. Artyukhin, E.D. Mun, M. Jaime, N. Harrison, A. Hansen, J.J. Yang, Y.S. Oh, D. Vanderbilt, V.S. Zapf, and S.-W. Cheong, Phys. Rev. Lett. **115**, 137201 (2015).
240 R.E. Newnham and E.P. Meagher, Mater. Res. Bull. **2**, 549 (1967).
241 I. Živković, K. Prša, O. Zaharko, and H. Berger, J. Phys. Condens. Matter **22**, 56002 (2010).
242 S.A. Ivanov, R. Mathieu, P. Nordblad, R. Tellgren, C. Ritter, E. Politova, G. Kaleva, A. Mosunov, S. Stefanovich, and M. Weil, Chem. Mater. **25**, 935 (2013).
243 M.O. Yokosuk, S. Artyukhin, A. Al-Wahish, X. Wang, J. Yang, Z. Li, S.-W. Cheong, D. Vanderbilt, and J.L. Musfeldt, Phys. Rev. B **92**, 144305 (2015).
244 X. Wang, F.-T. Huang, J. Yang, Y.S. Oh, and S.-W. Cheong, APL Mater. **3**, 76105 (2015).
245 D. Szaller, S. Bordács, V. Kocsis, T. Rõõm, U. Nagel, and I. Kézsmárki, Phys. Rev. B **89**, 184419 (2014).
246 P. Rovillain, R. de Sousa, Y. Gallais, A. Sacuto, M.A. Méasson, D. Colson, A. Forget, M. Bibes, A. Barthélémy, and M. Cazayous, Nat Mater **9**, 975 (2010).
247 G. Blasse and W. Hordijk, J. Solid State Chem. **5**, 395 (1972).
248 T.C. Damen, S.P.S. Porto, and B. Tell, Phys. Rev. **142**, 570 (1966).
249 G. Turrell, J. Raman Spectrosc. **15**, 103 (1984).
250 C. Bremard, P. Dhamelincourt, J. Laureyns, and G. Turrell, Appl. Spectrosc. **39**, 1036 (1985).
251 H. Morishita, Y. Hoshino, S. Higuchi, F. Kaneko, K. Tashiro, and the late M. Kobayashi, J. Raman Spectrosc. **31**, 455 (2000).
252 D. Niermann, C.P. Grams, P. Becker, L. Bohatý, H. Schenck, and J. Hemberger, Phys. Rev. Lett. **114**, 37204 (2015).
253 L.I. Kosse, E.D. Politova, V.V. Chechkin, E.A. Myzgin, and Y.N. Medvedev, B.S., Venevtsevae, Izv Akad Nauk SSSR, Neorg Mater **18(11)**, 1879 (1982).
254 L.I. Kosse, E.D. Politova, and Y.N. Venevtsev, Zhurnal Neorg. Khim. **28**, 1689 (1983).
255 M. Herak, H. Berger, M. Prester, M. Miljak, I. Zivkovic, O. Milat, D. Drobac, S. Popovic, and O. Zaharko, J. Phys. Condens. Matter **17**, 7667 (2005).
256 K.Y. Choi, P. Lemmens, E.S. Choi, and H. Berger, J. Phys. Condens. Matter **20**, 505214 (2008).
257 M. Hudl, R. Mathieu, S.A. Ivanov, M. Weil, V. Carolus, T. Lottermoser, M. Fiebig, Y. Tokunaga, Y. Taguchi, Y. Tokura, and P. Nordblad, Phys. Rev. B **84**, 180404 (2011).
258 S.A. Ivanov, P. Nordblad, R. Mathieu, R. Tellgren, C. Ritter, N. V Golubko, E.D. Politova, and M. Weil, Mater. Res. Bull. **46**, 1870 (2011).
259 S.A. Ivanov, R. Tellgren, C. Ritter, P. Nordblad, R. Mathieu, G. Andre, N.V. Golubko, E.D. Politova, and M. Weil, Mater. Res. Bull. **47**, 63 (2012).
260 R. Mathieu, S.A. Ivanov, P. Nordblad, and M. Weil, Eur. Phys. J. B **86**, 1 (2013).

[261] M.-R. Li, M. Croft, P.W. Stephens, M. Ye, D. Vanderbilt, M. Retuerto, Z. Deng, C.P. Grams, J. Hemberger, J. Hadermann, W.-M. Li, C.-Q. Jin, F.O. Saouma, J.I. Jang, H. Akamatsu, V. Gopalan, D. Walker, and M. Greenblatt, Adv. Mater. **27**, 2177 (2015).
[262] W.-H. Li, C.-W. Wang, D. Hsu, C.-H. Lee, C.-M. Wu, C.-C. Chou, H.-D. Yang, Y. Zhao, S. Chang, J.W. Lynn, and H. Berger, Phys. Rev. B **85**, 94431 (2012).
[263] P. Tolédano, V. Carolus, M. Hudl, T. Lottermoser, D.D. Khalyavin, S.A. Ivanov, and M. Fiebig, Phys. Rev. B **85**, 214439 (2012).
[264] A.B. Harris, Phys. Rev. B **85**, 100403 (2012).
[265] H. Singh, H. Ghosh, T. V. Chandrasekhar Rao, G. Sharma, J. Saha, and S. Patnaik, J. Appl. Phys. **119**, 44104 (2016).
[266] H. Singh, H. Ghosh, T. V. Chandrasekhar Rao, A.K. Sinha, and P. Rajput, J. Appl. Phys. **116**, 214106 (2014).
[267] R. Becker, M. Johnsson, and H. Berger, Acta Crystallogr. Sect. C Cryst. Struct. Commun. **62**, i67 (2006).
[268] M.E. Foglio and G.E. Barberis, Brazilian J. Phys. **36**, 40 (2006).
[269] L. Chaix, S. de Brion, S. Petit, R. Ballou, L.-P. Regnault, J. Ollivier, J.-B. Brubach, P. Roy, J. Debray, P. Lejay, A. Cano, E. Ressouche, and V. Simonet, Phys. Rev. Lett. **112**, 137201 (2014).
[270] B. Lorenz, Y.Q. Wang, Y.Y. Sun, and C.W. Chu, Phys. Rev. B **70**, 212412 (2004).

List of Publications

Publications related to the current thesis:

- *Spin and lattice excitations of $BiFeO_3$ thin film and ceramics,* S. Skiadopoulou, V. Goian, C. Kadlec, F. Kadlec, X. F. Bai, I. C. Infante, B. Dkhil, C. Adamo, D. G. Schlom, and S. Kamba, *Phys. Rev. B,* **91**, 174108 (2015)

- *Pb_2MnTeO_6 Double Perovskite: An Antipolar Anti-ferromagnet*, Maria Retuerto, Stella Skiadopoulou, Man-Rong Li, Artem M. Abakumov, Mark. Croft, Alexander Ignatov, Tapati Sarkar, Brian M. Abbett, Jan Pokorný, Maxim Savinov, Dmitry Nuzhnyy, Jan Prokleška, Milinda Abeykoon, Peter W Stephens, Jason P. Hodges, Přemysl Vaněk, Craig J. Fennie, Karin M. Rabe, Stanislav Kamba, and Martha Greenblatt, *Inorg. Chem*., **55** (9), 4320–4329 (2016)

- *Magnetoelectric excitations in multiferroic Ni_3TeO_6,* S. Skiadopoulou, Fedir Borodavka, Christelle Kadlec, Filip Kadlec, Maria Retuerto, Zheng Deng, Martha Greenblatt, and Stanislav Kamba, *Phys. Rev. B,* **95**, 184435 (2017)

Other publications:

- *Comment on "Interesting Evidence for Template-Induced Ferroelectric Behavior in Ultra-Thin Titanium Dioxide Films Grown on (110) Neodymium Gallium Oxide Substrates"*, S. Skiadopoulou, S. Kamba, J. Drahokoupil, J. Kroupa, N. Deepak, M. E. Pemble and R. W. Whatmore, *Adv. Funct. Mater*., **26**, 642-646 (2016)

- *Optical and vibrational properties of $(ZnO)_k$ In_2O_3 natural superlattice nanostructures*, Samuel Margueron, Jan Pokorny, Stella Skiadopoulou, Stanislav Kamba, Xin Liang and David R. Clark, *J. Appl. Phy*s., **119**, 195103 (2016)

- *Chapter 6: Thin-Film Porous Ferroic Nanostructures: Strategies and Characterization*, Alichandra Castro, Paula Ferreira, Stella Skiadopoulou, Liliana P. Ferreira, Margarida Godinho, Brian J. Rodriguez and Paula M. Vilarinho, In: Miguel Algueró, J. Marty Gregg, Liliana Mitoseriu, in *Nanoscale Ferroelectrics and Multiferroics: Key Processing and Characterization Issues, and Nanoscale Effects, Volume I and II*, Wiley, 147-162 (2016)

List of variables

$n*$	complex refraction index
n	real refraction index
k	imaginary refraction index
ε^*	complex dielectric function
ε'	permittivity (real part of ε^*)
ε''	losses (imaginary part of ε^*)
$\varepsilon(0)$	static permittivity (dielectric constant)
ε_∞	electronic contribution to permittivity
μ^*	complex magnetic permeability
R	Reflectivity
T	Transmission
$\boldsymbol{q}$	wavevector of phonon modes
ω	frequency of phonon modes
ω_{TO}	transverse frequency of phonon modes
ω_{LO}	longitudinal frequency of phonon modes
γ	damping of phonon modes
γ_{TO}	transverse damping of phonon modes
γ_{LO}	longitudinal damping of phonon modes
$\Delta\varepsilon$	dielectric strength of phonon modes
f	oscillator strength ($\Delta\varepsilon \cdot \omega^2$) of phonon modes
χ^e	dielectric susceptibility
χ^m	magnetic susceptibility
$\boldsymbol{J}_\mathrm{m}$	magnetization current
$\boldsymbol{J}_\mathrm{e}$	polarization current
M	magnetization
$\boldsymbol{E}$	electric field
$\boldsymbol{E}_{ext}$	external electric field
$\boldsymbol{H}$	magnetic field
$\boldsymbol{H}_{ext}$	external magnetic field
$\boldsymbol{D}$	electric displacement field
$\boldsymbol{E}^\omega$	electric component of the electromagnetic wave

$\boldsymbol{H}^{\omega}$ magnetic component of the electromagnetic wave

$\boldsymbol{k}$ wavevector of electromagnetic wave propagation

c speed of light

$\hbar$ Planck constant

a the lattice constant

F free energy

T_C Curie temperature, ferroelectric phase transition temperature

T_N Néel temperature, antiferromagnetic phase transition temperature

P^S spontaneous polarization

M^S spontaneous magnetization

α_{ij} linear magnetoelectric coefficient

$\boldsymbol{D}_{ij}$ Dzyaloshinskii-Moriya (DM) interaction

$\boldsymbol{S}$ spin

J exchange interaction coefficient

Φ_n cyclon modes

Ψ_n extra-cyclon modes

C_{P} heat capacity

σ' conductivity

List of abbreviations

ME	magnetoelectric
FM	ferromagnetic
AFM	antiferromagnetic
FiM	ferrimagnetic
FE	ferroelectric
AFE	antiferroelectric
DM	Dzyaloshinskii-Moriya
IR	infrared
FIR	far infrared
MIR	mid infrared
NIR	near infrared
FTIR	Fourier-transform infrared
THz	terahertz
TDS	time-domain spectroscopy
RT	room temperature
BZ	Brillouin zone
TO	transverse optical modes
LO	longitudinal optical modes
LST	Lyddane-Sachs-Teller relation
CCD	charged coupled device
SOJT	second order Jahn–Teller
PXD	powder X-ray diffraction
PND	powder neutron diffraction
XANES	X-ray absorption near edge spectroscopy
SPXD	synchrotron powder diffraction
SQUID	superconducting quantum interference device
SHG	second harmonic generation
FC	field cooling
ZFC	zero field cooling
DSC	differential scanning calorimeter
PPMS	physical property measurement system
DFT	density functional theory

SI	supporting information
NSLS	national synchrotron light source